Department of Environment Systems
Graduate School of Frontier Sciences
The University of Tokyo

2021

Master's Thesis

Modeling Electro-Thermal Heating for Analyzing Heavy Oil Production

(オイルサンド層からの重質油生産のための電熱加熱モデルの開発)

Submitted July 21, 2021

Adviser: Professor Tomochika Tokunaga

Co-adviser: Professor Shigeru Tabeta

Ekaterina Ulanova

Abstract

Today, under rapid climate change, people pay more attention to sustainable sources of energy. Yet, development and implementation of renewable energies in global scale is time and money consuming, and hence, people keep continuously using fossil fuels as main energy resources. Therefore, we need to think how to continue producing oil with less harm to environment. Due to conventional oil resources depletion, more attention is paid to heavy oil and bitumen production. It was proven by researches and experiments that thermal methods such steam injection are the most effective oil recovery enhancement methods. Still, it has several disadvantages which include loss of energy and high costs. Electro-thermal heating method (ETHM) is considered to be environmentally friendly as it does not imply gas generation on the surface. It was studied as soil remediation method and as heating method with vapor generation inside the reservoir.

The purpose of this study is to simulate bitumen extraction from Hangingstone oil sands field by using ETHM to calculate current, heat, and fluid flow in the reservoir and surrounding formations to quantitatively analyze ETHM in oil sands in order to estimate the efficiency of this method.

ETHM was divided into simple basic problems to understand the physics of the process, find appropriate initial and boundary conditions, and analyze the obtained results stability and accuracy. Finally, 2-D geological model of Hangingstone oil sands field was built to simulate ETHM. In the model, three layers were set, i.e., a reservoir sand sandwiched by limestone below and mudstone above. The model domain was chosen to be 333m depth and 70m width. The thicknesses of top mudstone layer, the reservoir, and the bottom limestone were 155m, 28m, and 150m, respectively. Water injection wells were set at both lateral boundaries and production well at the central position between the injection wells in the reservoir. The distance between the wells was set to be 35m in the model. Initial conditions were set to be hydrostatic pressure and temperature distribution to be equal to the geothermal gradient. Also, initial bitumen saturation was assumed to be 0.28 in the reservoir sand while fully water saturated conditions were assigned for both the limestone and mudstone layers. Lateral boundary conditions were set as mirror, i.e., no flow conditions with respect to fluid, heat, and electrical currents. Water injection rate and electrical current intensity were specified in the injection wells and the production amount was set at the central production well, and for the electrical current, the production well was specified to be grounded. Temperature dependency of bitumen viscosity was specified based on the data by Y. Souraki, M. Ashrafi. Water viscosity dependence on temperature was also considered in this thesis.

For the first 15 days system was preheated without fluid injection into sand formation. After 15^{th} day water was injected and bitumen production started. Total calculation time was 35 days. Following results were obtained.

Two-phase flow pattern was uneven and resembled temperature increase pattern into the system. As temperature increased at the electrodes and bottom of production well, water flew to that area as bitumen viscosity decreased and became more movable.

Temperature profile was uneven and was highly affected by the geometry and electrode configuration. This pattern was caused by electric field convergence at the edge. Round shape configuration and elongation of production well helped to minimize electric field convergence at the edges. To prevent electrodes from overheating, cooling system of electrodes was successfully implemented. As a result, temperature on electrodes did not exceed 40°C. Cold water injection into sand formation cooled down the rocks and decreased the resistivity of the system. ETHM became less effective as it is based on the principle the more resistivity of the system the more heat accumulates. As bitumen is high viscous, sand reservoir was preheated during first 15 days. As water usually flows along the path of least resistance, it reached to the production well at the point of higher temperature, where bitumen has already become movable.

It was considered that maximum heating temperature of the system should not exceed 100°C, which is boiling point of water. However, previous simulation results (Appendix) showed that under 100°C, bitumen viscosity value was still greater than water viscosity. With pressure increase the boiling point of water also increases. Therefore, maximum allowed temperature increase in the system was set 200°C, which resulted in more complete bitumen displacement profile.

Production rate of bitumen and water showed that during first 20 days production of bitumen is predominant. Estimated recovery factor was 73%, which means that ETHM operated successfully. However, on 35th day there were rapid bitumen recovery decrease and water recovery increase. This pattern is typical for oil production. Suggested geometry configuration can improve recovery factor, as temperature increase would become even and water would slowly expel bitumen from the formation.

Acknowledgements

First of all, I would like to extend my deepest gratitude to my supervisor Prof. Tomochika Tokunaga for all his support and guidance during these two years of Master's research; for his patience, motivation, enthusiasm, and immense knowledge. His guidance helped me throughout my research process, participating in conference, and writing this thesis. I could not have imagined having a better advisor and mentor for my Master's study.

I sincerely thank my co-advisor Prof. Shigeru Tabeta for his valuable time, insightful suggestions, and encouragement which incited me to improve and widen my research from various perspectives.

I am hugely indebted to my lab-members Jiaqi Lui, Shogo Hirota, Mao Ouyang, Sakambari Padhi, Yuka Ito, Satoshi Tajima. Thank you for all the suggestions on numerical simulation improvement and time on going through the chapters of this thesis.

I thank all the other members of the Toku-Lab for camaraderie, discussions and help in all aspects of life during my stay in Japan. It was a great pleasure attending our weekly seminars and I appreciate all the fruitful discussions. Thank you for accepting me into the group.

My sincere thanks goes to my friend Project Researcher of the University of Tokyo Dr. Tobias Binder for discussions on the physical aspects of this thesis.

I would like to express my gratitude to the Ministry of Education, Culture, Sports, Science and Technology (MEXT) of Japan, which made my stay in Japan possible.

I am extremely grateful to my family and friends for all their moral support and encouragement throughout my Master's research. I sincerely thank my caring, loving, and supportive husband, Fiodar, for all your love that gave me the power to be strong and to overcome difficulties. It was a great comfort and relief to know that you were willing to provide management of our household activities while I completed my research work. My heartfelt thanks. Last but not the least, I would like to thank my parents for their unconditional love, support, belief and guidance, spiritual teachings and for everything that inspired me to achieve my goals in my professional and personal life.

Table of Contents

List of Tables

List of Figures

Chapter 1

Introduction

1.1. Background

1.1.1. Social Importance of Heavy Oil Production

It is well known that one of the main problems of 21st century is climate change which includes global warming. Production of fossil fuels makes great contribution to CO_2 and methane gas release into atmosphere. These gases are believed to be the strongest greenhouse gases and represent 90% of the largest drivers of global warming (US EPA, 2020). During the last 100 years (between 1906 and 2005), average atmospheric temperature increased around 1°C and the rate of temperature increase was doubled in the last 50 years (Riebeek and Simmon, 2010). The increase of temperature causes natural disasters which in turn make people invent and develop new renewable sources of energy, such as hydropower, solar, ocean, wind power. The most optimistic sustainable development scenario to 2040 implies the increase of the usage of renewable energy up to 67% (Fig. 1.1) (IEA, 2018). Yet, development and implementation of renewable energies in global scale is time and money consuming, and hence, people may continuously use fossil fuels as main energy resources (Fig. 1.1) (IEA, 2018). Today, taking into account all the reasons mentioned above, we need to think how to continue producing oil with less harm to environment.

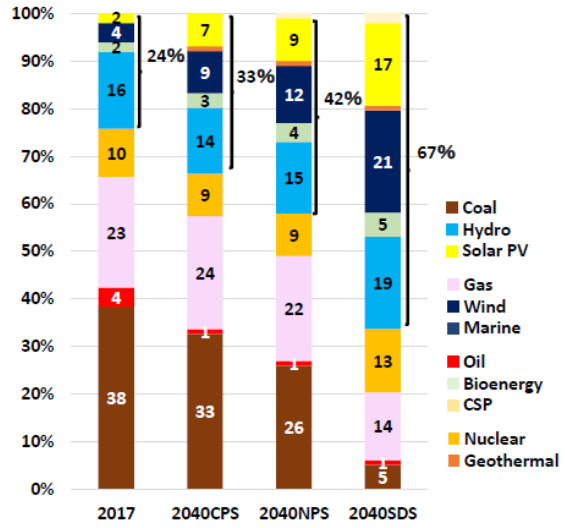

Figure 1.1 Power generation scenarios to 2040 (IEA, 2018) CPS – current policies scenario, NPS – new policies scenario, SDS – sustainable policies scenario.

Oil production started in the middle of 19th century and reached its peak at the end of 20th century (Maugeri and Leonardo, 2006). The increase of oil consumption has caused huge depletion of conventional oil resources (Maugeri and Leonardo, 2006). Nowadays, only 30% of oil resources is conventional type (Golpour, Smith, 2017). The rest is unconventional, in which 15% is heavy oil, 25% is extra heavy oil, and 30% is oil sands bitumen (Fig. 1.2) (Golpour, Smith, 2017). This change of resources distribution made people pay more attention to heavy oil production.

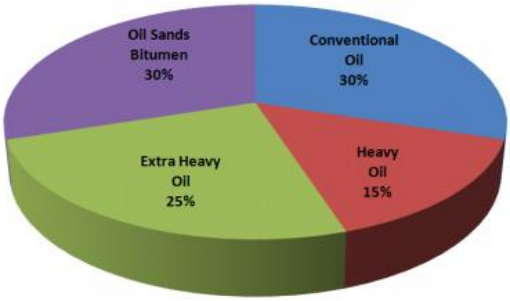

Fig. 1.2. Conventional and unconventional oil resources in 2017 (Golpour and Smith, 2017).

From ecological perspective, heavy oil production and refining is a dirty process. Heavy oil is usually hard to produce, and it necessitates to implement enhanced oil recovery (EOR) methods which require more energy input. Therefore, heavy oil and oil sands production have more severe environmental impacts than conventional oil production. It generates three times more CO_2 emissions compared with conventional oil production (Lee Bell BA MA, 2009). Despite all these negative effects, heavy oil production has never slowed down. Under the rapid climate change with the necessity of fossil fuels, it is crucial to think of alternative EOR methods that would reduce negative impact of oil extraction on the environment.

1.1.2 Characteristics of Heavy Oil

Heavy oil is well-known for its high viscosity. It is hardly movable and cannot be diluted in the water. Heavy oil can be classified into three types: heavy oil – a liquid oil with gravity below 20 API, extra-heavy oil with gravity less than 10 API and viscosity larger than 10000 cP, oil sands - a mixture of oil and sands with gravity less than 10 API and viscosity much greater than 10000 cP (Attanasi and Meyer, 2010). API gravity is an inverse measure of density showing how heavy or light the petroleum liquid is in comparison to the water. Viscosity of heavy oil is highly dependent on temperature (Fig. 1.3) (Raicar, Procter, 1984). For example, with increase in temperature from 20°C to 100°C oil viscosity drops more than 10^3 times. Due to this fact, thermal methods are proved to be efficient for heavy oil production. Heavy oil is rich for its composition, for example, asphaltenes are used to make asphalt surface for roads. It is also used in manufacturing roofing materials, paint, and cables. Heavy oil can be classified into two groups: with sulfur over 1% and less than 1% (Blackman, R.A.A.. 1986). Sulfur is considered to be a contaminant that degrades the quality of oil which makes bitumen refining more complicated.

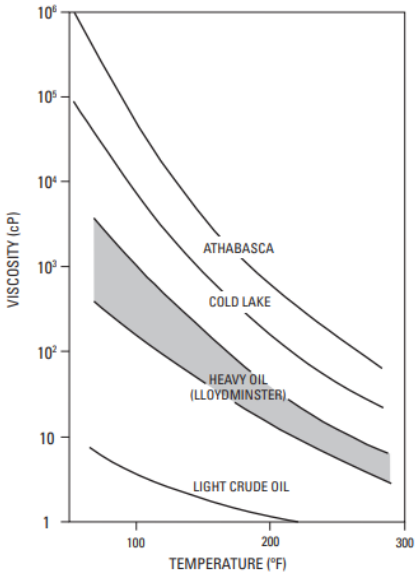

Fig. 1.3. Viscosity of some heavy oil in Alberta oil field as a function of temperature, (Raicar and Proctor, 1984).

Heavy oil and oil sands resources are widespread globally (Fig. 1.4). There are top four countries which in total have 64.4% of global recoverable heavy oil resources. Venezuela, USA, Saudi Arabia and Mexico hold in total 81.72 billion tons of recoverable resources. Extra-heavy oil is mainly produced in Venezuela meanwhile other countries extract heavy oil (Fig. 1.5) (Liu and Wang, 2019).

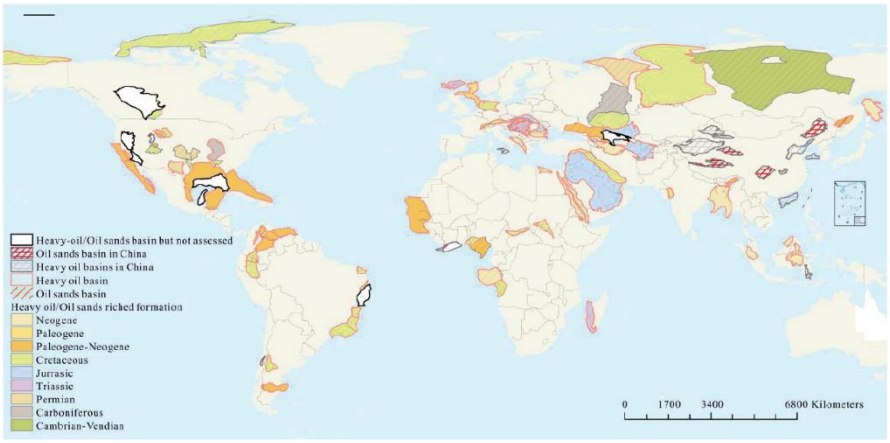

Fig. 1.4. Global distribution of heavy-oil and oil-sand resources (Liu and Wang, 2019).

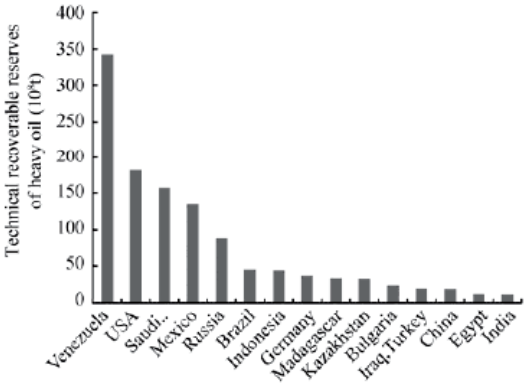

Fig. 1.5. Histograms of top 15 heavy-oil-rich countries (Liu and Wang, 2019).

Oil sands rich countries are Canada and Russia; around 30% of recoverable oil sands resources of the world are located in Canada, Athabaska. Even though Russia does not produce oil sands in commercial scale, it has relatively big resources i.e., 24% of total global amount (Fig. 1.6) (Liu and Wang, 2019).

Among the countries producing oil sands, Canada is the only country which has successfully developed large-scale commercial oil sands. Starting from 2010 till 2016, oil sands production in Canada increased from 205.4 kt/day to 332.97 kt/day in accordance with Alberta Energy Resources Conservation Board (ERCB) and the Canada Association of Petroleum Producers (CAPP). It is predicted that by 2035, production rate of oil sands in Athabaska would increase to 872.19 kt/day (Hart Energy, 2013).

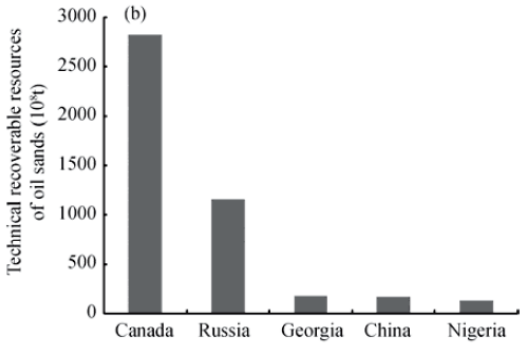

Fig. 1.6. Five oil sands rich countries (Liu and Wang, 2019).

1.1.3. Methodologies for Heavy Oil Production

Each oil field has three stages of oil production process (Temizel and Canbaz, 2018). The first stage implies production under natural reservoir pressure. At the time when reservoir pressure starts decreasing, second stage begins by injecting water into the strata through injecting wells. This process sustains reservoir pressure and keeps production rates. First two stages usually continue until 20-30% of oil is extracted. Then, third stage starts by applying Enhanced Oil Recovery methods (EOR) methods. These methods usually stimulate oil production up to 70%.

The most effective EOR methods for heavy oil production are considered to be thermal methods as it decreases viscosity of bitumen significantly. Thermal methods can be divided into two groups – heat generated on surface and heat generated in the reservoir.

The most common method using heat generated on surface is steam injection. It has many variations, for example, Steam Flooding (SF), Cyclic Steam Stimulation (CSS), and Steam Assisted Gravity Drainage (SAGD). Basic principle of steam injection is to decrease viscosity of oil and increase its mobility. The most popular heating methods used on heavy oil reservoirs are CSS and SAGD.

CSS is also known as Huff and Puff method. It has three stages, i.e., injection, soaking and production (Fig. 1.7). Firstly, during a period from week to month, steam is injected at temperature around 300°C. Then it sits and soaks into the formation for several days. Next, the production starts, and it continues till the production rate is decreased. After that, a new cycle of steam injection starts. This process is repeated few times until cost of injected steam is higher than cost of produced oil.

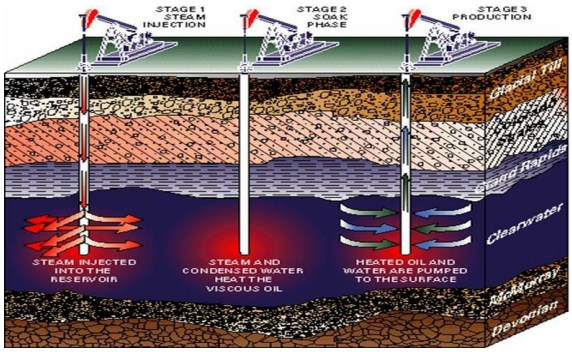

Fig. 1.7. Stages of CSS (Flint, 2005).

In SAGD method, two parallel horizontal wells are constructed with a 4-6 m distance between them. High-pressure steam is injected into the upper well. The steam and associated gas rise because of their low density compared to the heavy crude oil below, which makes steam not to reach to the lower production well. Steam rises and fills the space left by oil and creates a steam chamber to dissolve heavy components of crude oil and decrease oil viscosity. Oil becomes movable and can be collected through the lower well by pumping (Fig. 1.8).

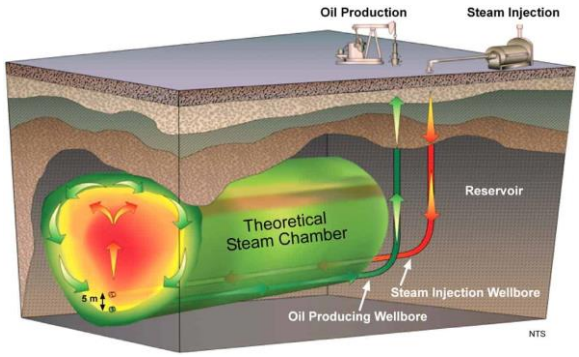

Fig. 1.8. Scheme of SAGD process (Vista Projects, 2021).

Main advantage of steam injection methods is the increase of extraction amount of oil up to 70% (Flint, 2005). Another contributing factor that enhances oil production during steam injection is related to near-wellbore cleanup (Oilfield Glossary, Schlumberger Limited). In this case, steam reduces the viscosity and dissolves paraffins and asphaltenes, creating a small solvent bank that can remove trapped oil. It is also believed that steam flooding is easier to control rather than fire flooding (in-situ combustion) (Temizel and Rodriguez, 2016). Unconventional oil resources have been widely developed by the methods in which heat is generated on the surface rather than by methods in which heat is generated in reservoir. Indeed, these methods are quite effective, however, at some points, are not efficient.

The main problems are huge energy consumption to generate high temperature water or vapor, energy losses as agent needs to be delivered to the boreholes and generation of greenhouse gases. Besides these, there were numerous cases of oil leakage as high-pressure steam injection dissolves salt which opens pass for bitumen (Inside Climate News, 2016). There are several difficulties in applying this method on a depth below 1500 m because of its high pressure.

Thermal methods using heat generated in reservoir are in-situ combustion (ISC) and Electro-Thermal Heating Method (ETHM). ISC is the oldest thermal recovery method as it has been used for nine decades (Sarathi, 1998). It is a process in which oxygen-containing gas or other air is injected into the reservoir and reacts with crude oil to create a high-temperature combustion zone. In combustion zone, gases are generated, and heated front goes through the reservoir (Fig. 1.9). ISC performs very well at deep and high-pressure reservoirs where steam is inefficient and shows have small heat losses compared to SF and CSS (Hvizdos and Howard, 1983).

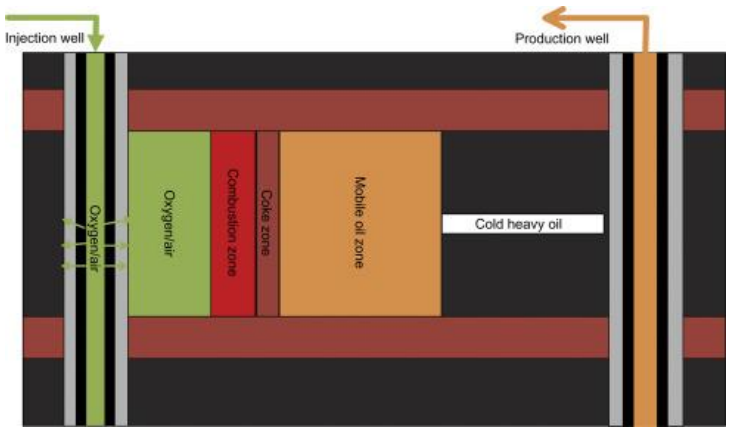

Fig. 1.9. In-situ combustion process (Zhang and Chen, 2018).

1.1.4 Electro-Thermal Heating Method

Electro-Thermal Heating Method has not been that commonly used as ISC, but it is used for heavy oil field in Canada, Venezuela and USA (Smalley, 2000), (Layrisse, 1999). The main principle of ETHM is to use electrical energy to increase temperature in the reservoir so that oil can be easily extracted. Depending on the current frequency being used, ETHM can be divided into three categories: low-frequency electrical heating (Ohmic or Joule heating), high-frequency electrical heating (microwave heating), and induction heating (IH) (Gill, 1979).

In low-frequency method, two wells with electrodes inside are used. One well represents anode and another one cathode. Because of the difference of electrical potentials between the wells, generated electrical current goes through the formation and because of Joule Heating reservoir temperature increases. The current frequency ranges used are normally from 0.1 to 60 cycles/sec. (Fig. 1.10)

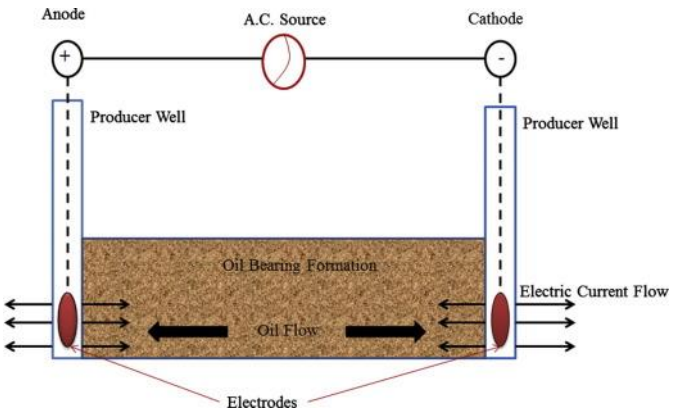

Fig.1.10. Low frequency heating (Bera and Babadagli, 2015).

High-frequency heating method with electrical current frequencies to be 300 – 300000 MHz is classified as microwave heating. These high-frequency microwaves interact with molecules of reservoir water and cause circulatory and oscillatory motion. Generated frictional heat is passed to surroundings, mainly to oil and rock, and increases the temperature of the system. The extent of temperature increase is determined by the amount of microwave energy absorbed by the fluids. For microwave heating, two wells are needed, one is for antenna which conducts microwaves and second one for production (Fig. 1.11).

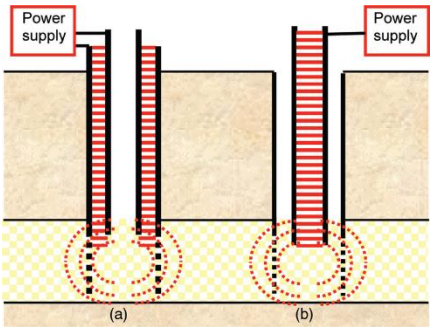

Fig. 1.11. High-frequency electromagnetic power transfer (Lake and Warner, 2007).

IH started its application from 1929. First implementation of this method in large scale experiment was carried out in the early 1980's (McGee and Vermeulen, 1996). IH frequencies range from 0 to 10 kHz. Induction coil is intertwined along the well and generates and alternates electric and magnetic fields, causing eddy currents. The flow of this eddy currents results in temperature increase in the reservoir (Fig. 1.12).

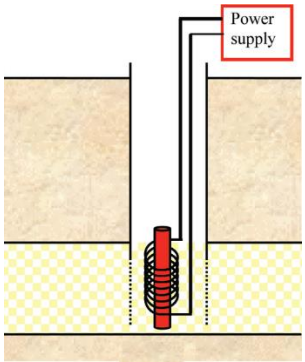

Fig. 1.12. Induction heating (Lake and Warner, 2007).

Electro-thermal heating method can be used as an alternative method to traditional EOR methods. The following advantages can be stated for ETHM (Rudnev and Loveless, 2002), (McGee and Vermeulen, 1996): heat transfer into low permeable zones of reservoir; relatively low energy

consumption; no need for special equipment of vapor distribution system; less generation of greenhouse gases. Thus, ETHM is very promising for oil sands reservoirs laying not too deep (around 200-400 m depth) (McGee and Donaldson, 2009). Despite the advantages, this method is impractical for deep reservoirs as exploitation of electrodes is difficult. Also, due to intensive heating, reservoir water can be evaporated resulting in decreased amount of water in the rock which may lead to cut off the electrical chain in the reservoir and suspension of ETHM process.

History of ETHM starts in the middle of 20th century when first steady-state model of concentrated heaters was built by Schild (1957), Schild also described first use of these heaters. Todd and Howell (1978) carried out numerical analysis based on Canadian patent of in-situ electrical heating, but they did not take into account convection effects. Physical models of conduction and inductive localized heating were built by Vermeulen and Chute (1979-1983). McPherson (1988) simulated a model of electromagnetic heating of Athabaska oil sands with varying frequencies from 60 to 250 KHz. Pizarro and Trevisan (1987) conducted an electrical heating test in the Rio Panon field in Brazil. McGee and Vermeulen (2004) described the heat and mass transfer mechanisms associated with a specific application of electrical heating, the Electro-Thermal Dynamic Stripping Process (ET-DSP), for the production of bitumen from oil sands. McGee (2009) published the results of pilot test of ET-DSP carried out in 2006-2007 in Alberta, Canada. They determined oil recovery factor, energy oil ratio, and water oil ratio. McGee and Donaldson (2009) presented a model for radial heat transfer that can be used to compare different electro-thermal heating methods. The model compares the resulting temperature distribution, the time to achieve a heated volume at some distance away from the wellbore, and the power density in the reservoir among the different electro-thermal methods. They also calculated well spacing and input power requirements for improving oil sands production process.

In this study, low-frequency heating is studied whether the method can be less energy wasteful and more environmentally friendly. Simulation model of the ETHM on Hangingstone oilsands field (Athabaska, Canada) is built for this purpose.

1.2. Objectives

The objectives of this thesis are to develop a numerical simulation model to calculate current, heat, and fluid flow in the reservoir and surrounding formations to quantitatively analyze ETHM in oil sands.

1.3. Thesis Structure

This thesis is consisted of 7 chapters. In chapter 2, fundamental physical processes are described by showing constitutive and governing equations and parameters. In chapter 3, the numerical simulation tool and numerical code is described. In chapter 4, the Hangingstone oil sands field is described. In chapter 5, ETHM simulation of Hangingstone oil sands field is conducted. In chapter 6, simulation results are analyzed and discussed. In chapter 7, conclusions of the study are presented.

Chapter 2

Theoretical Background

2.1. Description of Porous Medium

ETHM is a multiphysical process which includes two-phase flow of fluids, heat flow, and electrical current flow. All these processes happen in porous medium. Porous medium is a matrix which has solid skeletal portion and pores. Ratio of pores volume and total volume of bulk is a porosity. Porosity usually consists of effective and ineffective porosity. Porosity is called effective in the case when pores are connected to each other. Ineffective porosity represents isolated pores which are not connected to each other (Fig. 2.1). In a saturated rock where fluid flow occurs in connected pores, high effective porosity makes good filtration characteristics of rock.

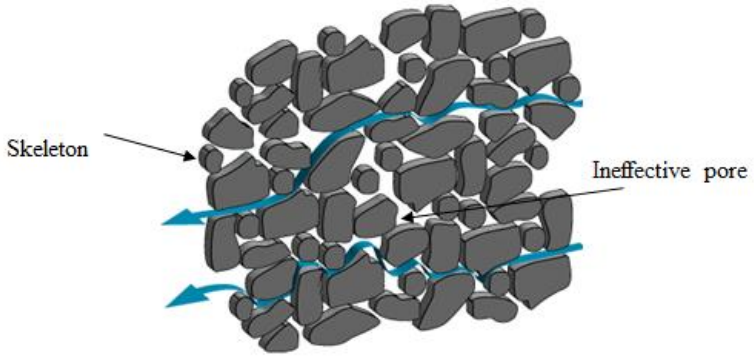

Fig. 2.1. Schematic model of porous medium (FrackOptima, 2014)

2.2. Physical Processes and Constitutive Equations

Basic physical phenomena that lie in oil the extraction process is a fluid flow which can be described by Darcy's Law (Whitaker and Stephen, 1986). Darcy's Law describes singe phase fluid flow velocity $\vec{u}$ through the porous media under a certain pressure gradient.

$$\vec{u} = -\frac{k}{\mu}\nabla(p + \rho g z) \tag{1}$$

Where k – permeability, m^2, μ – dynamic fluid viscosity, Pa·s, p – pressure, Pa, ρ – fluid density m^3/kg, g – gravitational acceleration m/s^2, z – coordinate, m.

According to this law, fluid flow occurs under pressure gradient and the direction of the flow is from high pressure towards low pressure. Fluid flow rate depends on filtration properties of porous media. Therefore, filtration rate of one fluid can be different under same pressure gradient in different porous medias. Also, fluid flow rate is highly dependent on physical properties of fluid itself, especially viscosity. The more viscous fluid, the lower flow rate. Darcy's Law is applicable only for Newtonian fluids in the cases of flow with small fluid velocity.

Buckley-Leverett problem describes two-phase oil-water flow in porous media (2). Displacement process is based on the principle that both fluids are immiscible, and flow is linear and horizontal. Comparing to single-phase flow, basic phenomena to be accounted for in two-phase flow is interaction of each fluid between each other and with porous media which can be described by relative permeabilities (3, 4). Relative permeability describes the ability of fluid to flow when other fluid is present in the same porous media. Difference of physical material properties of fluids results in different viscosities and relative permeabilities which in sum represents mobility λ (3).

$$\frac{\partial S_w}{\partial x} + \frac{\partial}{\partial x}\left(\frac{Q}{\varepsilon_p A} f_w(S_w)\right) = 0 \tag{2}$$

Where S_w – water saturation, ε_p- porosity, A – area of cross-section of flow, m^2, Q – total flow rate, m^3/s, $f_w(S_w)$ – Buckley-Leverett function.

Buckley-Leverett function is a phase flow distribution function which shows displacement process.

$$f_w(S_w) = \frac{\lambda_w}{\lambda_w + \lambda_o} = \frac{k_{rw}/\mu_w}{k_{rw}/\mu_w + k_{ro}/\mu_o} \quad (3)$$

λ_w, λ_o – mobility of water and oil, m²/Pa·s, k_{rw}, k_{ro} – relative permeabilities of water and oil, μ_w, μ_o – water and oil viscosity, Pa·s.

Relative permeability:

$$k_{rw} = \left(\frac{S_w - S_w^r}{1 - S_w^r - S_o^r}\right)^3, \quad k_{ro} = \left(\frac{1 - S_w - S_o^r}{1 - S_w^r - S_o^r}\right)^3 \quad (4)$$

Where S_w, S_o – water and oil saturation, Sw^r, So^r – residual water and oil saturation

To reach complete and full extraction of oil, the mobility ratio of oil and water should be decreased. The saturation profile of water also changes with different viscosity ratios. (Fig. 2.2). Viscosity ratio decrease can be obtained by decreasing oil's viscosity with thermal methods or increasing water's viscosity by adding polymer powder. As it was described in chapter 1.1.2, viscosity of heavy oil highly depends on its temperature. For this reason, thermal methods of oil enhancement processes are widely used as it decreases viscosity and increase mobility of oil which makes fluid flow faster.

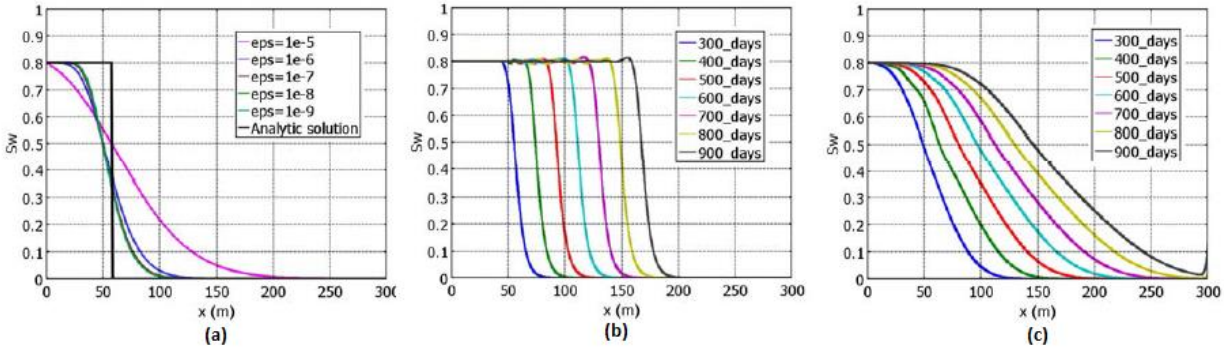

Fig. 2.2. Numerical solutions of the Buckley–Leverett problem with linear relative permeabilities and viscosity ratio (a) μ_w/μ_o =1, (b) μ_w/μ_o =2, (c) μ_w/μ_o =2/3 (Diaz-Viera and Lopez-Falcon, 2008)

Heat transfer in porous media consists of different types of heat flows, for instance, conduction of rock material, and convection by fluids fullfilling the pores (Fig. 2.3).

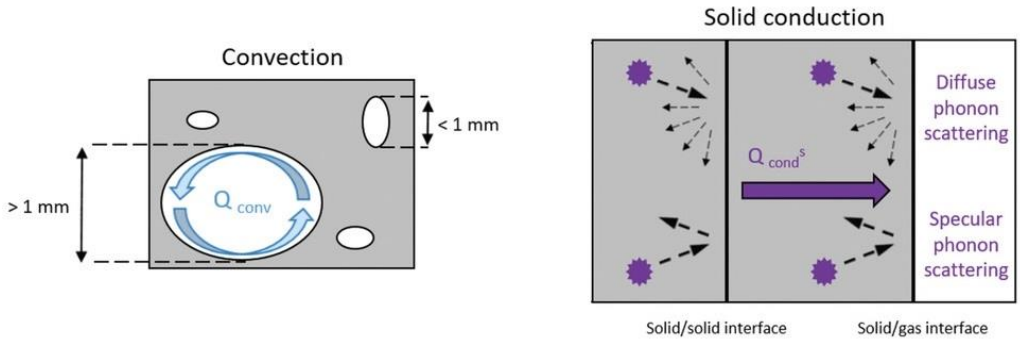

Fig. 2.3. Conduction and Convection in Porous Medium, (Apostolopoulou-Kalkavoura and Munier 2020)

Conduction is energy tranfer between materials that have physical contact. Hot and vibrating moleculs pass its energy through the neighbours heating up area around. The more density of solid phase, the more conduction of the system. Heat conduction process is described by by Fourier's Law of Thermal conduction (Bergman and Lavine, 2011). It includes relation between heat flux density and conductivity of system:

$$q = -K_{eff}\nabla T \tag{5}$$

q – heat flux density W/m^2, K_{eff} – effective conductivity of bulk, W/(m·K), ∇T - temperature gradient K/m.

Effective conductivity of bulk:

$$K_{eff} = S_w\varepsilon_p K_w + S_o\varepsilon_p K_o + (1-\varepsilon_p)K_r \tag{6}$$

K_w, K_o, K_r – effective conductivity of water, oil, and rock, W/(m·K).

Convection is a transfer of heat by movements of fluids, mainly by mass transfer. Fluid flow increases heat transfer between solid surface and the liquid (Cengel, 2002). The more effective porosity of porous media, the bigger contribution goes to convection type of heat transfer. In fluid flow processes convection is usually a dominant form of heat transfer. Also, convection usually occurs due to the boyancy effect when density of the fluid changes as the function of temperature and heated fluid floats up. However in this thesis boyancy is neglected. Convection process is described by specific heat of bulk:

$$(\rho C_p)_{eff} = S_w\varepsilon_p\rho_w C_w + S_o\varepsilon_p\rho_o C_o + (1-\varepsilon_p)\rho_r C_r \tag{11}$$

Where C_p – effective heat capacity of bulk, J/kg/K, C_r, C_w, C_o – heat capacity of rock, water and oil, J/kg/K, ρ_r, ρ_w, ρ_o – density of rock, water and oil, kg/m^3.

In ETHM heat is generated by electric current flow. Basic law which describes electric current flow is Ohm's Law (Millikan and Bishop, 1917):

$$I = \frac{V}{R} \tag{12}$$

I -electrical current through the conductor, A, V – voltage across the conductor, V, R – resistivity of conductor, Ohm.

Two electrode wells represent anode and cathode and create electric potentials difference. As a result, the electric field $\vec{E}$ is generated. The dependance between electric field $\vec{E}$ and potentials V can be described by following equation (Griffiths, 2017):

$$\vec{E} = -\nabla V \tag{13}$$

It was mentioned in chapter 1.1.4, that among different types of Electro-Magnetic Heating Low-frequency Heating (Joule Heating) is applied as main EOR method in this research. Joule Heating is a process in which heat transfer is accumulated by current flow through the material. This effect follows energy conservation principle when electrical energy transfers into heat energy. Electric potential difference of two electrodes generates electromotive force which in turn causes electrons movements in material. This movement is called electrical current. Depending on amount of free electrods and magnitude of electromotive force different materials have capability of passing electrical current but with varying degrees. Some are better of conduction electrical current and some are worse. Due to this, materials are usually divided into conductors and resistors. In Joule Heating case the less material conductivity is, the more heat generated in the system. Simply speaking, a lot of work is spent at moving electrods that hard to move and this work is directly converted in to the heat of material. Constitutive relation between current density J and electric field-E can be described by following equation (AC/DC Module User's Guide, COMSOL, 2020):

$$J = \sigma E + \frac{\delta D}{\delta t} \tag{14}$$

Where σ – electrical conductivity, S/m, D – electric displacement C/m^2.

Constitutive relation D-E (AC/DC Module User's Guide, COMSOL, 2020):

$$D = \varepsilon_0\varepsilon_r E \tag{15}$$

ε_0 – relative permettivity of vacuum, ε_r – relative permettivity of material

Archie's Law describes electrical conductivity of porous media (Archie, 1942):

$$\sigma = S_w^n \varepsilon_p^m \sigma_w \tag{16}$$

σ – electrical conductivity, S/m, S_w – water saturation, ε_p – porosity, σ_w – electrical conductivity of fluid, S/m, n – saturation exponent, m – cementation exponent.

2.3. Governing Equations

Heat flow is described by energy conservation equation:

$$(C_p\rho)_{eff}\frac{\partial T}{\partial t} + \sum_{i=1}^{2} \rho_i C_i u_i \cdot \nabla T + \nabla \cdot q = Q_{j.v} \tag{17}$$

$(C_p\rho)_{eff}$ – specific heat of bulk, C_i – heat capacity of i-phase, u_i – velocity of i-phase, which is described by Darcy's Law, q – heat flux density described by Fourier's Law of Thermal Conductivity, $Q_{j.v}$ – total electric charge.

Electric current flow is described by charge conservation Law:

$$\nabla \cdot J = Q_{j,v} \tag{18}$$

Mass conservation equation describes fluid flow:

$$\frac{\partial \varepsilon_p \rho_i s_i}{\partial t} + \nabla \cdot \rho_i u_i = 0 \tag{19}$$

Where ρ_i, s_i and u_i – density, saturation, and velocity of i-phase

2.4. Parameters

Table of parameters is presented in Table 1. The values of porosity, permeability, density, water and bitumen saturation, heat capacity and thermal conductivity of rocks and fluids were set according to previous experiment (McGee and Donaldson, 2009) and field data (AER Hangingstone Project Update, 2020). Water injection rate and current density values were determined during simulation.

Table 2.1. Material properties and physical parameters

Name of parameter	Designation	Definition
Porosity of sands	ε_p^s	0.35
Porosity of mudstone	ε_p^m	0.2
Porosity of limestone	ε_p^L	0.3
Density of sands	ρ_r, kg/m3	2250
Density of mudstone	ρ_m, kg/m3	2000
Density of limestone	ρ_L, kg/m3	2000
Density of bitumen	ρ_o, kg/m3	1000
Density of water	ρ_w, kg/m3	1000
Initial saturation of water in mudstone	s_w^m	1
Initial saturation of water in limestone	s_w^L	1
Initial saturation of water in sands	s_2^0	0.28
Residual water saturation in sands	S_w^r	0.2

Name of parameter	Designation	Definition
Residual oil saturation in sands	S_o^r	0.2
Water injection rate	u_2^{inj}, m/s	$1.11 \cdot 10^{-5}$
Dynamic viscosity of water	μ_2, Pa·s	0.001
Horizontal permeability of sands	k_x, m^2	$3.9 \cdot 10^{-12}$
Horizontal permeability of sands	k_y, m^2	$3.2 \cdot 10^{-12}$
Permeability of mudstone	k_m, m^2	$1 \cdot 10^{-18}$
Permeability of limestone	k_L, m^2	$1 \cdot 10^{-15}$
Electric conductivity of mudstone	σ_m, S/m	0.033
Electric conductivity of limestone	σ_L, S/m	0.014
Electric conductivity of water	σ_w, S/m	1.421
Saturation exponent	n	2
Cementation exponent	m	1.37
Water injection temperature	T_{ing}, °C	13.57
Thermal capacity of mudstone	C_m, $J/(kg \cdot K)$	1700
Thermal capacity of limestone	C_L, $J/(kg \cdot K)$	1700
Thermal capacity of sands	C_s, $J/(kg \cdot K)$	875.56
Thermal capacity of water	C_w, $J/(kg \cdot K)$	4184
Thermal capacity of bitumen	C_o, $J/(kg \cdot K)$	1700
Heat conductivity of water	k_w, W/m·K	0.58
Heat conductivity of bitumen	k_w, W/m·K	0.17
Heat conductivity of mudstone	k_m, W/m·K	3
Heat conductivity of limestone	k_L, W/m·K	2.5
Heat conductivity of sands	k_r, W/m·K	2.63
Ground potential	V_0, V	0
Current density	J, A/m^2	6
Relative permittivity of vacuum	ε_0	1
Relative permittivity of water	ε_r	80

Chapter 3

Methodology

3.1. Description of Numerical Code

COMSOL Multiphysics (Porous Media Flow Module, COMSOL, 2020) is a numerical tool which includes all steps of building a numerical model – defining geometry, material properties, initial and boundary conditions, and physics. COMSOL Multiphysics has many modules as fluid flow and heat transfer module, electromagnetics module, structural mechanics and acoustics module, chemical engineering modules. It well performs for physics coupled processes and gives reasonable results.

The Porous Media Flow Module is a package that includes customized physics interfaces for the analysis of transport processes in porous media. It combines physics interfaces for fundamental processes with structural mechanics and electromagnetics analyses. Heat transfer and chemical transport can be calculated for liquid, solid ad gas phases. The Richards' Equation interface of Fluid Flow branch describes nonlinear flow in variably saturated porous media. Darcy's Law interface is used for slow flow in saturated porous media and the Brinkman Equations interface where flow shear is nonnegligible. The Laminar Flow interface is used for free flows with help of Navier–Stokes equations, and the Fracture Flow interface is used for modeling flow along thin layers and fractures. This module also treats the chemical transport in solid, liquid and gas phases for free and porous media flows with the Chemical Species Transport branch (Porous Media Flow Module, COMSOL, 2020).

The Heat Transfer Interfaces calculate the temperature distribution in solids, fluids, and fluid-solid systems. The Mechanisms for Heat Transfer physics interfaces to estimate effective properties in multicomponent systems. The Heat Transfer Interfaces include heat transfer by conduction and convection. Also, Surface-to-ambient radiation effects around edges and boundaries can also be taken into account. The Heat Transfer in Porous Media Interface calculates heat transfer with and without fluid flow. The convective velocity can be set. Dispersion or spreading of heat from small-scale velocity variations can be estimated.

The AC/DC (alternative current and direct current) Module is used to create electric and magnetic fields in static, low-frequency, and transient applications. It allows to quickly and accurately predict electromagnetic field distributions, electromagnetic forces, and power dissipation in a specified design. Simulation in COMSOL helps predict phenomena which is hard to measure in laboratory experiments, so destructive and hazardous conditions can be avoided.

The AC/DC Module includes stationary and dynamic electric and magnetic fields in two-dimensional and three-dimensional spaces. All modeling formulations are based on Maxwell's equations and material laws like Ohm's law for charge transport. AC/DC Module has several physics interfaces, referred to as AC/DC interfaces, which allow you to set up and solve electromagnetic models. The AC/DC interfaces include electrostatics, DC current flow, magnetostatics, AC and transient current flow, AC and transient magnetodynamics, and AC electromagnetic (full Maxwell) formulations.

3.2. Trial Simulations

I simplified the problems of the Electro-Thermal Heating process into several processes. Simulation of each case was considered, which are listed in the Table 1. It is important to mention that my model is simplified by omitting capillary pressure and evaporation.

Table 3.1. ETHM problems

Problem	Type
Fluid flow	Single phase flow
	Two-phase flow
Heat transfer	Conduction (no flow)
	Conduction + convection (single phase flow)
	Conduction + convection (two-phase flow)
Joule Heating	No flow (porous media)
	Two-phase flow

Mesh

Mesh structure is shown in Fig. 3.1. Length is 300 m and height is 40 m. On the left border I set the finer mesh size to obtain detailed results. The maximum size of cell is 11 m and the minimum size is 3.75 cm. Edge element number is 78 and vertex element number is 4. Total element number is 140.

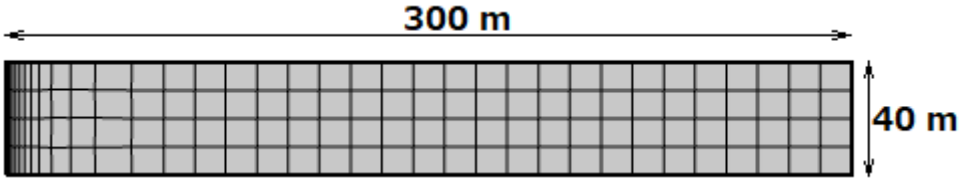

Figure 3.1. Mesh structure

3.2.1 Single Phase Flow

The first case represents one phase water flow injected from the left boundary and outflow on the right boundary. The model parameters used are listed in the Table 3.2. Initial conditions are the initial pressure in the reservoir, boundary conditions are on the left boundary mass inlet flow with fixed velocity value, on the right border – fixed pressure value equal to the initial reservoir pressure (Fig. 3.2).

Table 3.2. Single phase flow parameters

Name of parameter	Dimension	Definition
Initial pressure p_0	kPa	600
Permeability k	m^2	10^{-12}
Length, L	m	300
Height, H	m	40
Porosity, ε_p	-	0.35
Velocity, u	m/s	$2.89 \cdot 10^{-7}$
Density, ρ	kg/m^3	1000
Viscosity, μ	Pa·s	$8.9 \cdot 10^{-4}$

Equations that is applied in COMSOL are mass conservation equation and Darcy's Law:

$$\frac{\partial}{\partial t}(\varepsilon_p \rho) + \nabla \cdot (\rho u) = 0 \tag{13}$$

$$u = -\frac{k}{\mu}\nabla p \tag{14}$$

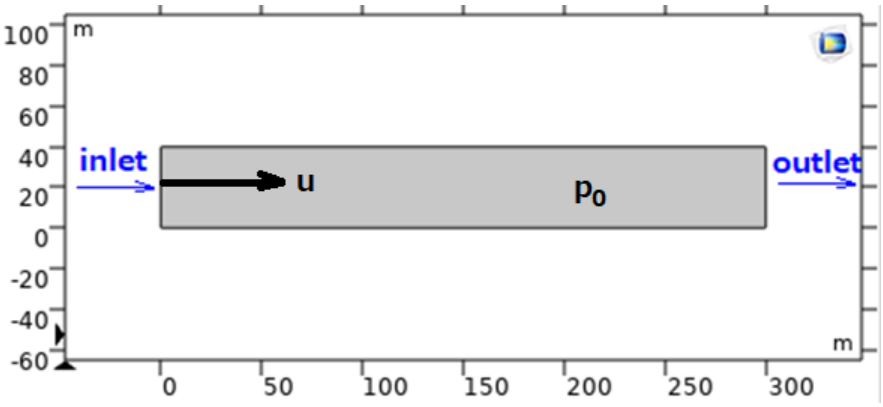

Figure 3.2. Single phase flow scheme

Figure 3.3 shows the results of this simulation. Due to the fixed initial and boundary conditions and the absence of another phase, we can see that pressure showed linear decrease from the inlet to the outlet, and velocity is constant. This means that the flow is stable, does not change with the time.

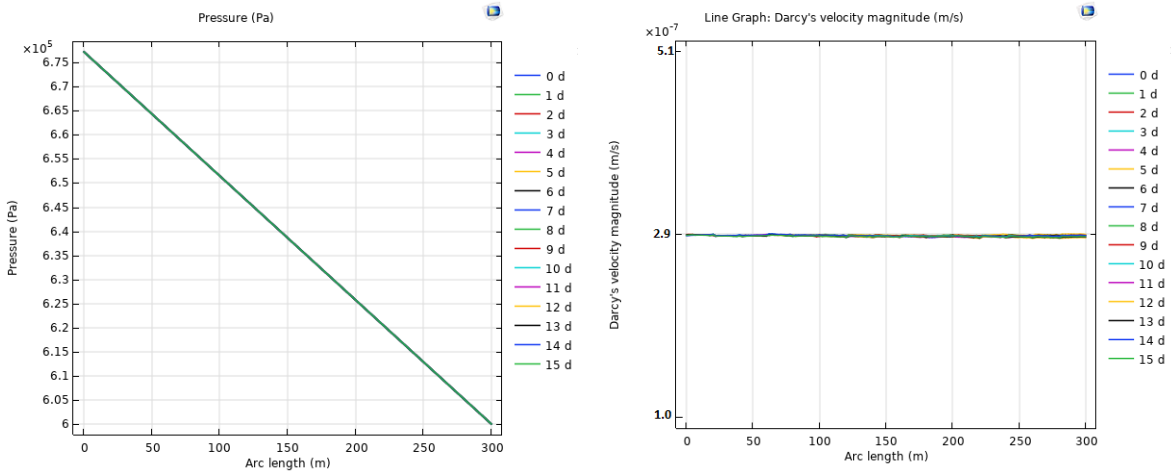

(a) (b)

Figure 3.3. Single phase flow scheme (a) pressure (b) Darcy's velocity

3.2.2 Two-Phase Flow

This case represents two-phase flow with water injected from the left border into the porous media of which initial oil saturation to be 80% and water saturation to be 20%. Used in this model parameters are listed in the table 3.3. Initial conditions are the initial pressure in the reservoir and initial water and oil saturations (*So*, *Sw*), boundary conditions are on the left boundary mass inlet flow with fixed velocity value and fixed water saturation value (*Sw*=1), on the right border – fixed pressure value equal to the initial reservoir pressure (Fig. 3.4).

Table 3.3. Two-phase flow parameters

Name of parameter	Dimension	Definition
Initial pressure, p_0	kPa	600
Permeability, k	m^2	10^{-12}
Length, L	m	300
Height, H	m	40
Initial oil saturation, So	-	0.8
Initial water saturation, Sw	-	0.2
Porosity, ε_p	-	0,35
Fluid velocity, u	m/s	$2.89 \cdot 10^{-7}$
Density of oil, ρ_o	kg/m^3	1000
Density of water, ρ_w	kg/m^3	1000
Viscosity of oil, first case μ_o^1	Pa·s	0.01
Viscosity of oil, second case μ_o^2	Pa·s	0.001
Viscosity of water, μ_w	Pa·s	0.001

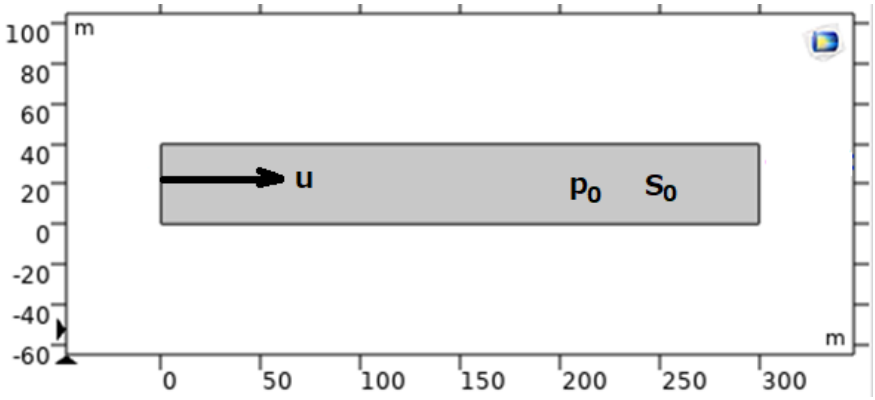

Figure 3.4. Two-phase flow scheme

Equations that is applied in COMSOL are mass conservation equation (15), Darcy's Law for each phase i (16) and system and relative permeabilities of both phases (17):

$$\frac{\partial \varepsilon_p \rho_i s_i}{\partial t} + \nabla \cdot (\rho_i u_i) = 0 \tag{15}$$

$$u_i = -\frac{k_{ri}}{\mu_i} k \nabla p \tag{16}$$

$$k_{ri} = s_i^3 \tag{17}$$

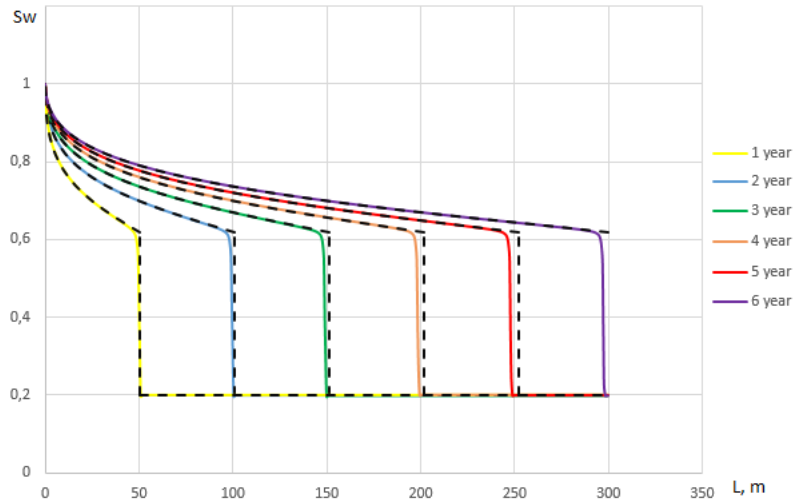

Figure 3.5. Comparison of water saturation profile for *μo/μw=1* COMSOL simulation (solid lines) and analytical solution (dashed lines)

Figure 3.5 shows the comparison between COMSOL simulation results which are represented by solid lines and analytical solution by dashed lines. Total time of simulation is 6 years, and we can see that COMSOL reasonably represents analytical solution. However, as time goes by, some divergence of results between COMSOL and analytical solution occurs. The difference of displacement front does not exceed 2 m, which can be neglected. This comparison allows us to rely on COMSOL's results in two-phase flow simulation.

I did two subcases: first one is for *μo/μw*=10 and second is for *μo/μw*=1 to make it sure that displacement process follows Buckley-Leverett distribution. On the right-side graphic volume fraction of water (Fig. 3.6), we can see that displacement process of fluids with equal viscosities resembles Buckley-Leverett. On the left-side graphic with ten times difference of viscosities we can see that the water saturation profiles are flatter which tells that sufficient amount of oil left unextracted. Comparing these two subcases it can be said that extraction of oil in the case of equal viscosities (μo/μw=1) is more complete rather than 10 times different viscosities (*μo/μw*=10).

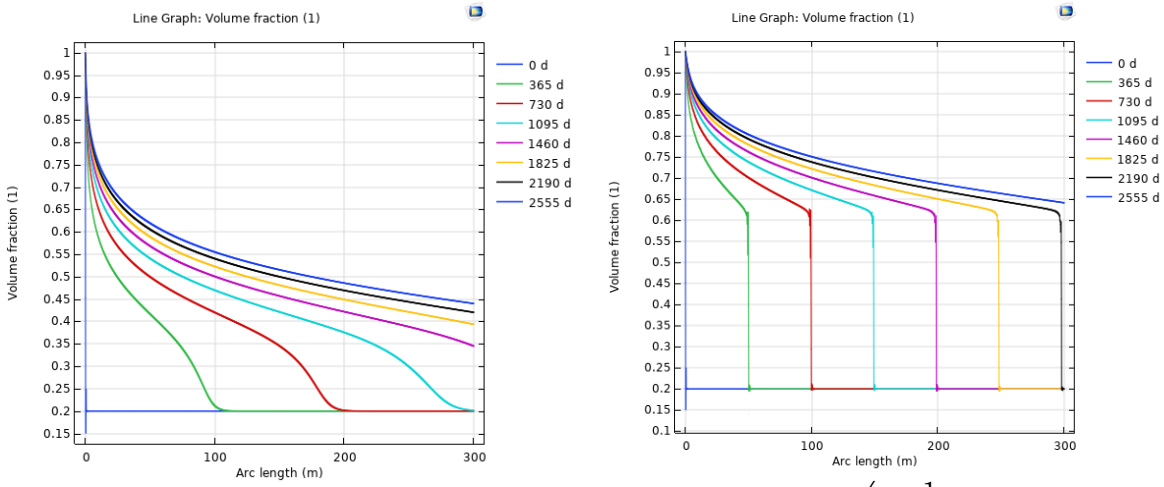

μo/μw=10 *μo/μw*=1

Figure 3.6. Water saturation profiles in case of different fluid viscosities *μo/μw*=10 and equal *μo/μw*=1 viscosities

On the graphics of pressure profiles, we can observe two different phenomena. As we fixed the right border to be constant pressure, on the graphics it does not change. Still on the left border it changes differently. In the case of equal viscosities (*μo/μw*=1), we can see that the value of pressure on the left border raises (Fig. 3.7). It can be explained by the fact that displacement process is more complete due to equal viscosities. In this case, more bitumen was extracted from the formation.

As for the case of different viscosities ($\mu o/\mu w$=10) we can see that the pressure drops. It is because extraction fluid is too viscous so the injected fluid cannot expel all amount of oil. That is how water breaks its path through the reservoir, and most of the amount of water goes through its path, leaving behind amounts of "immovable" oil. This phenomenon causes pressure drop in the system.

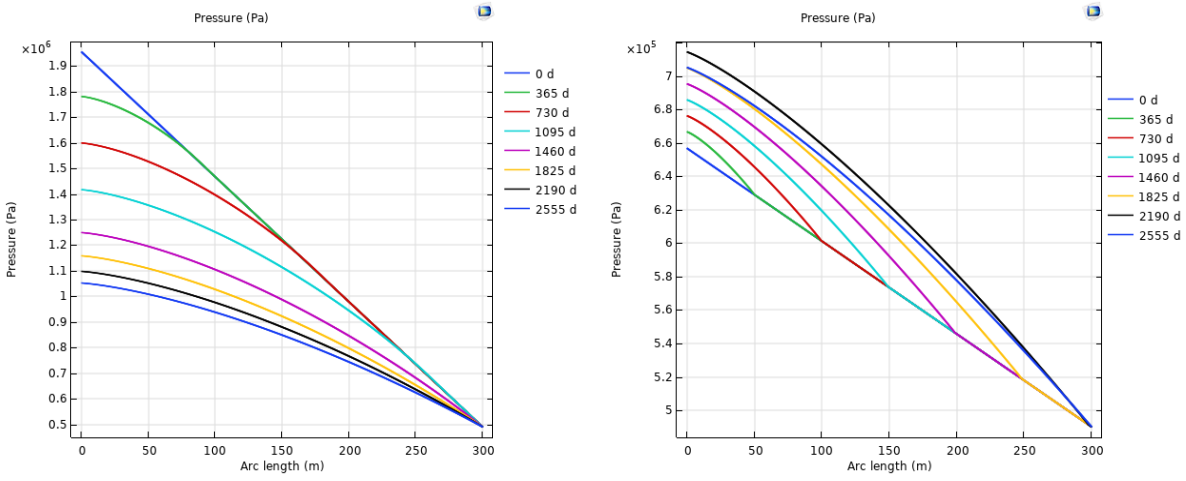

$\mu o/\mu w$=10 $\mu o/\mu w$=1

Figure 3.7. Pressure profiles in case of different fluid viscosities $\mu o/\mu w$=10 and equal viscosities $\mu o/\mu w$=1

It is well known that to increase the amount of extracted oil the viscosity value of injected fluid must be as close to the viscosity value of extraction fluid. That is why adding to the water thickening agents (ex. polymer) can partly solve the problem. However, the most popular method is to decrease the viscosity of extraction fluid by using thermal methods. These thermal effects are considered in the cases below.

3.2.3 Heat Conduction (No Flow)

This case represents heat transfer in porous media without any flow. Only water is existing in the pores of the rock. Used in this model parameters are listed in the table 3.4. Initial conditions are the initial temperature in the reservoir (T_0), boundary conditions are on the left border fixed Temperature (T=100°C), on the other borders – thermal isolation (Fig. 3.8).

Table 3.4. Heat conduction problem parameters

Name of parameter	Dimension	Definition
Initial temperature, T_0	°C	10
Porosity, ε_p	-	0,35
Density of rock, ρ_r	kg/m^3	2250
Thermal conductivity of rock, k_r	W/m/°C	2.63
Thermal capacity of rock, C_r	J/(kg·°C)	743
Length, L	m	300
Height, H	m	40
Density of water, ρ_w	kg/m^3	1000
Thermal conductivity of water, k_w	W/m/°C	0.58
Thermal capacity of water, C_w	J/(kg·°C)	4180

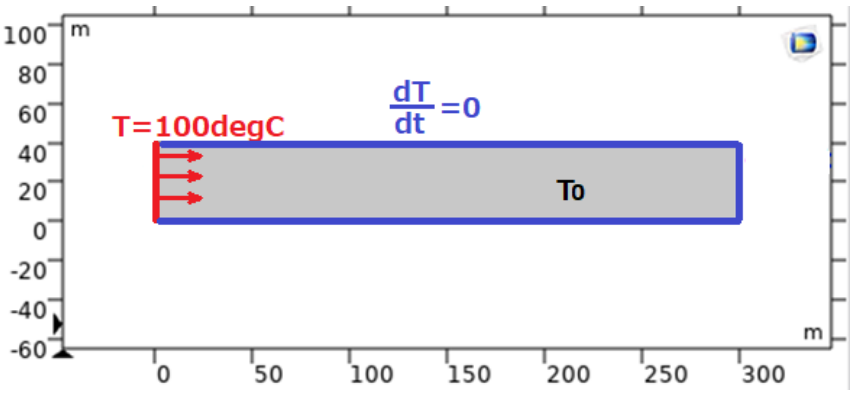

Figure 3.8. Heat conduction model scheme

Equations that are applied in COMSOL are Fourier's Law of thermal Conduction (4) energy conservation equation (5). In conduction case no flow occurs, thus the term with u is equal to zero ($\sum_{i=1}^{2} \rho_i C_i u_i \cdot \nabla T = 0$). The equations are simplified.:

$$\left(\rho C_p\right)_{eff} \frac{\partial T}{\partial t} + \nabla \cdot q = 0 \tag{18}$$

$$q = -K_{eff} \nabla T \tag{19}$$

$$\left(\rho C_p\right)_{eff} = \varepsilon_p \rho_w C_w + \left(1 - \varepsilon_p\right) \rho_r C_r \tag{20}$$

$$K_{eff} = \varepsilon_p k_w + \left(1 - \varepsilon_p\right) k_r \tag{21}$$

Figure 3.9 shows the comparison of simulation results and numerical solution results of conduction problem without fluid flow. We can see that COMSOL ideally represents analytical solution results. Looking at the temperature profile, it is clear that in 10 years of constant heating, temperature raising front hardly reached point of 50 meters (Fig. 3.9). It can be said that temperature change pace is quite slow. It is because convection is not involved into the heat transfer process.

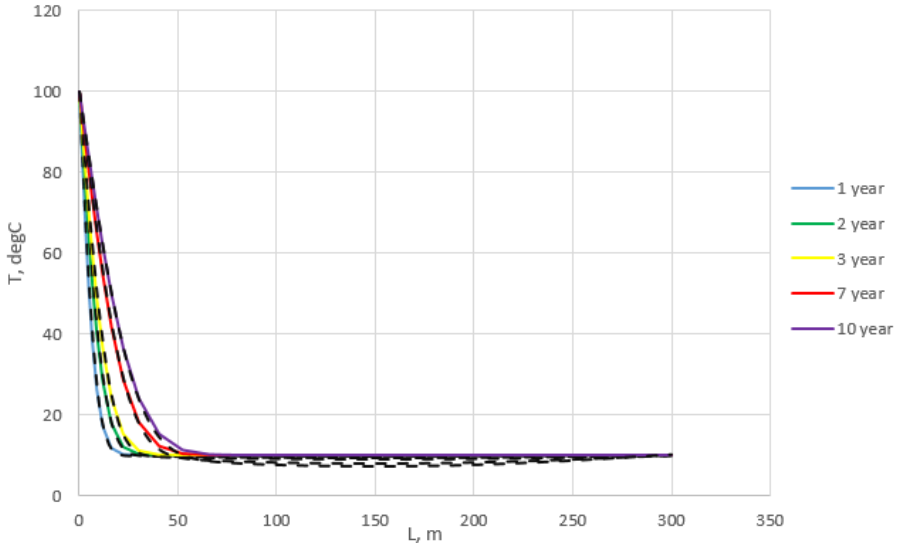

Figure 3.9. Comparison of temperature profile of conduction problem without fluid flow COMSOL simulation (solid lines) and analytical solution (dashed lines)

3.2.4 Conduction and Convection (Single Phase Flow)

This case represents heat transfer in porous media with inlet single phase flow (water). Water is existing in the pores of the rock and injected through the left border with the temperature T=100°C. Used in this model parameters are listed in the table 3.5. Initial conditions are the initial temperature in the reservoir (T_0), initial pressure (p_0) (Fig. 3.10). Boundary conditions are on the left border - fixed

Temperature (T=100°C), inlet water flow with constant injection velocity u, on the right border – heat outflow and fixed pressure equal to the initial pressure (p_0). On the horizontal up and down borders – no flow and thermal insulation. In simply terms, this case describes the heat transfer profile when hot water is injected into the porous media.

Table 3.5. Heat conduction and convection problem parameters

Name of parameter	Dimension	Definition
Initial temperature, T_0	°C	10
Initial pressure, p_0	kPa	600
Porosity, ε_p	-	0,35
Density of rock, ρ_r	kg/m^3	2250
Thermal conductivity of rock, k_r	W/m/°C	2.63
Thermal capacity of rock, C_r	J/(kg·°C)	743
Length, L	m	300
Height, H	m	40
Density of water, ρ_w	kg/m^3	1000
Thermal conductivity of water, k_w	W/m/°C	0.58
Thermal capacity of water, C_w	J/(kg·°C)	4180
Water injection velocity, u	m/s	$2.89 \cdot 10^{-7}$
Water viscosity, μ_w	Pa·s	0.001
Density of water, ρ_w	kg/m^3	1000

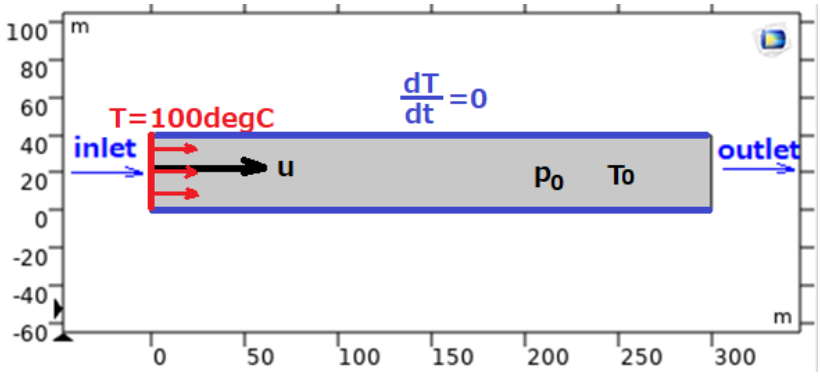

Figure 3.10. Heat conduction and convection model scheme

System of equations that is applied in COMSOL is similar to the previous cases and consist of mass conservation equation, Darcy's Law and energy conservation equation. In this case both conduction and convection are involved into heat transfer process. COMSOL takes the value of convection velocity from Darcy's velocity u:

Mass conservation equation and Darcy's Law:

$$\frac{\partial \varepsilon_p \rho_w}{\partial t} + \nabla \cdot \rho_w u = 0 \tag{22}$$

$$u = -\frac{k}{\mu_w} \nabla p \tag{23}$$

Energy conservation equation:

$$\left(C_p\rho\right)_{eff}\frac{\partial T}{\partial t}+\sum_{i=1}^{2}\rho_i C_i u_i\cdot\nabla T+\nabla\cdot q=0 \tag{24}$$

$$q=-K_{eff}\nabla T \tag{25}$$

$$\left(\rho C_p\right)_{eff}=\varepsilon_p\rho_w C_w+\left(1-\varepsilon_p\right)\rho_r C_r \tag{26}$$

$$K_{eff}=\varepsilon_p k_w+\left(1-\varepsilon_p\right)k_r \tag{27}$$

On the temperature graphics below (Fig. 3.11), we can see significant change comparing to no flow conduction case. After 10 years of injecting hot water at the point of 50 meters the temperature raised up to 95°C. This proves the fact that convection gives a greater contribution to the heat transfer process, which is essential in petroleum engineering. Also, the graphics of Darcy's velocity and pressure distribution (Fig. 3.12) show us that the flow is stable. It is because no other fluid phase is involved into the filtration process.

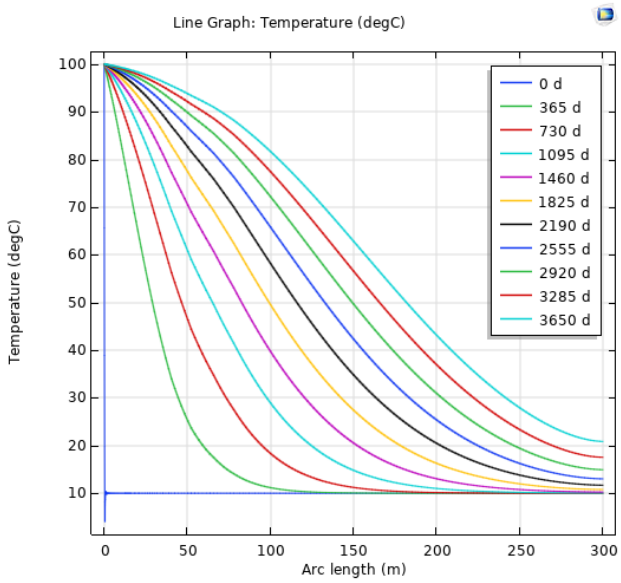

Figure 3.11. Temperature profile

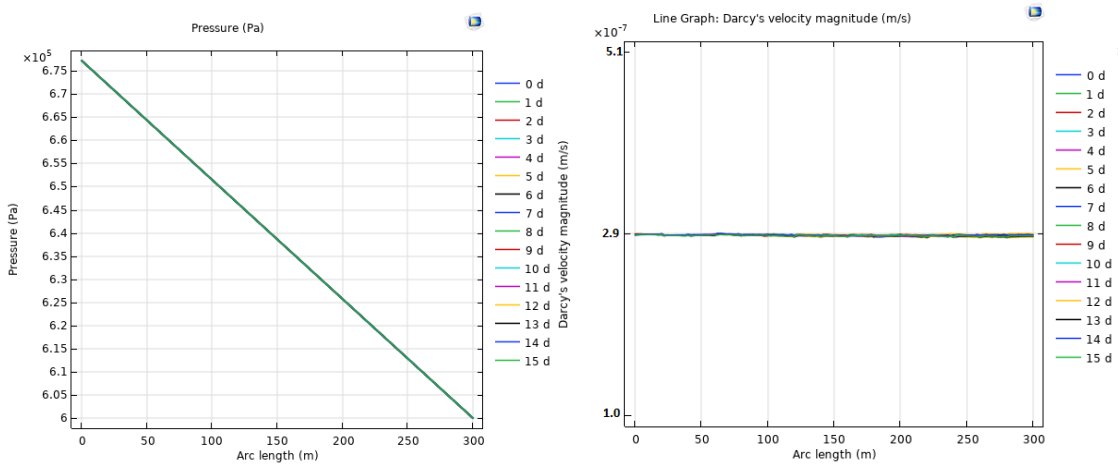

(a) (b)

Figure 3.12. Pressure (a) and water flow velocity (b) profiles

3.2.5 Conduction and Convection (Two-Phase Flow)

This case represents heat transfer in porous media with inlet water phase flow into high viscous oil saturated rock. In the pores of rock material both phases water and oil exist. Hot water (T=100°C) is injected through the left border. It transfers heat to the oil, decreasing its viscosity (Fig. 3.13). The oil viscosity distribution in dependence of temperature (Fig. 3.14) is described by the interpolation showed on the picture below. Initial oil viscosity is 130 Pa·s which is 10^5 bigger than water viscosity (0.001 Pa·s). The parameters sed in this model are listed in the table 3.6. Initial conditions are the initial temperature in the reservoir (T_0), initial pressure (p_0) and initial water and oil saturation (S_w^0, S_o^0) (Fig. 3.13). Boundary conditions are on the left border - fixed Temperature (T=100°C), inlet water flow with constant u velocity value, on the right border – heat outflow and fixed pressure equal to the initial pressure (p_0). On the horizontal up and down borders – no flow and thermal insulation.

Table 3.6. Two-phase thermal flow problem parameters

Name of parameter	Dimension	Definition
Initial temperature, T_0	°C	10
Initial pressure, p_0	kPa	600
Porosity, ε_p	-	0,35
Density of rock, ρ_r	kg/m^3	2250
Thermal conductivity of rock, k_r	W/m/°C	2.63
Thermal capacity of rock, C_r	J/(kg·°C)	743
Length, L	m	300
Height, H	m	40
Density of water, ρ_w	kg/m^3	1000
Thermal conductivity of water, k_w	W/m/°C	0.58
Thermal capacity of water, C_w	J/(kg·°C)	4180
Water injection velocity, u	m/s	$2.89 \cdot 10^{-7}$
Water viscosity, μ_w	Pa·s	0.001
Density of water, ρ_w	kg/m^3	1000
Initial water saturation, S_w^0	-	0.2
Initial oil saturation, S_o^0	-	0.8
Density of oil, ρ_o	kg/m^3	1000
Thermal conductivity of oil, k_o	W/m/°C	0.17
Thermal capacity of oil, C_o	J/(kg·°C)	2000

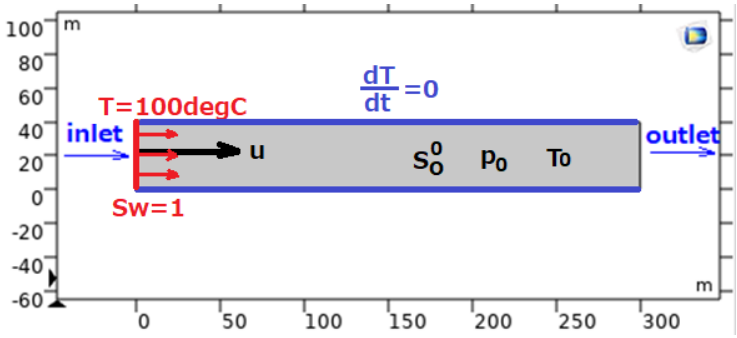

Figure 3.13. Two-phase thermal flow model scheme

System of equations that is applied in COMSOL is similar to the previous cases and consist of mass conservation equation (15), Darcy's Law for each phase (16), relative permeability equations (17) and energy conservation equations (24-27). In this case both conduction and convection are involved into heat transfer process. COMSOL takes the value of convection velocity from Darcy's velocity u.

Initial oil viscosity is 130 Pa·s at 10°C and when temperature reaches 140°C viscosity decreases to 0.0042 Pa·s (Souraki and Ashrafi, 2012). This data is presented in Fig. 3.14.

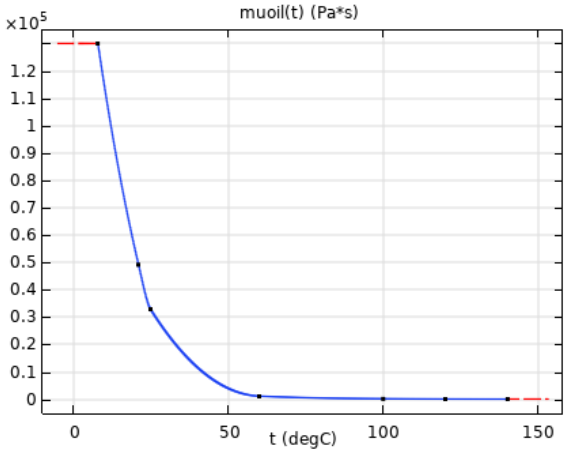

Figure 3.14. Oil viscosity dependance on temperature

Comparing temperature profile to the single-phase thermal flow case we can see that heat transfer slowed down (Fig. 3.15). It is because additional phase (oil) was considered in the system. Now the heat, that the hot water brings to the system, goes to heat up the oil and surrounding rocks. Heat capacity of oil (C_o) is bigger than rock's (C_r), which means that oil need more energy than rock to change its temperature. This effect slows heat transfer process in the rock fracture.

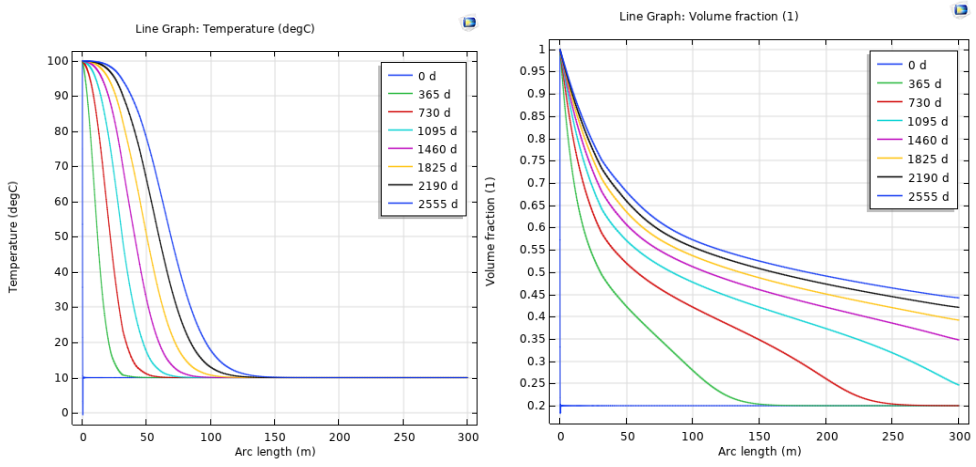

(a) (b)

Figure 3.15. Temperature (a) and water saturation (b) profiles

Analyzing water saturation profile (Fig. 3.15), it is essential to know that the integral of the water saturation graphic determines the amount of oil extracted by this time. Comparing to case of two-phase flow without heating, we can see that the amount of oil extracted during heating is more than the amount of oil without heating (Fig. 3.16). This is because the heat decreased oil viscosity as it is shown on the oil viscosity interpolation graphic. Oil with decreased viscosity is more mobile so the amount of extracted oil increases.

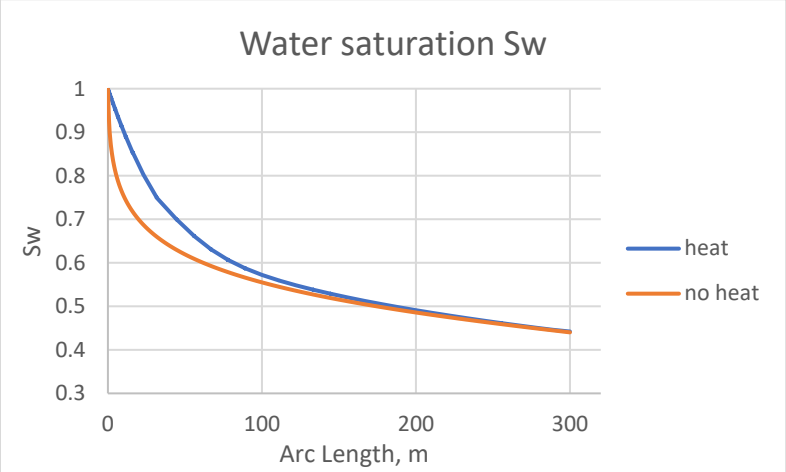

Figure 3.16. Water saturation profiles

Looking on the graphics of velocity (Fig. 3.17), we can say that the flow is almost stable, in the beginning some fluctuations occur when water starts interacting with oil and pressure profile changes. As for the pressure, relative permeabilities of both phases are changing and the amount of water on the left border increasing. These effects result in pressure decreasing on the inlet boundary (Fig. 3.17).

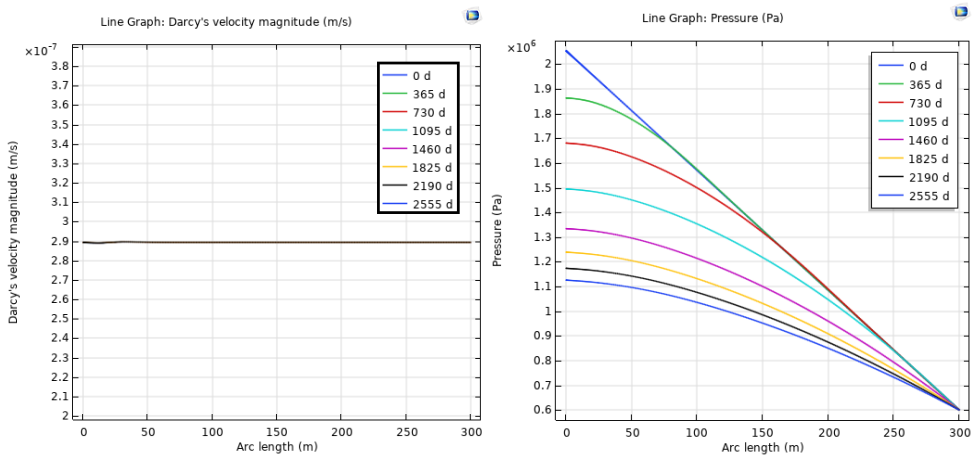

(a) (b)

Figure 3.17. Darcy's velocity (a) and pressre gradient (b) profiles

3.2.6 Joule Heating (No Flow)

This module describes the fundamental process on which the whole electro-thermal heating method based. Principle of Joule Heating is to produce heat by passing electrical current through the rock. During simulation, no heat losses were considered.

This case represents heat transfer in porous media without any flow. Rock is saturated by the water only. On the left border electrical current supplied (Fig. 3.18). Used in this model parameters are listed in the table 3.7. Initial conditions are the initial temperature in the reservoir (T_0) and ground electrical potential (V_0=0 V). Boundary conditions are on the inlet boundary - fixed Electrical current (I), on the outlet boundary – ground potential (V_0=0 V). Electric and thermal insulations are shown on the figure 3.18.

Table 3.7. Joule Heating (no flow) problem parameters

Name of parameter	Dimension	Definition
Initial temperature, T_0	°C	10
Porosity, ε_p	-	0,35
Density of rock, ρ_r	kg/m^3	2250
Thermal conductivity of rock, k_r	W/m/°C	2.63
Thermal capacity of rock, C_r	J/(kg·°C)	743
Length, L	m	300
Height, H	m	40
Density of water, ρ_w	kg/m^3	1000
Thermal conductivity of water, k_w	W/m/°C	0.58
Thermal capacity of water, C_w	J/(kg·°C)	4180
Electric current density, I	A/m^2	1
Cementation exponent, m	-	1.37
Saturation exponent, n	-	2
Water electric conductivity	S/m	1.421

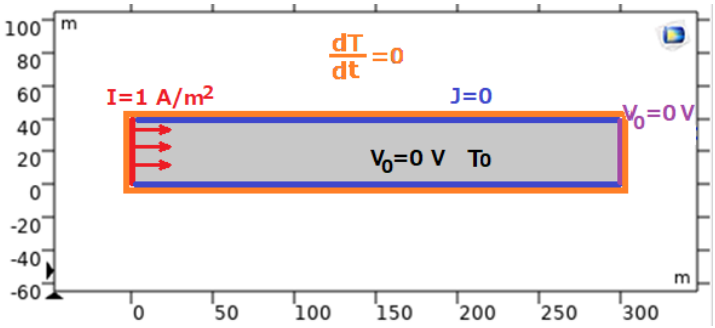

Figure 3.18. Joule Heating model scheme

System of equations that is applied in COMSOL is consist of energy conservation equation (5), specific heat of bulk (11), effective conductivity of bulk (12), Fourier's Law of Thermal conduction (4), charge conservation equation (7), constitutive relation between current density J and electric field-E (2, 3) and Archie's Law (8).

This case is divided into two subcases, all the initial and boundary conditions are the same except the initial condition of water saturation: first case – Sw=0.2 and second case Sw=0.8. The main point of this is to see how the electrical field and temperature distribution change depending on water saturation of the porous media.

Subcase 1 - Sw=0.2

On the graphics below we can see that the graphics of current density of the system, difference of electrical potential and conductivity do not change due to the initial and boundary conditions (Fig. 3.19). Checking temperature profile, we can see that for one month temperature raised from 10°C to the 85°C.

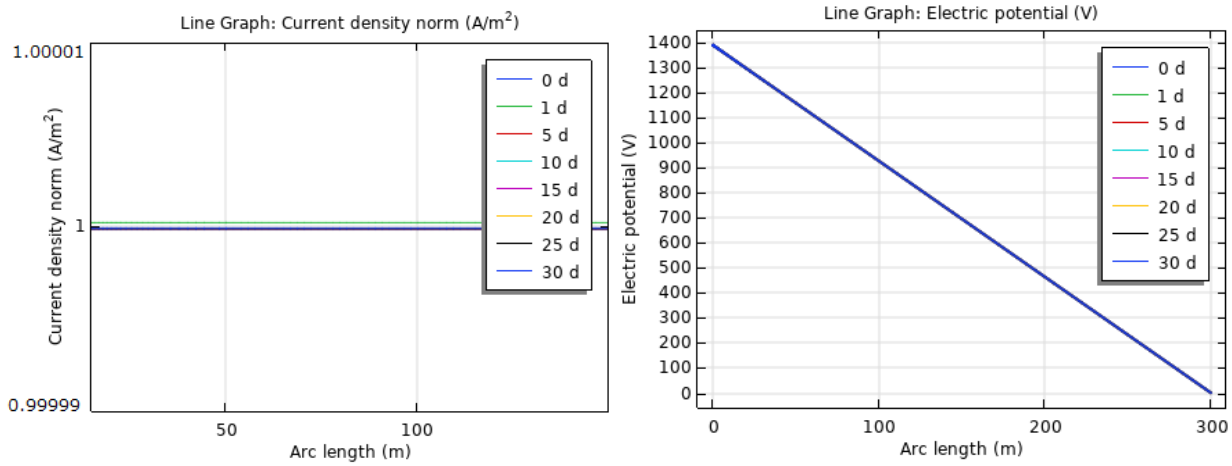

(a) (b)

Figure 3.19. Electric current density (a) and electric potential (b) profiles

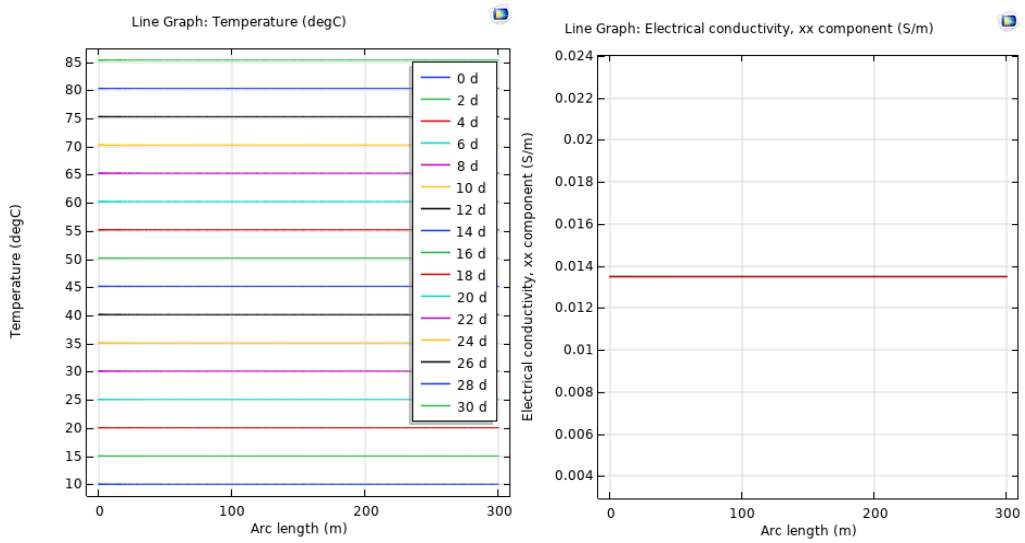

(a) (b)

Figure 3.20. Temperature (a) and electrical conductivity (b) profiles

Subcase 2 - Sw=0.8

Analyzing results, we can see that the density current remained the same as it set in the boundary conditions. However, other parameters have changed. First, electrical conductivity (Fig. 3.20 (b)) has raised, because water saturation raised. In this model porous media consists of sand and water. Sand is dielectric material and water is conductor. So, the more amount of water in the system, the more conductivity of the system (the less resistivity). The less resistivity of the system the less electric potential difference. For this reason, electrical potential difference decreased. In temperature graphics (Fig. 3.20 (a)), according to Joule Heating principle, the more resistivity of the system the more temperature raising occurs. In this subcase water saturation has raised which led to decreasing of the system resistivity and as a result small temperature raising. During one month of heating temperature changed from 10°C to the 14.7°C (Fig. 3.21 (b)).

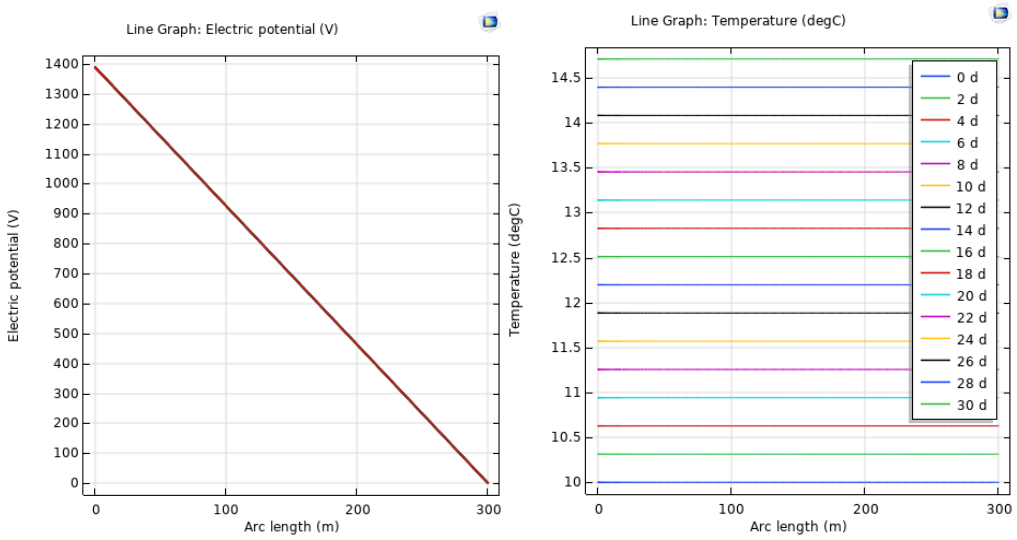

(a) (b)

Figure 3.21. Electric potential (a) and temperature (b) profiles

All in all, through the simulation and comparing simple models, it is determined that the more water in the system, the less temperature raising. This is the main point which should be considered during the real model simulation.

3.2.7 Joule Heating (Two-Phase Flow)

This case represents heat transfer in porous media with injecting water. Rock is saturated by the water and oil (S^0_w, S^0_o). On the left border electrical current supplied and water is injected. Used in this model parameters are listed in the table 3.8. Initial conditions are the initial temperature in the reservoir (T_0), zero potential of electric field (V_0=0 V), initial pressure (p_0), water saturation (S^0_w) and oil saturation (S^0_o) (Fig. 3.22). Boundary conditions are on the left border - fixed Electrical current (I) water injecting rate (u), on the right border – ground potential (V_0) and pressure (p_0). Electric and thermal insulations and no flow conditions are shown on the scheme.

Table 3.8. Joule Heating (two-phase flow) problem parameters

Name of parameter	Dimension	Definition
Initial temperature, T_0	°C	10
Porosity, ε_p	-	0,35
Density of rock, ρ_r	kg/m^3	2250
Thermal conductivity of rock, k_r	W/m/°C	2.63
Thermal capacity of rock, C_r	J/(kg·°C)	743
Length, L	m	300
Height, H	m	40
Thermal conductivity of water, k_w	W/m/°C	0.58
Thermal capacity of water, C_w	J/(kg·°C)	4180
Density of water, ρ_w	kg/m^3	1000
Density of oil, ρ_o	kg/m^3	1000
Thermal conductivity of oil, k_o	W/m/°C	0.17

Name of parameter	Dimension	Definition
Thermal capacity of oil, C_o	J/(kg·°C)	1700
Initial water saturation, S_w^0	-	0.2
Initial oil saturation, S_o^0	-	0.8
Electric current density, I	A/m²	1
Cementation exponent, m	-	1.37
Saturation exponent, n	-	2
Water electric conductivity, σ	S/m	1.421
Injection water velocity, u	m/s	$2.89 \cdot 10^{-7}$

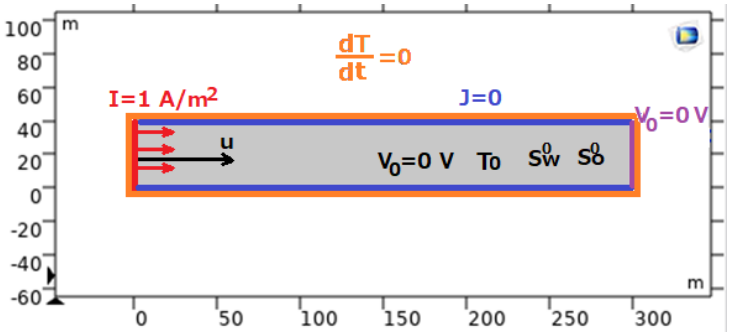

Figure 3.22. Electro-thermal heating model scheme

On the graphics below we can see the electric parameters like electric current density and potential (Fig. 3.23). Electric current value (a) due to boundary conditions should stay constant, but there are also some fluctuations on the graphic at the beginning. These changes occurred because of second phase (water) intrusion into the system. Electric potential graphic (b) we can see that the value of the potential on the right border is decreasing. Again, it is because of water intrusion into the system which changes system conductivity. Water raises electrical conductivity of porous media and as a result electric potential value decrease.

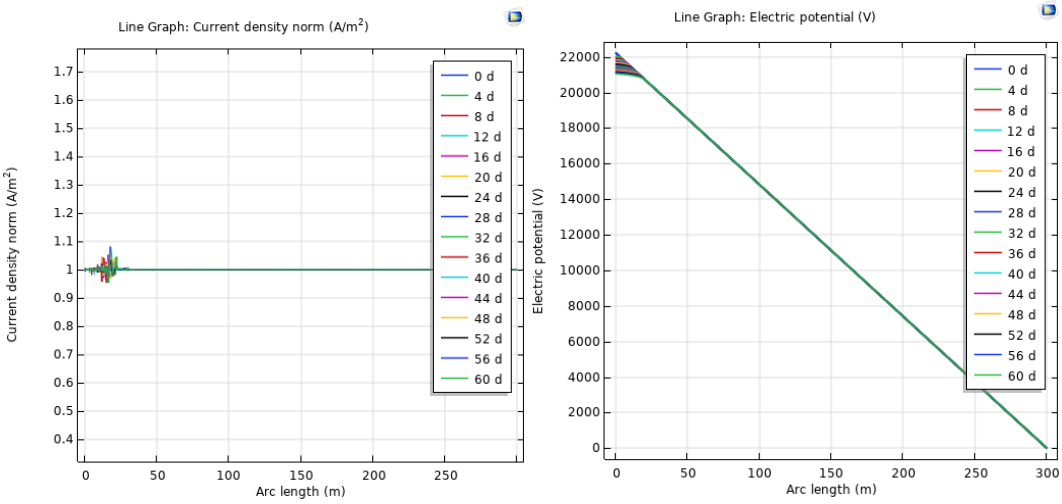

(a) (b)

Figure. 3.23. Electric current density (a) and electric potential (b) profiles

On the figure 3.24 we can see water fraction movement. The viscosity of oil changes with the temperature as it is shown on the graphic of interpolation in the section 3.2.5. As water heat up oil, oil viscosity drops, so the displacement process becomes more complete, which we can see on the volume

fraction graphic (Fig. 3.24 (a)) (we can compare it to the volume fraction of case 2 ($\mu o/\mu w$=10)). Looking at the electrical conduction graphic (Fig. 3.24 (b)) of the system, we can see that it is resembles volume fraction graphic. According to the Archie's Law which determine electrical conductivity of the porous medium, it is directly depends on amount of water in the system (because water is a conductor). So that is why the conductivity of the part of rock where water has infiltrated is bigger than in other area.

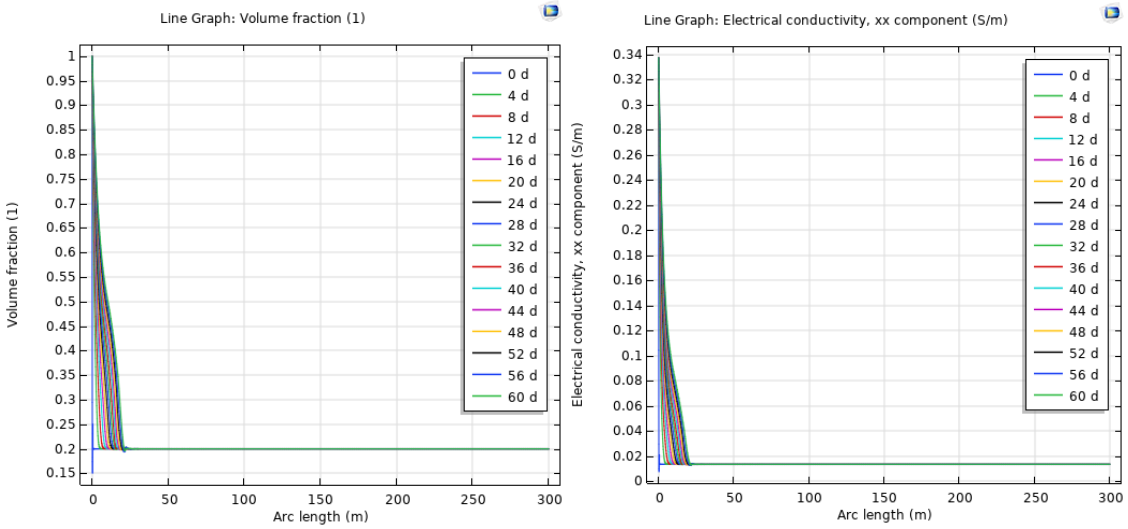

(a) (b)

Figure. 3.24. Water saturation (a) and electric conductivity (b) profiles

In Fig. 3.25 on the left border pressure value (a) drops because water infiltrate in the rock. Water amount changes saturation profile of the system which according to the Darcy's Law changes the pressure profile. Velocity value (b) should stay constant during filtration process as it is set in the boundary conditions, however fluctuations occurred which are caused by water intrusion.

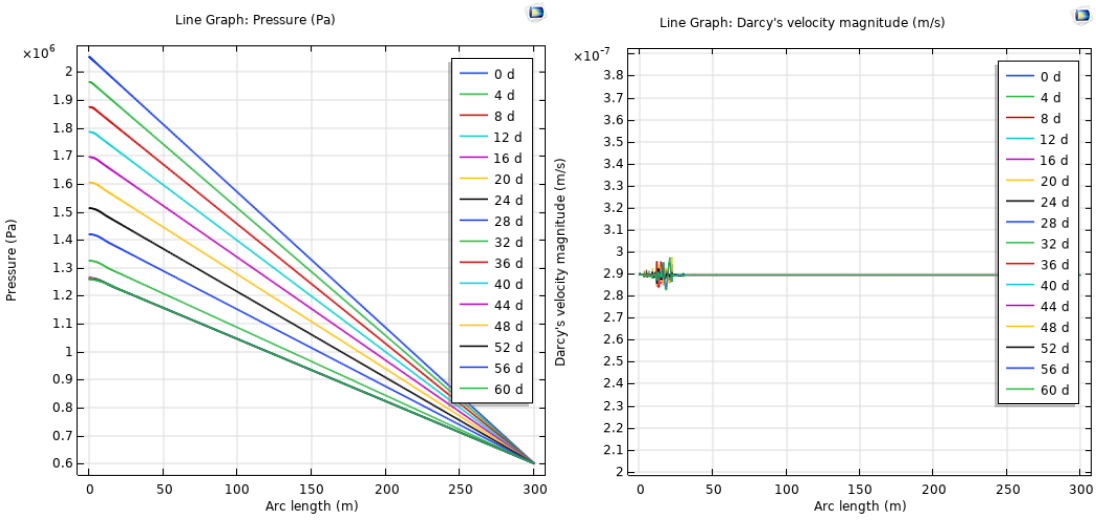

(a) (b)

Figure. 3.25. Pressure gradient (a) and water velocity (b) profiles

Finally, temperature profile is shown in the Fig. 3.26. There is definitely raising of the temperature value, which says that Joule Heating process works. The tendency of temperature change can be explained by water volume fraction and conductivity graphics. We can see that in the beginning at the left border, temperature value is close to the initial temperature and then significantly raising. This is because of water intrusion. Firstly, as it was described above, the more water inside the rock, the more conductivity of system and the less temperature change. Secondly, cold water is injected into the rock (initial temperature 10°C) which lead to cooling. Still water is needed to be injected as it removes heat from the electrode.

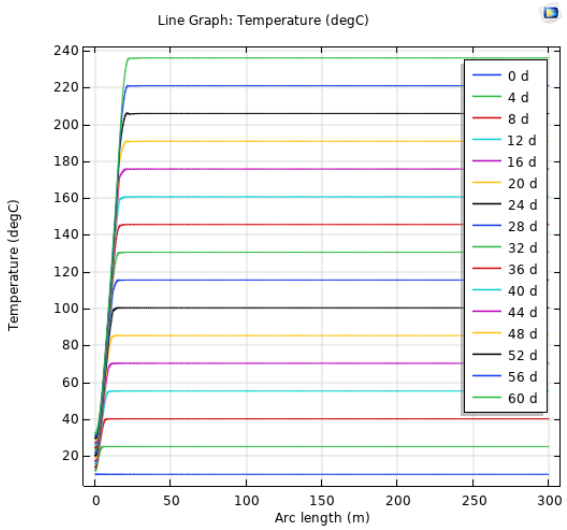

Figure. 3.26. Temperature profile

3.3. Evaluation of the Code

To prove the applicability of COMSOL as simulation tool, the experiment of M. Krol (Krol and Sleep, 2011) was reproduced in COMSOL, and results were compared between each other.

3.3.1 Krol's Experiment

In 2010 M. Krol described subsurface flow and transport at 50°C temperature during electrical resistance heating (ERH) for soil remediation. It is a multiphysical process which includes electrical current flow, temperature-dependent fluid flow, and mass transport. To examine these effects series of two-dimensional tank experiments were carried out. Tank 60 cm long, 45 cm tall, 1 cm thick was packed with 0.5mm glass beds representing sands (Fig. 3.27). Hydraulic conductivity of glass beds is 0.3 cm/s. Five injecting wells, and five production wells were set on opposite sides of tank. Injection rate is 5 cm^3/min. Two columns of electrodes were set in the tank, first column of six electrodes were set to 120 V, another column was attached to neutral. To measure the temperature of tank, 48 thermocouples were evenly set. To study buoyancy effect, tracers were also injected through the tracer injection wells. The experiment lasted 8 hours 45 minutes.

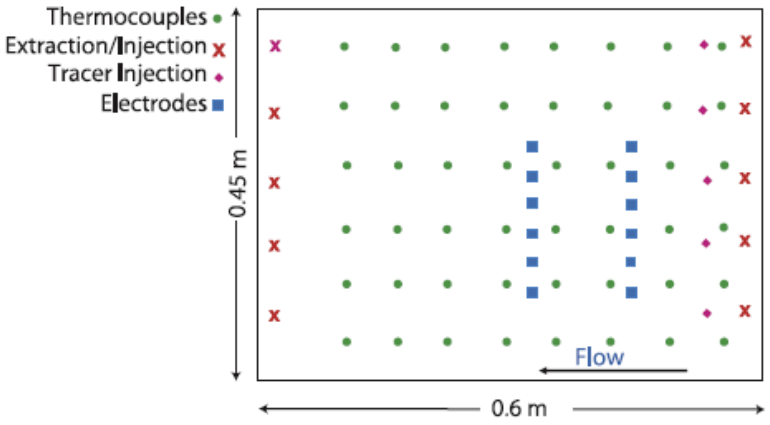

Figure 3.27. Tank experiment scheme

Numerical model was also built during this study. At the beginning of each step, the voltage distribution is calculated according to electric charge conservation law:

$$\nabla \cdot (\sigma \nabla V) = Q \tag{28}$$

where Q represents sinks and sources of electric charge, which are nonzero only at the electrodes.

Power dissipation U was calculated as follows:

$$U = \sigma|\nabla V|^2 \tag{29}$$

Boundary conditions for electric current flow was set to be insulated on the walls of model.

Water flow was solved by using equation for hydraulic head and Darcy's velocity:

$$\vec{q} = -\frac{kg\rho_f}{\mu}\left[\nabla h_f + \rho_r \nabla z\right] \tag{30}$$

where ρ_f is the freshwater density, ρ_r is the density coefficient $(\rho - \rho_f)/\rho_f$, ρ is the density of the fluid at the current temperature, k is the soil permeability, and μ is the water viscosity. In this case water density and viscosity dependance on temperature were accounted for.

Heat transfer process was described using equation (31) which is solved for temperature:

$$\frac{\partial}{\partial t}\left[\rho_w \varepsilon_p C_p T + (1-\varepsilon_p)\rho_r C_b T\right] + \rho_w C_p \nabla[\vec{q}T] - K_H \nabla^2 T - U = 0 \tag{31}$$

Where ρ_b is the bulk density of the soil, C_b is the heat capacity of the soil, C_p is the heat capacity of water, $\vec{q}$ is the Darcy velocity vector, and K_H is the bulk thermal conductivity.

Boundary conditions of heat transfer is heat insulation. Injection and production wells were simulated as source and sink.

3.3.2 Model's Set Up

Krol's tank experiment model was reproduced in COMSOL. The geometry is set to be identically same as in tanks experiment (Fig. 3.28).

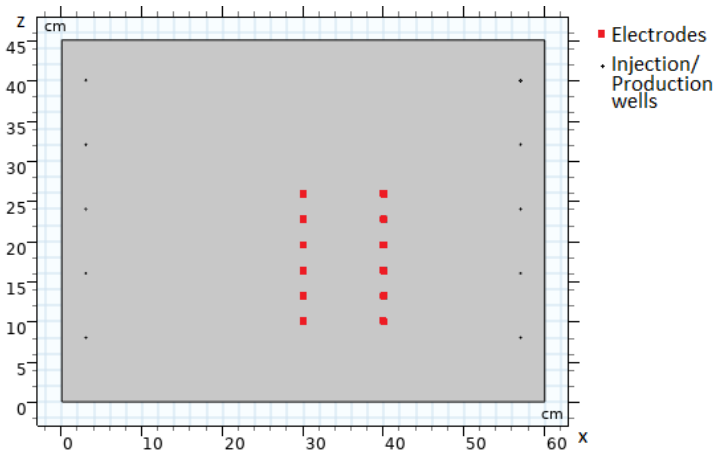

Figure 3.28. Tank experiment scheme in COMSOL

The modules that are used in COMSOL to describe ERH are Darcy's Law module for fluid flow, Heat Transfer in Porous Media for heat flow and Electric Currents module for electric currents flow. Automatically COMSOL sets coupled multiphysical interface Electromagnetic Heating which is consisted of Heat Transfer in Porous Media module and Electric Currents module.

Fluid flow represents single phase flow of water in porous media. Velocity of flow is determined by Darcy's Law (1) and mass conservation equation (19). Heat flux is described by energy conservation equation coupled with electric charge conservation equation (18):

$$\left(C_p\rho\right)_{eff}\frac{\partial T}{\partial t} + \rho_w C_w u \cdot \nabla T + \nabla \cdot q = Q_{j.v} \tag{32}$$

Where $\left(C_p\rho\right)_{eff}$ – specific heat of bulk (33), C_w – heat capacity of water, u – velocity of water, q – heat flux density described by Fourier's Law of Thermal Conductivity (5), $Q_{j.v}$ – total electric charge (14, 18).

Specific heat of bulk:

$$(\rho C_p)_{eff} = S_w \varepsilon_p \rho_w C_w + (1 - \varepsilon_p)\rho_r C_r \quad (33)$$

Where C_r, C_w, – heat capacity of rock and water, J/kg/K, ρ_r, ρ_w – density of rock and water, kg/m^3.

Effective conductivity of bulk:

$$K_{eff} = S_w \varepsilon_p K_w + (1 - \varepsilon_p) K_r \quad (34)$$

Where K_w and K_r – water and rock conductivity W/m·K.

Electric conductivity of the system in COMSOL is described differently from Krol's model. COMSOL uses Archie's Law equation (16) to determine the electric conductivity of dry bulk saturated with fluid. However, Krol's model include electric conductivity of wet fully saturated porous medium.

In table 3.9 parameters used in Krol's model and COMSOL's model are presented.

Table 3.9. Krol's experiment parameters

Parameters	Krol's data	Applied data
Water electrical conductivity, σ_w	0,12 S/m	0,12 S/m
Porosity, εp	0,4	0,4
Permeability, k	$4 \cdot 10^{-10}$ m^2	$4 \cdot 10^{-10}$ m^2
Anisotropy ratio, Kx/Kz	0,7	0,7
Electric potential, V	120 V	120 V
Injection rate, Qinj	5 cm^3/min	5 cm^3/min
Medium thermal conductivity, K_{Hb}	0,026 W/m·K	-
Dry bulk thermal conductivity, K_b	-	1,2 W/m·K
Dry bulk density, ρb	-	1370 m^3/kg
Dry bulk heat capacity, $C_{p,b}$	-	700.55 J/(kg·degC)

3.3.3 Results and Discussion

From Figs. 3.29 and 3.30 we can see results of Krol's experiment and numerical simulation and COMSOL simulation. All graphics show temperature distribution of the system of vertical cross section of tank. The shapes of temperature isolines is a result of buoyancy effect which occurs due to water density and viscosity dependance on temperature. Experiment results show greater increase of temperature than simulation models. COMSOL simulation result looks similar as Krol's simulation result. The shape of COMSOL's isolines resembles the shape of Krol's result, but there is small discrepancy of the lines in the tank bottom. COMSOL's result did not represent perfectly Krol's experiment results as some data is missing in the paper. Still COMSOL's results are pretty close to Krol's which means that COMSOL is capable enough as numerical tool to investigate the electro-thermal heating effect on oil sands production.

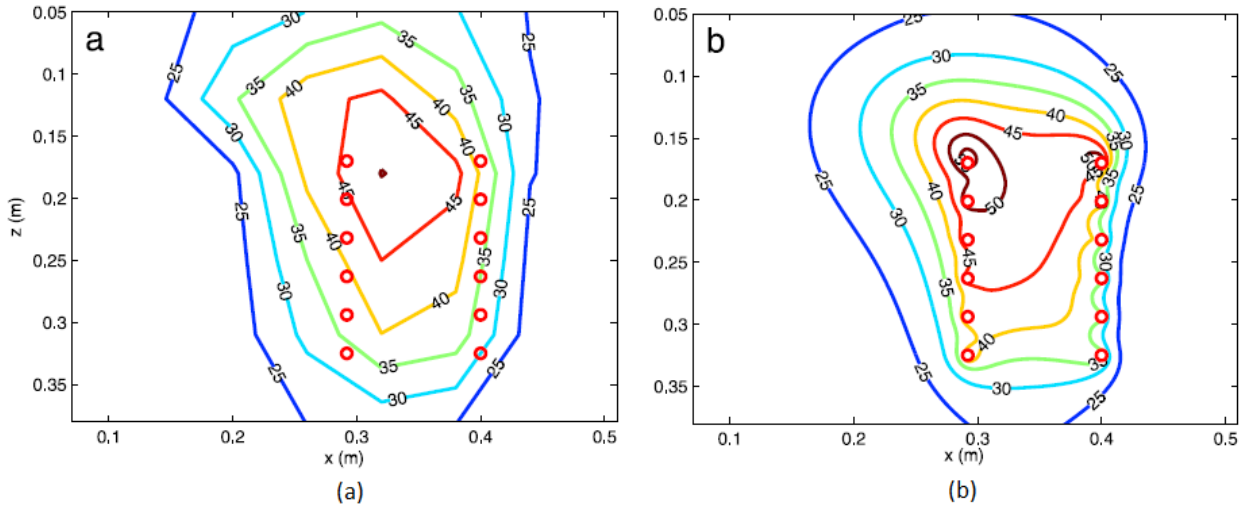

Figure 3.29. Krol's experiment results: (a) experiment (b) laboratory model (Krol and Sleep, 2010)

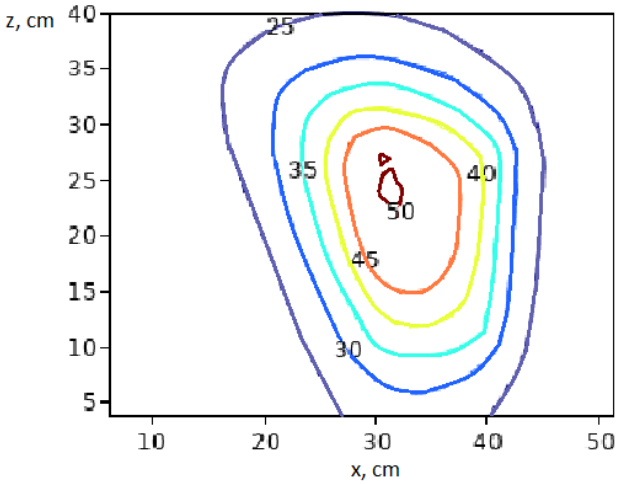

Figure 3.30. COMSOL's numerical model result

Chapter 4

Description of Hangingstone Oil Sands Field

4.1. Overview

The Hangingstone oil sands field is located in 20 km southwest of Fort MucMurray, northeastern Alberta, Canada (Fig. 4.1). The development history of Hangingstone oil sands field started in 1978 when Japan Canada Oil Sands Limited (JACOS) was established. JACOS started pilot tests on Hangingstone oil sands field, including CSS and electric heating methods. In 1997, SAGD demonstration started on the area. The test production with SAGD method started on June 1999. In May 2008, environmental impact assessment was started, and it was completed in March 2010. In 2012, construction of wells was started (AER Hangingstone Project Update, 2020). First steam was produced in March 2015 and first oil in July 2015 (JAPEX, 2012).

Figure 4.1. Regional map (Einstein, 2006)

Bitumen production rate by SAGD was estimated to be 1.908 m^3/day (Hangingstone Expansion, Athabaska Oil Corporation, 2017). Project area is to be 5.6 km^2 while developed area is 5.1 km^2 (Fig. 4.2). The area is divided into five production pads, 25 horizontal well pairs (five well pairs per pad), i.e., totally 50 horizontal wells (Fig. 4.3). Average horizontal length of the wells is 700 m. Wells of each pad are located about 100 m apart, distance between pads is 130 m. There are 25 observation wells in total, in which 10 wells are vertical delineation wells, 15 wells with thermocouples to control temperature, and 6 piezometers. Wells are equipped with pressure sensors, however, some of these were broken because of the high pressure steam conditions.

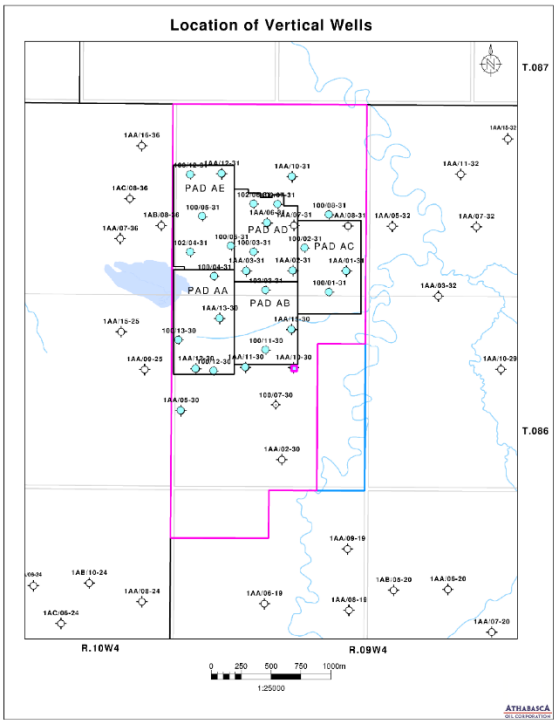

Figure 4.2. Project area map of the Hangingstone oil sands field (Hangingstone project update, 2020)

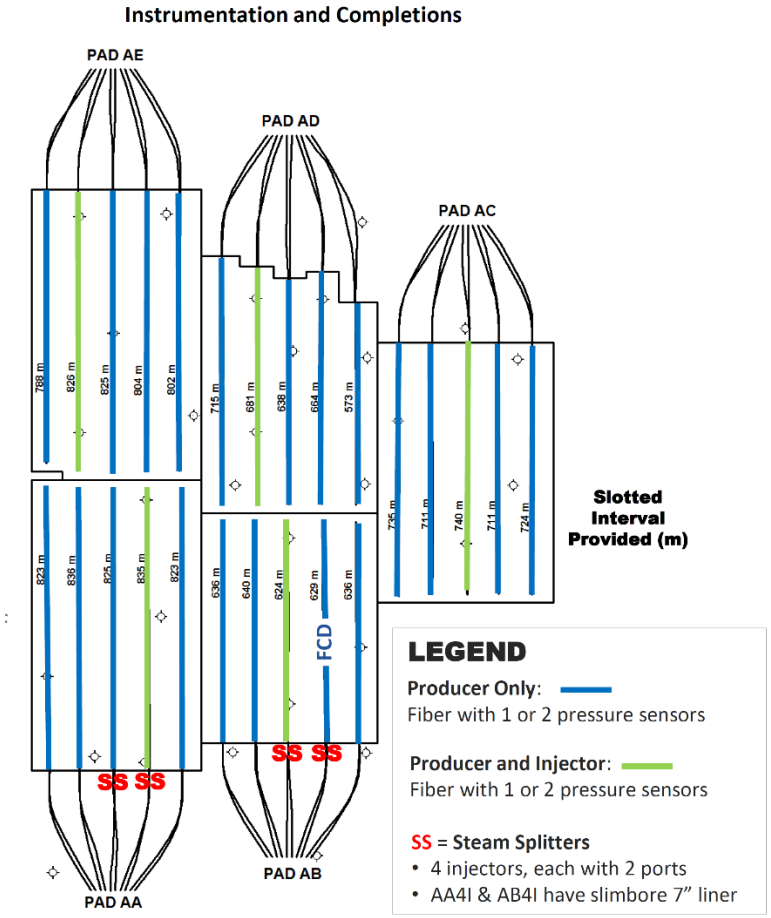

Figure 4.3. Production pads (Hangingstone project update, 2020)

4.2. Geology and Stratigraphy

Geophysical well logging surveys were conducted to evaluate reservoir quality, including lateral and vertical reservoir homogeneity. These were gamma ray, induction (shallow, medium and deep), spontaneous potential, bulk density (and photoelectric), neutron porosity, caliper and sonic surveys (Hangingstone Expansion, Athabaska Oil Corporation, 2017). Cores were obtained to provide detailed information on the stratigraphy, determine the environments of deposition, and to establish reservoir details. Core analyses were conducted to evaluate porosity, bitumen saturation and grain density, as well as vertical and horizontal permeability from bitumen saturation formation. Obtained properties of the reservoir help to estimate potential gross pay.

The stratigraphic intervals are shown in Fig. 4.4. Here, McMurray formation is the one having bitumen in pore space.

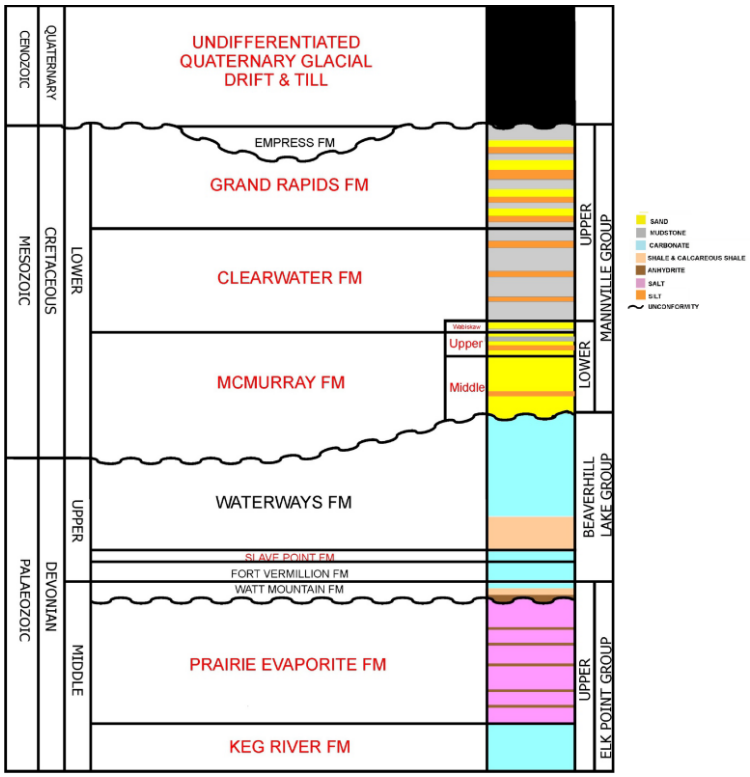

Figure 4.4. Stratigraphic section (AER Hangingstone Project Update, 2020)

The Keg River Formation was deposited in Devonian, and it consists of grey and brown dolomite with poor intercrystalline or vuggy porosity, and, brown, cryptocrystalline, limestone, and minor dolomite. The Prairie Evaporite Formation was also deposited in Devonian, and it consists of an interbedded halite, sylvite, anhydrite, red beds and minor anhydritic dolostone.

Bitumen saturated formation is called McMurray Formation and it is divided into middle and upper members. Its age is Cretaceous. The lithology of the Middle McMurray member typically comprises fine grained, high angle cross bedded channel sandstone that grade upward into heterolithic sandstone and mudstone forming point bars and associated abandoned channel and muddy tidal flats. Observed within the channel sandstone are numerous occurrences of mudclast breccia beds. The Upper McMurray erosionally overlies the Middle McMurray member and it consists of fine-grained interbedded sandstone with light to dark grey mudstone.

The McMurray Formation is unconformably overlain by interbedded argillaceous siltstone, mudstone and thin sandstone of the Clearwater Formation. The Clearwater Formation was deposited in Early Cretaceous. It is a sandy, muddy and glauconite-rich formation.

The Grand Rapids Formation is also Early Cretaceous formation, and it overlies the Clearwater Formation and is unconformably overlain by Quaternary sand, gravel and mud sediments. The Grand

Rapids Formation is composed of cleaning-upward packages that are separated by muddy and silty beds and is present throughout the area.

The Quaternary sediments form a complex paleotopography composed of a series of pre-glacial and glacial channels incised into the sediments below. The Quaternary sediments are typically composed of gravel, sand and clay.

4.3. Bitumen Recovery

Performance of bitumen production from each pad depends on different factors such as geology, pad boundary, well pair trajectories and pump performance. Results of each pad performance during period 2015-2019 are presented in Table 4.1 (AER Hangingstone Project Update, 2020). Average net pay is a thickness of bitumen saturation formation, original bitumen in place (OBIP) is an estimated amount of bitumen that lays in reservoir, current recovered is an amount of bitumen extracted by the October 2019. According to Table 4.1. recovery factor of each pad varies from 8.5% to 23.5%. The most productive pad is AB pad which recovered 0.68×10^6 m^3 of bitumen and the recovery factor is 23.5%. The lowest production amount was at AC pad. Totally, during the four years of exploitation, five pads produced $1.99 \cdot 10^6$ m^3, out of 15.6×10^6 m^3, and the recovery factor is 12.8%. It is also predicted that final recovery factor will reach 70%.

Table 4.1. Pads recovery (AER Hangingstone Project Update, 2020)

Pad	Well Pairs	Average Lateral Length (m)	Average Net Pay (m)	Oil Saturation (frac)	Total Net Pay Porosity (frac)	OBIP (10^6 m^3)	Current Recovered[1] (10^6 m^3)	Current Recovery Factor (%)	Predicted Recovery Factor (%)
AA	4/5	850	28.0	0.71	0.35	3.3	0.31	9.4	50-70
AB	5/5	640	29.3	0.73	0.37	2.9	0.68	23.5	50-70
AC	5/5	750	28.7	0.70	0.36	3.0	0.25	8.5	50-70
AD	5/5	670	32.1	0.71	0.35	3.2	0.35	11.0	50-70
AE	5/5	830	28.2	0.70	0.35	3.2	0.39	12.3	50-70
TOTAL	24/25					15.6	1.99	12.8	50-70

Cumulative amount of bitumen production was shown in Fig. 4.5. After approximately 400 days of SAGD exploitation, production was increased, especially for AB pad.

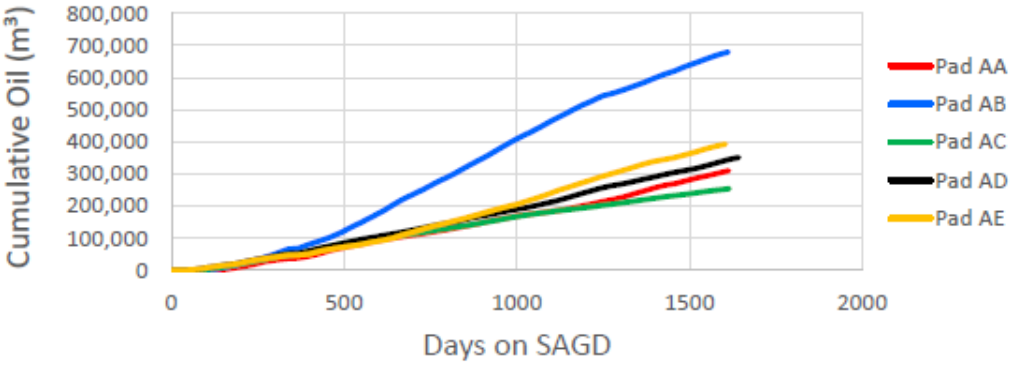

Figure 4.5. Cumulative oil production from the Hangingstone oil sands field (AER Hangingstone Project Update, 2020)

Chapter 5

Application of Geological Model

5.1. 2-D Model Design

A simplified 2-D model for ETHM based on the information obtained from the Hangingstone oil sands field was developed and simulation was conducted by applying COMSOL Multiphysics.

5.1.1 Geology and Geometry of the Model

Based on the stratigraphical section of Hangingstone oil sands field (AER Hangingstone Project Update, 2020), a simplified geological model was built in COMSOL (Fig. 5.1). 2-D model consists of three layers, i.e., mudstone with 155 m thickness, sands with 28 m thickness, and limestone with 150 m thickness. Total thickness of the model was 333 m and width was 70 m. The width was set based on the previous field experiments (McGee and McDonald, 2008) and preliminary simulation results (Chapter 3).

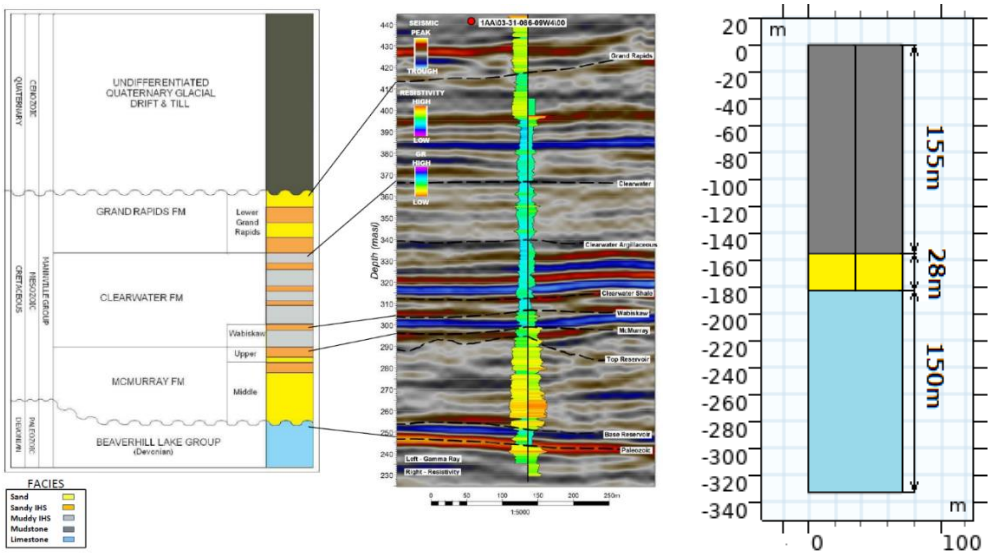

(a) (b)

Figure 5.1. Stratigraphic section of Hangingstone oil sands (a) field data (AER Hangingstone Project Update, 2020) (b) COMSOL model

Injection wells were set as two blocks on the sides, and production well one block in the mudstone and sands formations (Fig. 5.2). Diameter of each well was 0.2 m and the length was 183 m. The distance between each well was 35 m.

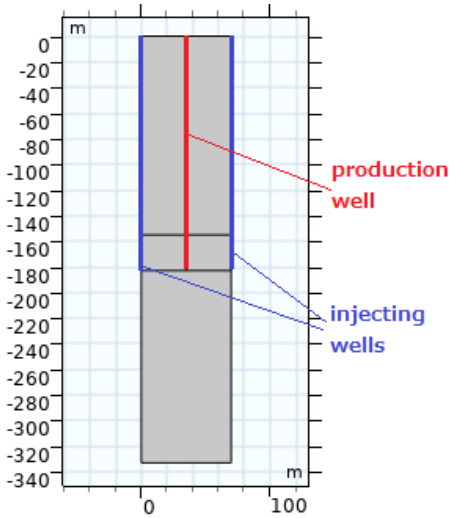

Figure 5.2. Location of injection and production wells

5.1.2 Mesh

As shown in Figure 5.3 (a), the 2-D model domains were discretized differently. Mudstone and limestone formations ware discretized into 2364 triangle elements while sand formation and wells were discretized into 5360 rectangles. Total number of elements was 7724, and edge elements 826. Local refinement was applied at sand formation and nearby wells (Fig. 5.3 (a), (b)) because the two-phase fluid flow occurs mainly in these areas, and the simulation requires higher stability and accuracy. Also, refinement was applied to the boundaries between the formations (Fig. 5.3 (b)). The element size was in the range of 0.099 to 22.3 m.

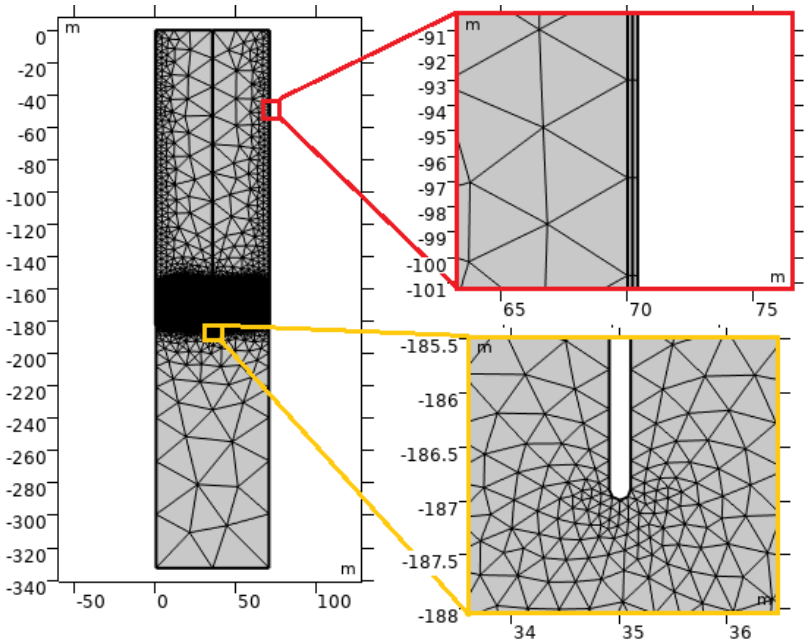

(a)

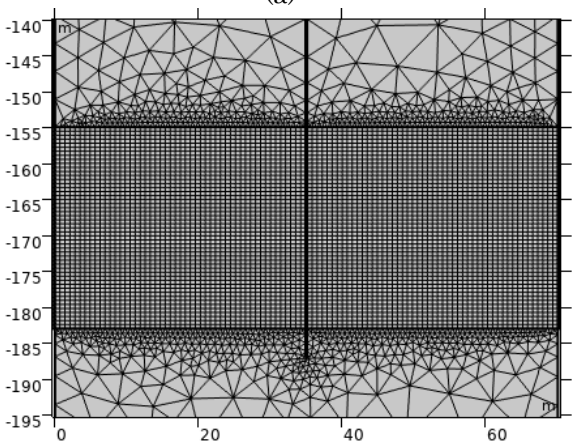

(b)

Figure 5.3. Mesh structure (a) side boundary and production well edge (b) sand formation

5.1.3 Boundary and Initial Conditions

Based on preliminary 2-D simulations, boundary conditions (BCs) and initial conditions (ICs) were set for each module. To reproduce natural reservoir conditions, hydrostatic pressure was set as initial pressure condition (Fig. 5.4 (a)), as well as temperature gradient which is 0.021 K/m for Athabaska area (Fig. 5.4 (b)). Water saturation profile was shown on Fig. 5.4 (c). Mudstone and limestone formations were fully saturated with water while oil sands water saturation was 0.28. Initial water saturation of oil sands was based on field data (AER Hangingstone Project Update, 2020). Initial water saturation inside wells was set to be one. For electrical current flow module, ground condition (0 V) was set as initial condition for whole model.

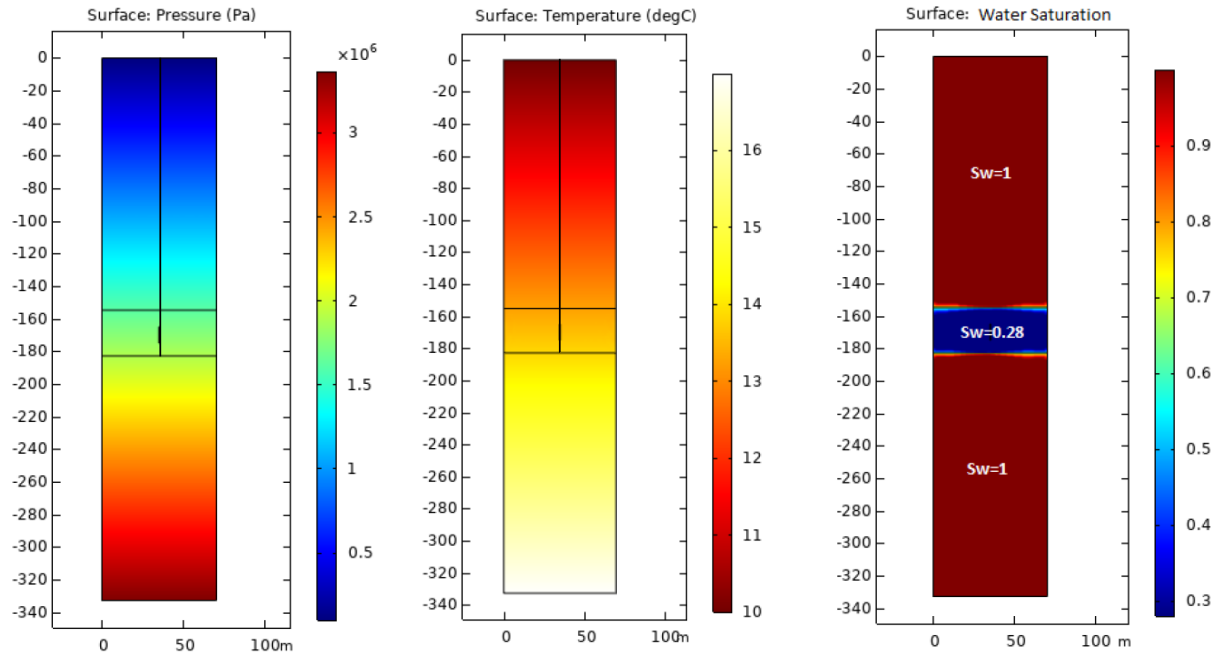

(a) (b) (c)

Figure 5.4. Initial conditions (a) pressure, (b) temperature, (c) water saturation

Boundary conditions were set according to the previous simulation results. Fixed temperatures were set on the top and bottom of the model (Fig. 5.5 (a)). Surface temperature was set to be year average temperature at Athabaska region which is 10°C. Bottom temperature is set to be 17°C which is equal to the temperature at 333 m depth according to temperature gradient. Outflow condition is set on production well at the interval of sands formation. On the side of production well thermal insulation BC was set. Symmetry condition was set on the side walls of the model. Electrodes were located inside the injection wells at the sands formation and conducted constant electric current (Fig. 5.5 (b)). Ground condition was set on the walls of production well, top and bottom boundaries of the model. Electric insulation condition was set on side walls of the model. Inlet fluid velocity value was set at the surface of the injection wells.

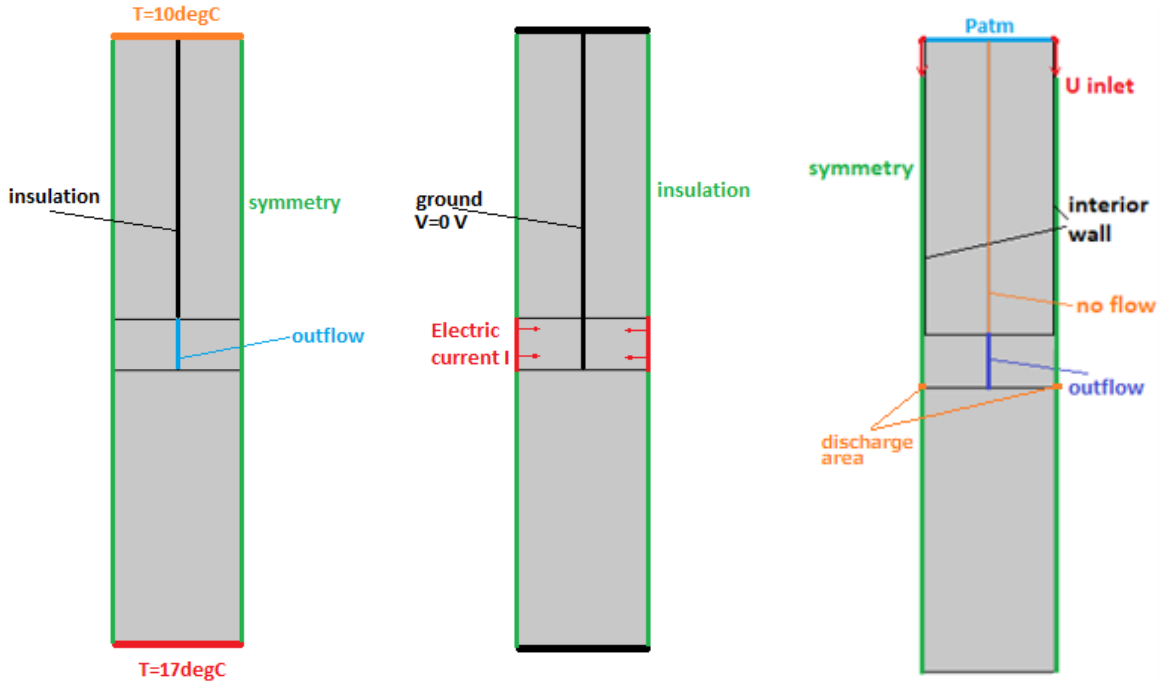

(a) (b) (c)

Figure 5.5. Boundary conditions (a) temperature, (b) electric current, (c) pressure

Atmospheric pressure was set to be constant on the top of the model (Fig. 5.5 (c)). Outflow condition was set to be changed with time. i.e.: during cooling process outlet condition was set on discharge area (Fig. 5.5 (c)), during displacement process outflow condition was set on the production well along the sand formation (Fig. 5.5 (c)). The rest part of production well up to the surface was set to be no flow condition. Side boundaries of model were symmetry BCs. Interior wall was set in between injection wells and mudstone to avoid water flow between the well and mudstone.

5.1.4 Parameters

Model parameters are summarized in Table 5.1.

In this model, water and bitumen viscosities were considered to be temperature dependent. As was mentioned in section 3.2.5, bitumen viscosity is highly dependent on temperature. According to the experiment data (JAPEX, 2012), bitumen viscosity decreases by 10^4 times. The dependence of bitumen viscosity and water viscosity on temperature were shown on Fig. 5.6, based on analysis of previous works (JAPEX, 2012), (Likhachev, 2003).

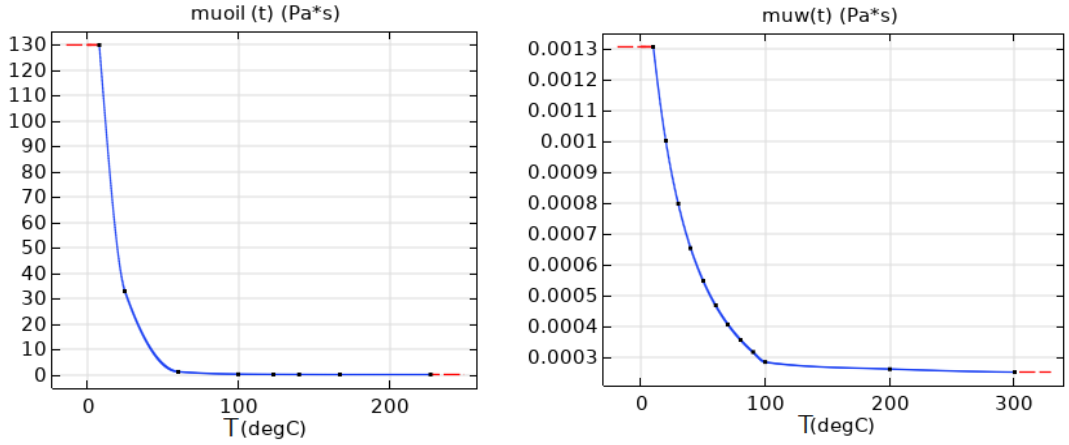

(a) (b)

Figure 5.6. Bitumen (a) and water (b) viscosity dependance on temperature

Table 5.1. Model parameters (Hangingstone Expansion, Athabaska Oil Corporation, 2017), (AER Hangingstone Project Update, 2020)

Module / Domain	Darcy's Law	Phase transport	Heat transfer	Electric current
Mudstone	Porosity ε_p=0,3 k = 1e-18 m2	Sw=1	Thermal conductivity rock k_r=3[W/(m*K)] Heat capacity rock C_r =1700[J/(kg*K)] Rock density ρ_r = 2000 kg/m^3	Electrical conductivity σ = 0,033 S/m
Sands	Porosity ε_p=0,35 kh = 3,9e-12 m2 kv = 3,2e-12 m2	Sw=0,28 So=0,72	Thermal conductivity rock k_r=2.63[W/(m*degC)] Heat capacity rock C_r =875.56[J/(kg*degC)] Rock density ρ_r = 2250 kg/m^3	Archie's Law: Saturation exponent n = 2 Cementation exponent m = 1,37
Limestone	Porosity ε_p=0,2 k = 1e-15 m2	Sw=1	Thermal conductivity rock k_r= 2,5 [W/(m*K)] Heat capacity rock C_r =1700[J/(kg*K)] Rock density ρ_r = 2000 kg/m^3	Electrical conductivity σ = 0,014 S/m
Wells	Porosity ε_p=0,99 k = 1e-8 m2	Sw=1	Thermal conductivity k_r =3 [W/(m*degC)]	In=5 A/m2
Water	Injection velocity u=1·10^{-3} m/s		Thermal conductivity water k_w =0.17[W/(m*degC)] Heat capacity water C_w =1700[J/(kg*degC)] Water density ρ_r = 1000 kg/m^3	Electrical conductivity σ = 1,421 S/m

5.2. Results

Total calculation time was 35 days. First 15 days were electro-thermal heating without fluid injection into the sand formation. Water was injected into the wells but was discharged to cool down electrodes. From 15th day, water was injected into the formation and bitumen production started. Figure 5.7 showed the representative cross sections. i.e., section 1-1 was a horizontal section along the sand formation, and section 2-2 was vertical section along the whole model.

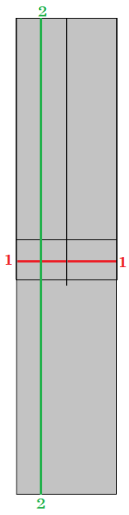

Figure 5.7. Model sections

Due to Joule Heating, temperature of the system increased unevenly. Temperature increase mainly occurred nearby the current electrodes and the lower part of production well (Fig. 5.8 (a)-(c)). After 15 days, temperature at the production well reached around 100°C while nearby electrodes it reached 220°C (Fig. 5.8 (d)). Temperature on the electrodes did not exceed 40°C. As water injection started to the sand formation, temperature profile approached to the plateau, and the temperature difference between nearby the injection wells and production well became around 30°C. Vertical section of temperature distribution showed that heat accumulation mainly occurred at sand formation (Fig. 5.8 (e)). Also, temperature raised up to 70°C in the mudstone and limestone formations near the sand formation.

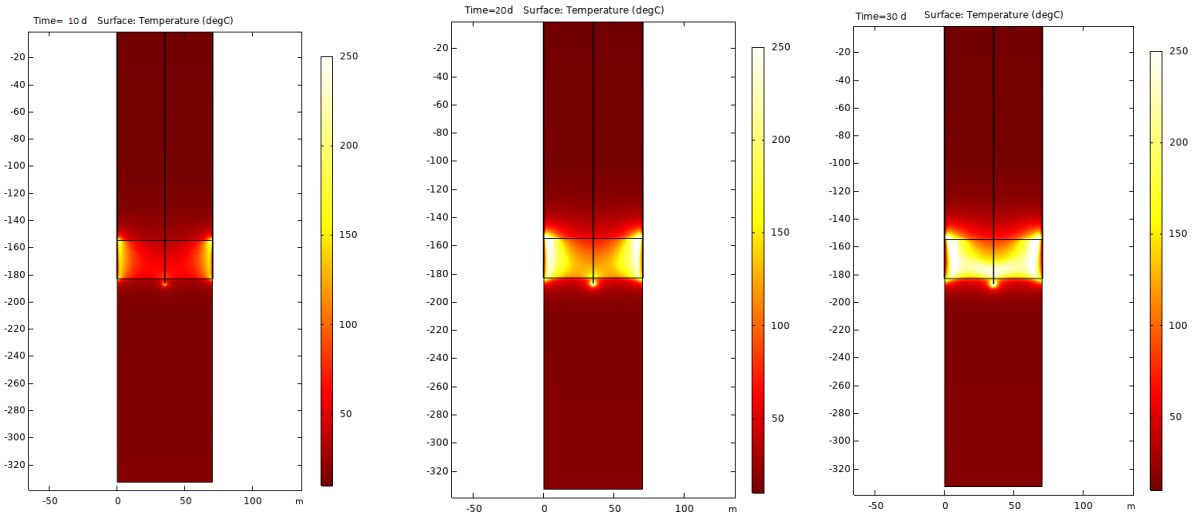

(a) t=10 d (b) t=20 d (c) t=30 d

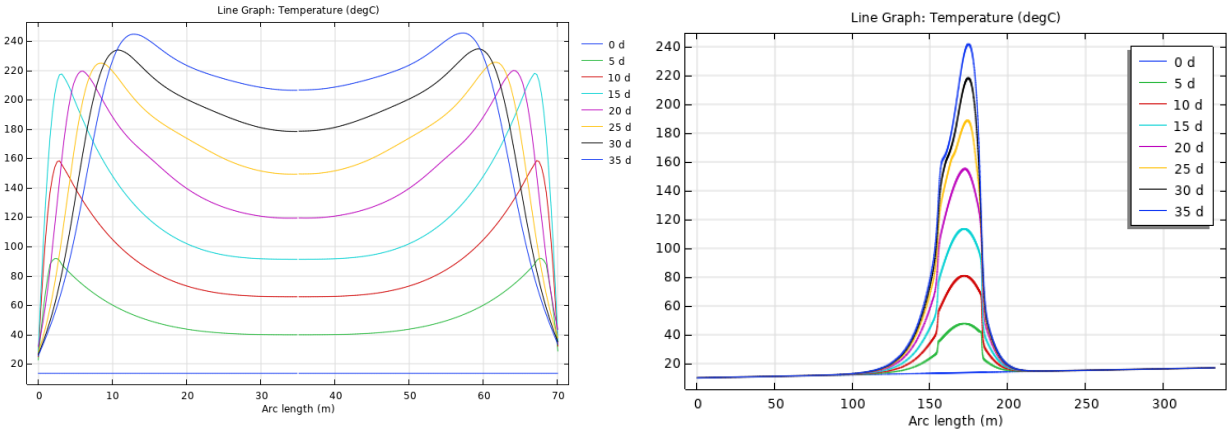

(d) Horizontal section 1-1 (e) Vertical section 2-2

Figure 5.8. Temperature distribution

Water saturation profiles were shown in Fig. 5.9. On the horizontal section 1-1 (a), we can see the displacement process occurring in sand formation. As water injection into sand formation started, the water-bitumen front moved towards the production well. Residual water saturation was set to be 0.2, which indicated that 20% of water cannot be extracted from the formation, therefore, water saturation profile did not become smaller than 0.2. The curved pattern of water saturation (Fig. 5.9 (a)) could be explained by different viscosities of fluids. Vertical section 2-2 (Fig. 5.9 (b)) showed no water saturation in mudstone formation while small increase of water saturation in the limestone formation was observed. Water saturation of the whole system was shown on Fig. 5.9 (c). Flooding pattern was uneven in sand formation, and water tended to move to the lower domain of the sand formation.

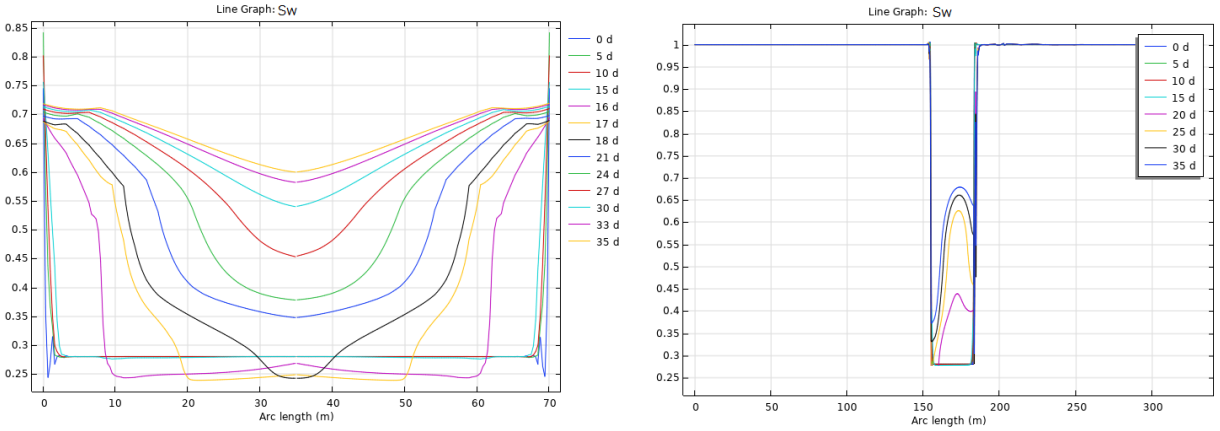

(a) horizontal section 1-1 (b) vertical section 2-2

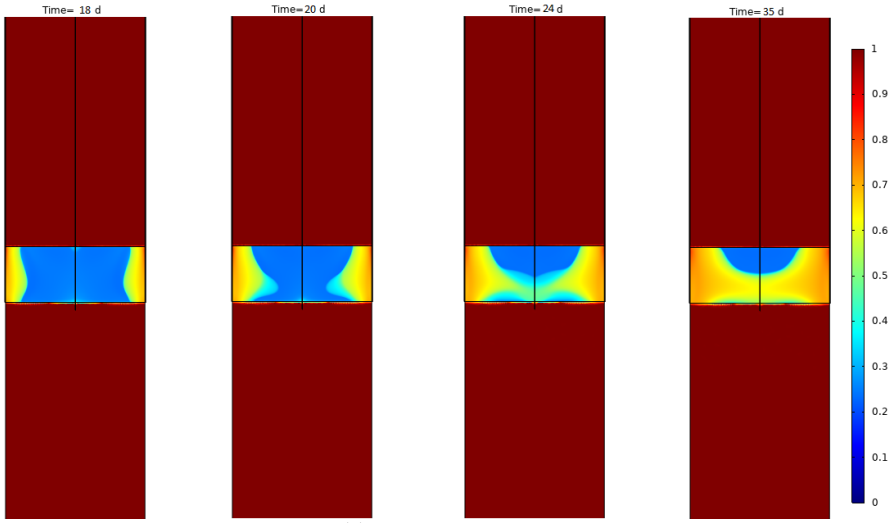

(c) surface map

Figure 5.9. Water saturation

Pressure profile of sands formation was shown in Fig. 5.10 (a). During cooling process pressure in whole formation was constant which corresponded to hydrostatic pressure at 170 m. After water injection was started, pressure increased at round 2.5 times. Then, pressure decreased with time. On the vertical section (Fig. 5.10 (b)), at the beginning of water injection pressure increased in the mudstone and limestone formations, however, greater increase can be seen in sand formation. As water was injected further to the formation, pressure in the system decreases.

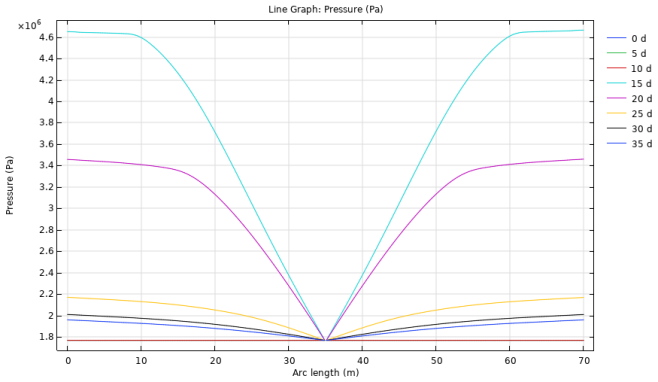

(a) horizontal section 1-1

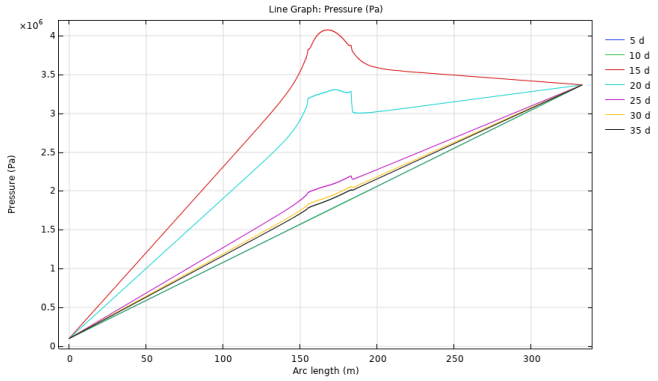

(b) vertical section 2-2

Figure 5.10. Pressure profile

Darcy's velocity field was shown in Fig. 5.11. Color range showed the amplitude of velocity value for X-direction and streamlines showed the direction of flow. Maximum velocity value reached at the sand formation at the bottom of production well. Velocity was very close to zero in mudstone and limestone formations The whole interval of sand formation was involved into fluid injection. Streamlines pattern showed horizontal flow towards production well.

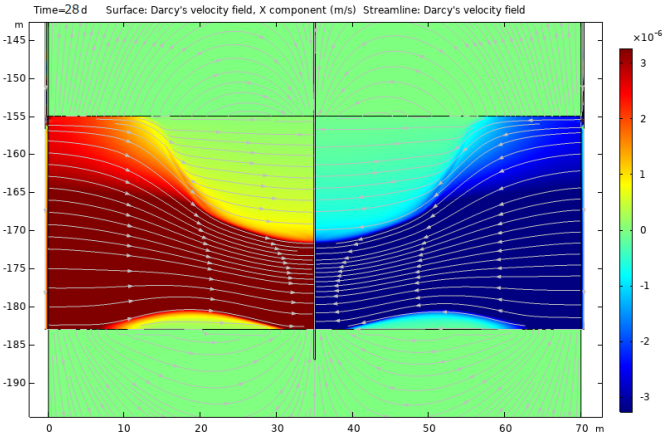

Figure 5.11. Darcy's velocity field (X-component)

Water and bitumen recovery rate at the production well were presented in Fig. 5.13. After water injection started on 15th day, oil velocity increased rapidly. In one day, value changed from zero to 1.95×10^{-4} m^3/s and then decreased (Fig. 5.12). Next increase happened on 34th day and then oil production rate started to continuously decreasing. Water recovery rate profile showed increase on 16th day and then decreased (Fig. 5.12). From 35th day when bitumen recovery rate started decreasing water recovery rate rapidly increased. This pattern is typical for oil production. Analysis of production rate of each day showed that average bitumen recovery factor was 73%.

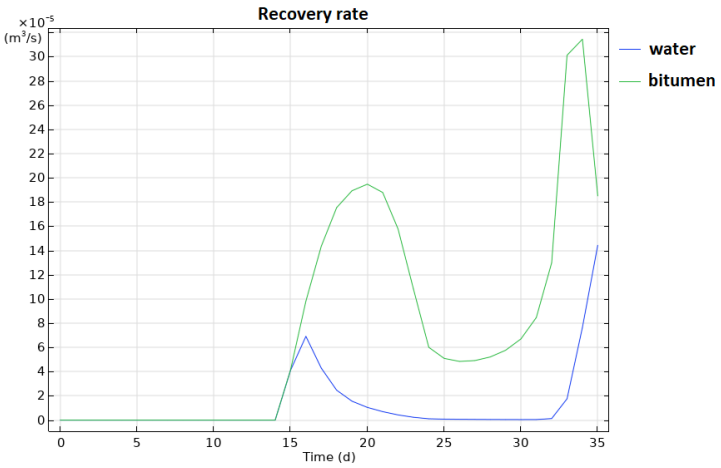

Figure 5.12. Recovery rate

Electric current density mainly increased at the sand formation, especially along the electrodes (Fig. 5.13 (a)). Streamlines showed the predominant horizontal direction of electric current to the ground potential electrode (Fig. 5.13 (b)). Lines were sub-parallel to each other except lower part of production well. It was due to the model geometry at the edge of the electrode, creating electric field convergence.

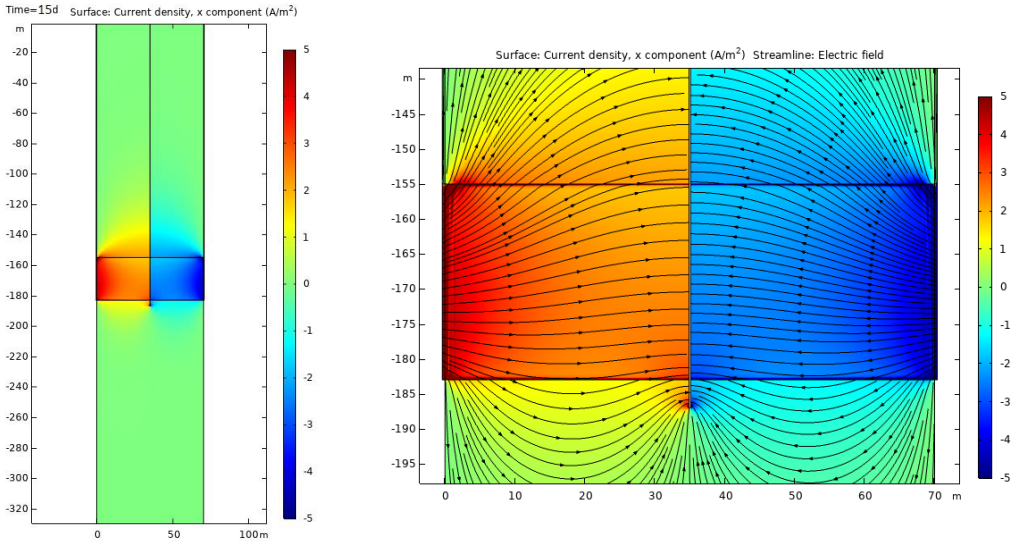

(a) Electric current density, X component

(b) Electric field streamlines

Figure 5.13. Electric field

Chapter 6

Discussion

There are many different factors which impact heat transfer performance. In this chapter, these factors and its configurations are discussed.

6.1. Fluid Viscosity and Temperature

It should be noticed that as bitumen changes its viscosity with temperature increase, water viscosity also changes. For realistic comprehension, it was proposed to consider water viscosity change along with bitumen viscosity change.

Previous simulations (Appendix) showed unsatisfied results with respect to water saturation profile (Fig. A.3 (b)). It was considered that maximum heating temperature should not exceed 100°C, which is boiling point of water. However, under 100°C, bitumen viscosity value was still greater than water viscosity. It is also well known, that with pressure increase the boiling point of water also increases. At the sands formation with its depth 155 – 183 m, the water pressure is 1.62 – 1.89 MPa and water boiling temperature under these conditions can be calculated by formula (Zhang and Evans, 2011):

$$T_{boil} = 179.47P^{0.2391} \tag{35}$$

Where P is pressure in MPa.

According to the formula (35), boiling point of water at 180 m depth is around 200°C. As a result of this analysis, temperature of the system can be increased up to 200°C without boiling. This change helped to improve the displacement process by decreasing bitumen viscosity.

6.2. Geometry

The temperature distribution was strongly affected by the size and spacing of electrodes. Different configurations studied were showed in Fig. 6.1. In the first case (a), electrodes were located between each other in 100 m, and length was 28 m, which is equal to sands formation thickness. Second case was that the length of electrodes was shorten to 10 m according to article (McGee and Donaldson, 2009). Comparing to these in the final one, lengths of wells were prolonged up to the surface (Fig. 6.1. (c)). This modification represented real technical configuration and decreased the electric field convergence on edges.

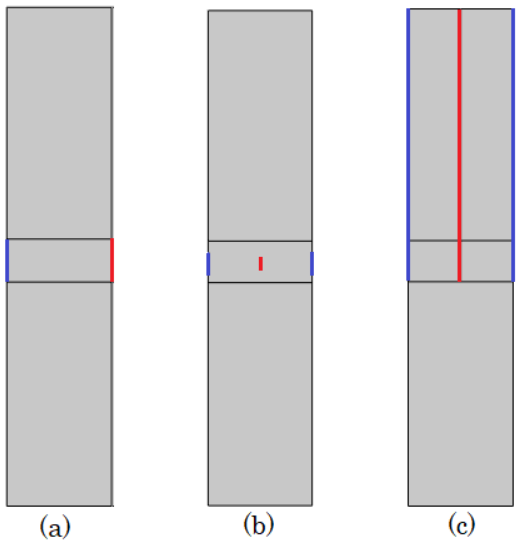

Figure 6.1. Electrode configurations, blue line – well used for current electrode, red line – well used for grounded electrode, (a), (b) – previous cases, (c) – current case

The large temperature was observed on electrodes, especially at the edges (Fig. 6.2 (a), (b)). This phenomenon was due to the electric field convergence (Fig. 6.3). It can be clearly seen in case (b) that the concentration of electric current density is big at the edges of electrode (Fig. 6.3 (a)).

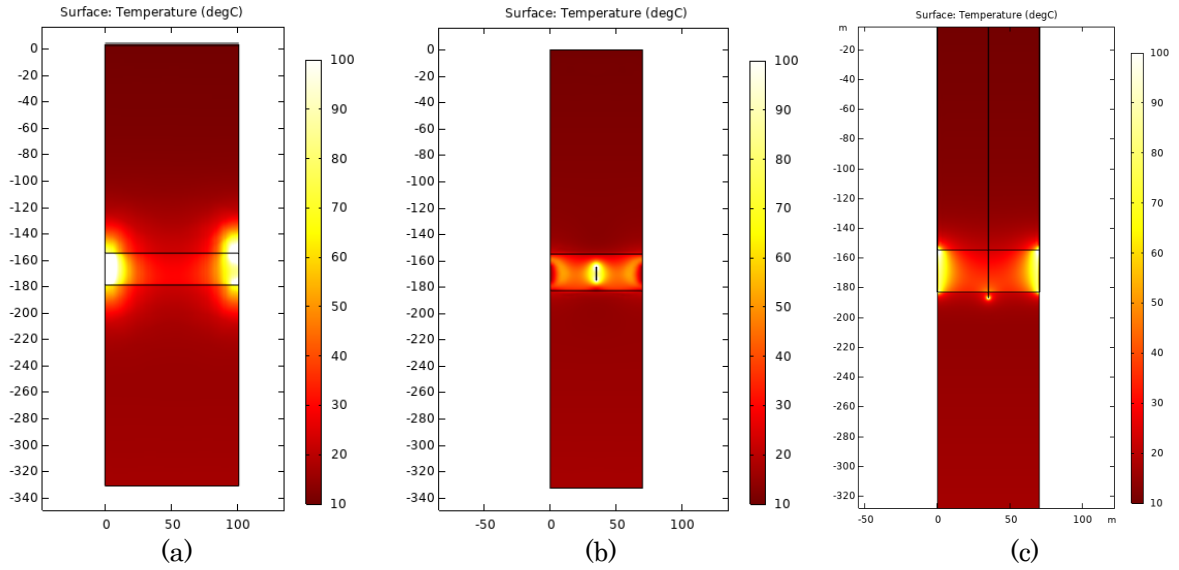

Figure 6.2. Temperature distribution

Electric streamlines were highly concentrated at the edges (Fig. 6.3 (b)) which led to abnormal temperature increase. This phenomenon highly affected the displacement process of bitumen as bitumen viscosity drops with the temperature increase which led to the uneven two-phase flow pattern. To reduce this effect, the geometry of wells should be modified.

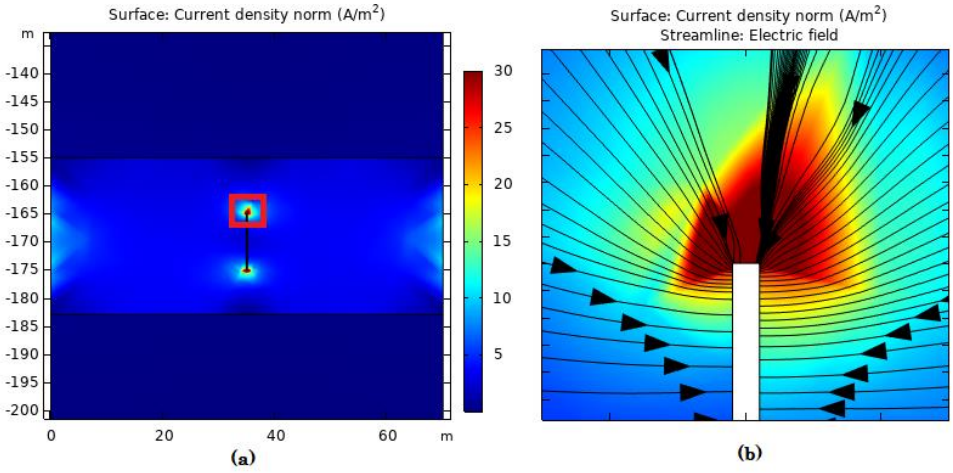

Figure 6.3. Current density (a) sand formation case b (b) squared shape

One of the modifications which should be implemented first is to round the edges. On Fig. 6.4, there is a scheme of shape change in current model (a) compared with the previous model (b). Rounded edges did not guarantee complete disappearance of electric field convergence but can reduce the effect (Fig. 6.3 (b) and Fig. 6.5).

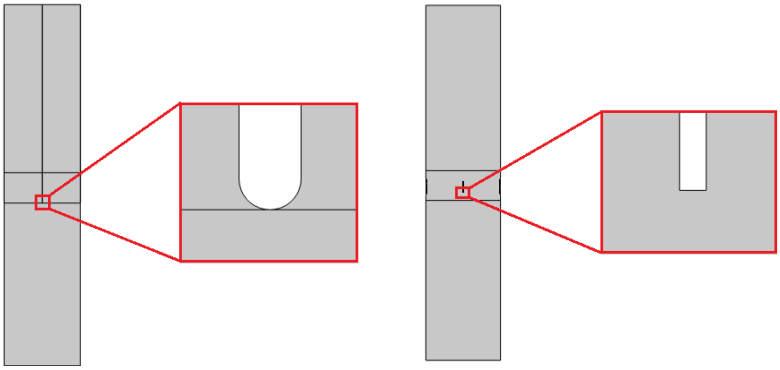

(a) (b)

Figure 6.4. Well edge configuration (a) current model, (b) previous model

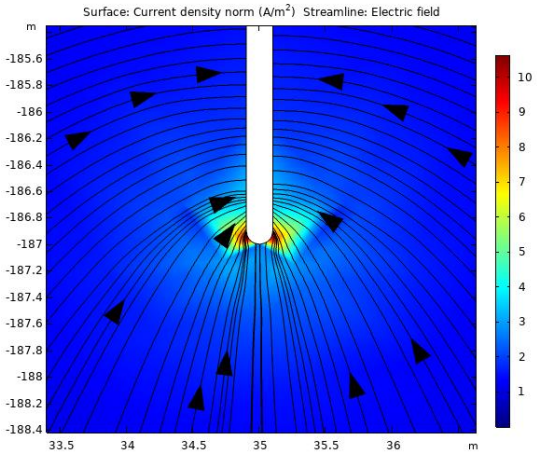

Figure 6.5. Electric field streamlines of rounded shape edge

Another modification that was implemented to decrease abnormal temperature increase at the edge was to prolong the length of production well beyond sands formation (Fig. 6.6). In the final model (a), production well length was prolonged to 4 m deeper into the limestone formation, while in case (b), bottom of the production well was co-located at the bottom of sand formation. In the previous set-up, temperature increased up to 100°C and spreading to the sand formation while in the current model, temperature locally increased to the same value (around 100°C), but in the limestone formation. Still, it affected the temperature increase in the sands formation but not that much as in case (b).

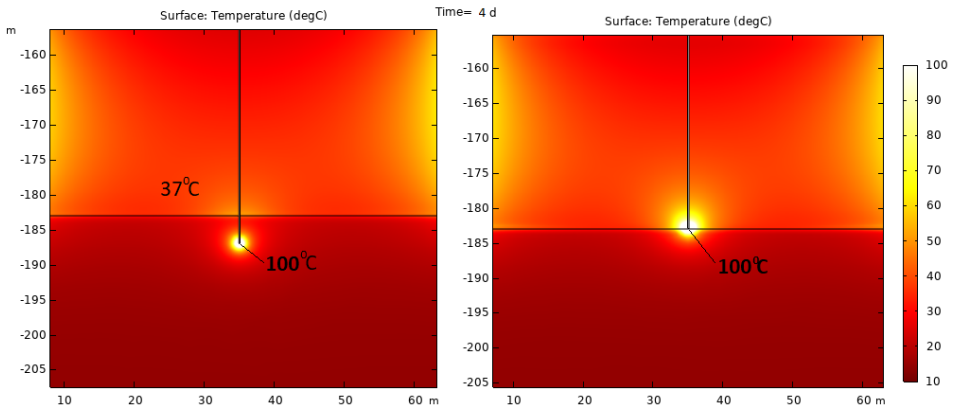

(a) (b)

Figure 6.6. Production well length modification (a) current model (b) previous model

6.3. Cooling System

Large temperature increase was noticed at the production well, especially at the injection well electrodes (Fig. 6.2 (a), (c)). This phenomenon can cause the breakdown of electrodes during the operation, which is one of the troubles of electrode exploitation (McGee and Vermeulen, 1996). Injection wells were prolonged up to the surface which resembled realistic configuration at the field. To remove heat from the electrodes, cold water must be injected in the wells, but not in the sand formation. In this model, water was injected into well bore and was discharged from the model at the bottom of the wells to remove heat (Fig. 6.7). After temperature in the whole formation reached appropriate value, water was injected into formation and the bitumen displacement process started. In the simulation first, 15 days were dedicated to the cooling, and it prevented electrodes overheating. In between 15 and 35 days water was injected into formation and two-phase flow started. This effect contributed to the results with smooth water saturation profile.

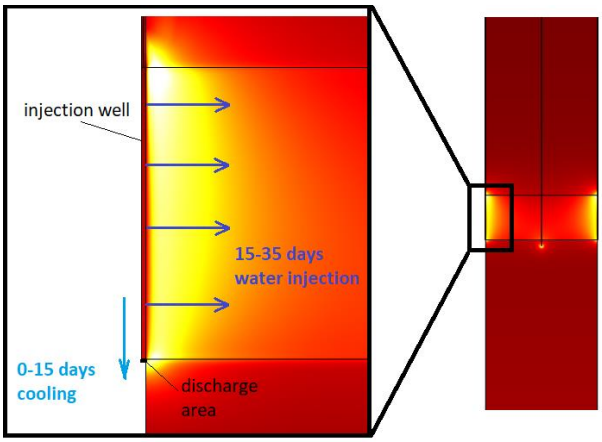

Figure 6.7. Water discharge scheme

6.4. Timing of Water Injection

Timing of water injection played great role in bitumen extraction outcome. As it was mentioned in previous subchapter that the best way was to heat up the formation to let bitumen viscosity decrease enough so the difference between water and bitumen viscosities would not be tangible. Important point was not to let the electrode overheat happen. For this reason, cooling system was implemented as discussed in section 6.3. Let us look at how water injection timing affected the result. In case (a), water was injected from the beginning of heating, while in case (b), first 15 days were dedicated to preheating cool the electrodes, then water injection into formation started on 15th day. Temperature profiles in both cases were presented along horizontal section 1-1 along sands formation (Fig. 5.8). In case (a), temperature increased more quickly on the production well compared to the injection wells because cold water injection decreased temperature at the that area. Cold water injection did not let bitumen viscosity decrease, and as a result water breaks through. To prevent this effect, sand formation should be preheated and as bitumen viscosity should be decreased before water injection. In this case, displacement process is expected to be more complete, and amount of extracted bitumen should increase. In the case (b), temperature increased in the formation but temperature on electrodes did not exceed 40°C, enough high to decrease bitumen viscosity.

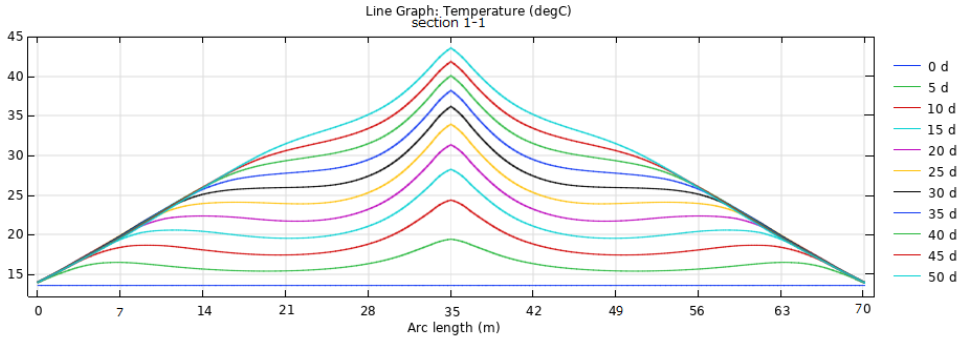

(a) t_w=0 day

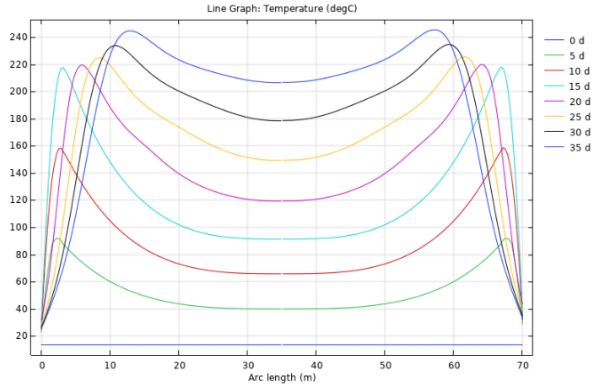

(b) t_w=15 day

Figure 6.8. Temperature profiles in case of different water injection timing

6.5. Meshing

Model discretization can affect simulation results. Inappropriate mesh can lead to inaccurate results. The coarser the mesh, the rougher the results the simulation gives. As an example, on Fig. 6.8 there are two configurations of sands formation mesh. First one was mesh with 25 elements on each side of sands formation domain (a), second one was mesh with 50 elements on each side (b).

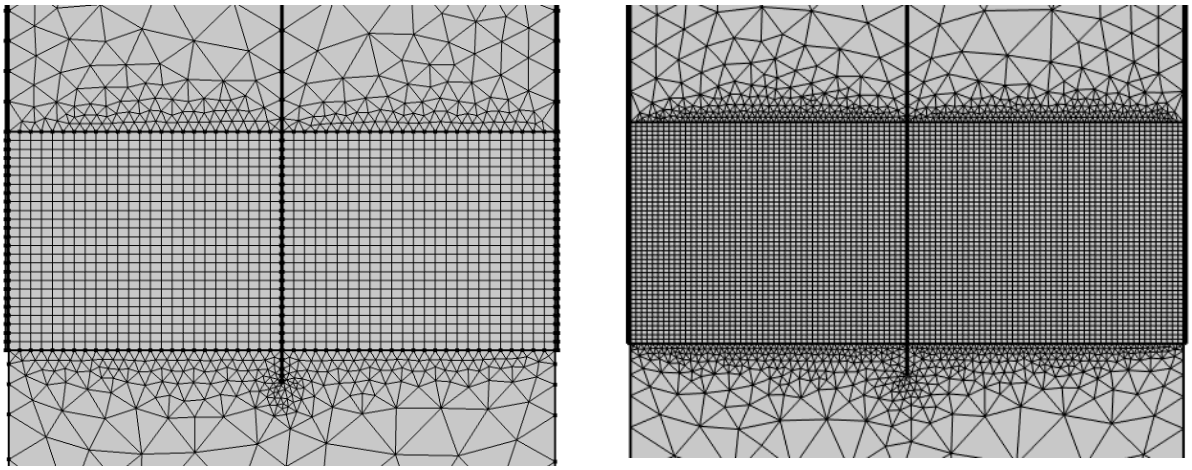

(a) Coarse mesh - 25 elements (b) Fine mesh - 50 elements

Figure 6.9. Sand formation mesh structure

Obtained results of vertical temperature profile showed that in case of coarse mesh, lines of temperature have curves in transition zone between different formations. In case of fine mesh these curves disappeared, and profiles got smoother.

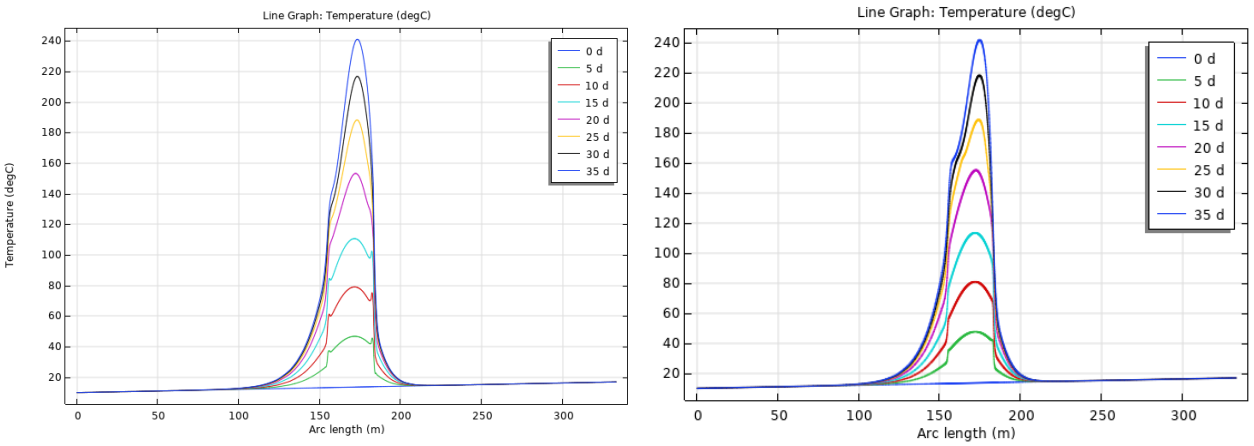

(a) Coarse mesh (b) Fine mesh

Figure 6.10. Temperature vertical profile 2-2

Another example was shown on Fig. 6.10 and 6.11. As it was explained in subchapter 6.2, configuration of edges can give great contribution to the accuracy of results. Meshing of edges also affected the simulation results. Mesh structure of production well edge was shown on Fig. 6.10 (a, b). Triangular structure was applied in limestone domain as it was easier to build mesh structure. Even though the shape of edge was rounded, coarse mesh made the edge triangular with angles in order to build as big cells as possible (Fig. 6.10 (a)). To keep the shape of the edge rounded, fine mesh was built. Fig. 6.11 compared these two different mesh configurations with respect to the electric field streamlines and current density. Color map showed that electric current density distribution was smoother in case of fine mesh (Fig. 6.12 (b)) comparing to coarse mesh (Fig. 6.12 (a)). Current density increased in case (a) compared to case (b). Electric field streamlines were unevenly concentrated at the edge in case of coarse mesh, especially at the sides that formed triangle at the mesh structure (Fig. 6.12 (a)). In case of fine mesh, streamlines did not form equal shape but compared to the coarse mesh streamlines, more uniform.

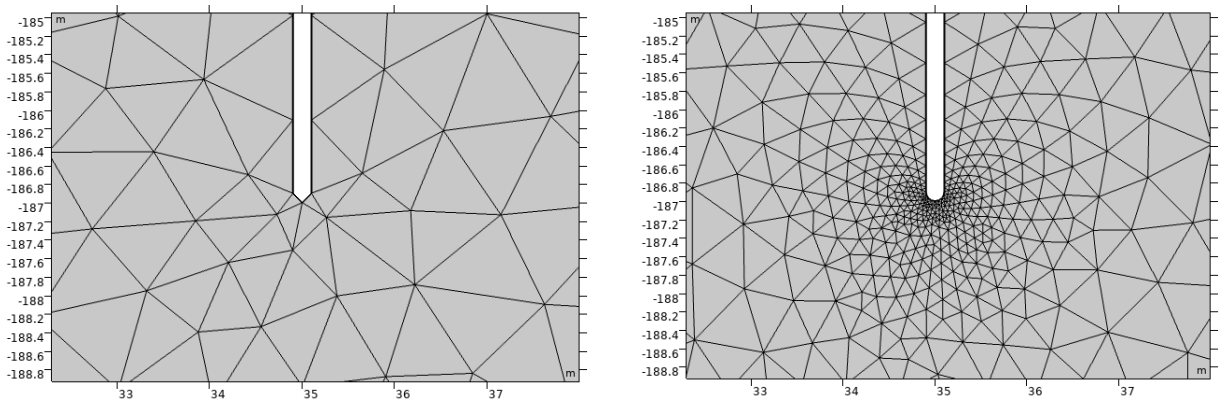

(a) Coarse mesh (b) Fine mesh

Figure 6.11. Production well edge mesh structure

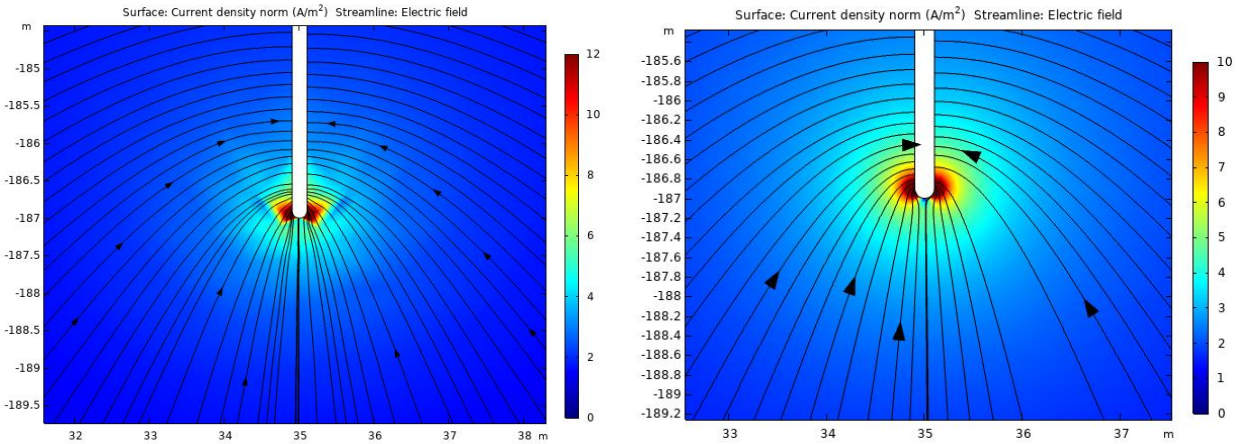

(a) Coarse mesh (b) Fine mesh

Figure 6.12. Production well edge electric field

Finer mesh can give more accurate results, however it requires longer computation time. While building mesh, it is essential to set not only proper cell size but also shape.

6.6. Joule Heating

6.6.1 Electrode configuration

Joule Heating is a basic principle of ETHM. Temperature distribution is dependent on many factors such as geometry, meshing, water injection timing. Electrode spacing and configuration especially affect temperature increase. In this thesis, temperature increase started at the electrodes and bottom edge of the production well. This pattern can be explained by electric field convergence at the edge. Even after round shape configuration and elongation of production well down to the limestone formation, the temperature increase pattern tended to the lower side of sands formation (Fig. 5.8 (a-c)). For further simulations, it is recommended to prolong electrode edge down to limestone formation. Now production

well is prolonged to -187 m which is 4 m deeper than sands formation bottom. It is recommended to increase length at least to -193 m. In sands formation electric field streamlines goes towards to the ground electrode even to the mudstone formation where electric potential is also zero. As for the lower part limestone formation, edge of ground electrode concentrates electric field streamlines creating convergence. This effect cannot be avoided in the simulation but can be minimized by rounding the angles of the edge and increasing length of electrode down to limestone formation. Electric convergence is not described in detail in ETHM especially in field test operation, but it can be assumed that this phenomenon takes place also at ETHM field operation. This problem can become a topic for the further research.

6.6.2 Overall ETHM Process

Joule Heating is based on the principle the more resistivity of the system the more heat accumulates. Water is a conductor, and it decreases systems resistivity making ETHM less effective. For this reason, it was proposed to heat up the formation before water injection into the reservoir. To remove heat from the electrodes cooling system was successfully implemented and electrode temperature was slowly increasing, and it did not exceed 40°C (Fig. 5.8 (d)). As cold water is injected into formation, convection starts contributing to heat transfer process. It cools down the rocks but heat transfers faster, so the profile aligns (Fig. 5.8 (d).

6.7. Two-Phase Fluid Flow

Two-phase fluid flow is a complicated problem. Hangingstone bitumen is highly viscous and it will not flow under natural conditions. The temperature archived in the simulation allowed the decrease of bitumen viscosity more than 10^4 times. However, Figure 5.9 (a) showed slopes on water saturation profiles, which meant that difference of fluid mobilities was still tangible. Some amounts of bitumen left unextracted in the formation. Fig. 5.9 (c) showed that water reaches lower part of production well, displacing the formation from bottom to top. It can be explained by big temperature increase at that area which was caused by electric field convergence. Accumulated heat decreased bitumen viscosity making it more movable. As water usually flows along the path of least resistance, it reached to the production well at the point of higher temperature. This pattern is also seen on Fig. 5.9 (b) where water saturation profile bent at the lower point of sands formation. Darcy's velocity streamlines (Fig.5.11) showed that flow became more intense at the lower part of production well. Pressure profile (Fig. 5.10) showed the big increase at the early stage of production, but it decreased. Recovery rate of production well showed that during first 20 days production of bitumen is predominant (Fig. 5.12). Analysis of production rate of each day showed that average bitumen recovery factor was 73%., which means that ETHM operated successfully. However, on 35^{th} day there were rapid bitumen recovery decrease and water recovery increase. This pattern is typical for oil production, and it leads to water cut increase.

Generally, it was clear that the subsequence of model improvements is important. Firstly, the operation temperature of whole model was raised up to 200°C which is boiling point of water on 170 m depth. It helped to increase the recovery of bitumen and decrease the water cut of production well. Secondly, preheating time was added to simulation. As cold-water injection cooled down the formation, the viscosity of bitumen did not decrease. Due to preheating temperature of the system reached appropriate value decreasing the viscosity of bitumen. Next step was to change the geometry of the model to reach even profile of temperature increase. The length of the wells was prolonged up to the surface which resulted in smooth increase of temperature on the electrodes. Also rounding edges and elongation of well was implemented to avoid the big increase of temperature caused by electric field convergence. Finally, to avoid electrode overheating cooling system was implemented. All these improvements helped to increase the recovery of bitumen.

Chapter 7

Conclusions

Nowadays it is important to produce oil with minimum harm to environment. More than 50% of world conventional oil resources are depleted, and more attention is paid to heavy oil and bitumen production. Hangingstone oil sands field is proved to be a prospective field where SAGD production method has been implemented. ETHM has a lot of advantages as EOR method and can be considered as alternative method to SAGD. Previously, ETHM was studied as EOR method of bitumen reservoirs. Field tests have been carried out at Athabaska, Canada. Also, ETHM was studied as soil remediation method. ETHM is complicated multiphysical process that includes two-phase flow, electric current flow, and heat transfer. In this thesis the main factors that affect ETHM 2-D simulation results were discussed and modifications to improve the efficiency of ETHM were proposed.

In chapter 3, ETHM was divided into simple basic problems. 2-D simulation models were built to understand the physics of the process, find appropriate initial and boundary conditions, and analyze the obtained results stability and accuracy. To prove that COMSOL build and solve 2-D models correctly, analytical solutions were compared to numerical simulation results. This comparison showed that COMSOL works appropriate.

In chapter 4, COMSOL's numerical code was evaluated by reproducing experiment of buoyancy effect (Krol M.M., 2011). As a result of this comparison, the general pattern of isothermal lines obtained by COMSOL was consistent with the pattern of experiment. It can be said that COMSOL is proved to be sufficient numerical tool for simulation coupled multiphysical processes.

In chapter 5, simulation 2-D model and obtained results of Hangingstone oil sands field were described. Two-phase fluid flow resembled pattern of temperature distribution of the system. Temperature increase mainly occurred nearby the current electrodes and the lower part of production well. Pressure of the sand formation increased at the beginning of water injection and then decrease after 20^{th} day. Maximum velocity value was observed at the bottom of production well inside the sand formation. Velocity reached its minimum in mudstone and limestone formations. Recovery rate of production well showed that during 20 days production of bitumen is predominant. Estimated recovery factor was 73% which means that ETHM operated successfully. However, on 35^{th} day there were rapid bitumen recovery decrease and water recovery increase. This pattern is typical for oil production. Suggested geometry configuration can improve recovery factor, as temperature increase would become even and water would slowly expel bitumen from the formation.

In chapter 6, 2-D simulation results were discussed. It was clear, that geometry and electrode configuration affected temperature increase, which started at the electrodes and bottom edge of the production well. This pattern was explained by electric field convergence at the edge. Round shape configuration and elongation of production well helped to minimize electric field convergence at the edges. To prevent electrodes from overheating, cooling system of electrodes was successfully implemented. As a result, temperature on electrodes did not exceed 40°C. Cold water injection into sand formation cooled down the rocks and decreased the resistivity of the system. ETHM became less effective as it is based on the principle the more resistivity of the system the more heat accumulates. As bitumen is high viscous, sand reservoir was preheated during first 15 days. As water usually flows along the path of least resistance, it reached to the production well at the point of higher temperature, where bitumen has already become movable.

During 2-D model simulation the physical processes of ETHM were understood, and based on trial simulations results, model modifications were suggested. Finally, satisfied results were obtained regarding bitumen recovery rate, which means that implemented modifications successfully improved model. For the next step, it can be suggested to assess capital cost and profit to estimate if ETHM is economically efficient.

References

AC/DC Module User's Guide, COMSOL 1998–2020.

AER Hangingstone Project Update, Athabaska Oil Corporation, 2020

Apostolopoulou-Kalkavoura, Varvara & Munier, Pierre & Bergström, Lennart. (2020). Thermally Insulating Nanocellulose - Based Materials. Advanced Materials. 33. 2001839. 10.1002/adma.202001839.

Application for Approval of the Athabasca Oil Corporation's Hangingstone Expansion, Athabaska Oil Corporation, 2017

Archie, G.E.. (1942). The electrical resistivity log as an aid in determining some reservoir characteristics. Transactions of the American Institute of Mining and Metallurgical Engineers. 5. 1-8.

Attanasi and Meyer, 2010. Natural Bitumen and Extra-Heavy Oil. Survey of energy resources (22 ed.). World Energy Council. ISBN: 978 0 946121 021. pp. 123–140.

Bera, Achinta & Babadagli, Tayfun. (2015). Status of Electromagnetic Heating for Enhanced Heavy Oil /Bitumen Recovery and Future Prospects: A Review. Applied energy 151. 206-226.

Bergman, Theodore L. & Lavine, Adrienne S. (2011) Fundamentals of heat and mass transfer (7th ed.). Hoboken, NJ: Wiley.

Blackman, R.A.A.. (1986). Oil in the sea: Inputs, fates, and effects. Marine Pollution Bulletin - MAR POLLUT BULL. 17. 45-46. 10.1016/0025-326X(86)90806-4.

Cengel, Y.A. (2002) Heat Transfer: A Practical Approach. 2nd Edition, McGraw-Hill, New York. ISBN 978-0-07-245893-0.

COMSOL Multiphysics, Porous Media Flow Module, User's Guide, version 5.6, 2020

Diaz-Viera, Martin & López-Falcón, D. & Moctezuma-Berthier, A & Ortiz Tapia, Arturo. (2008). COMSOL Implementation of a Multiphase Fluid Flow Model in Porous Media.

Flint, L. (2005) Bitumen Recovery: A Review of Long Term R&D Opportunities, accessed Nov. 2008.

Gill, W. 1979. The Electrothermic System for Enhanced Oil Recovery. First Intl. Conference on the Future of Heavy Crude and Tar Sands, Ch. 52, 469-473. New York City: McGraw-Hill Book Co. Inc.

Golpour, Smith, 2017. Oil Shale Ex-Situ Process - Leaching Study of Spent Shale. International Journal of Engineering and Science Invention ISSN 2319 – 6726 Vol. 6 (3), pp. 45-53.

Griffiths, David. (2017). Introduction to Electrodynamics. 10.1017/9781108333511.

Hart Energy, 2013. Retrieved from: https://www.hartenergy.com/

Hvizdos, Leonard & Howard, John & Roberts, George. (1983). Enhanced Oil Recovery Through Oxygen-Enriched In-Situ Combustion: Test Results From the Forest Hill Field in Texas. Journal of Petroleum Technology - J PETROL TECHNOL. 35. 1061-1070. 10.2118/11218-PA.

IEA, 2018. World Energy Outlook. Retrieved from: https://www.iea.org/reports/world-energy-outlook-2018

Ingebritsen S. E. & Sanford Ward E. (2006) Groundwater in Geologic Processes, Cambridge University Press, 536 p.

Krol, Magdalena & Sleep, Brent & Johnson, Richard. (2011). Impact of low-temperature electrical resistance heating on subsurface flow and transport. Water Resources Research - WATER RESOUR RES. 47. 10.1029/2010WR009675

Lake L. W., Warner Jr. H.R., Petroleum Engineering Handbook, Volume VI – Emerging and Peripheral Technologies, Pgs. 575-617, 2007.

Layrisse. I, (1999). Heavy Oil Production In Venezuela: Historical Recap And Scenarios For Next Century. 10.2118/53464-MS.

Lee Bell BA MA, 2009. The Heavy Oil Power Deal a Dark Cloud over East Timor's Bright Future, National Toxics Network Inc.

Likhachev, E.. (2003). Dependence of water viscosity on temperature and pressure. Technical Physics. 48. 514-515. 10.1134/1.1568496

LIU, Zuodong & Wang, Hongjun & Blackbourn, Graham & MA, Feng & He, Zhengjun & Wen, Zhixing & Wang, Zhaoming & Yang, Zi & Luan, Tiansi & WU, Zhenzhen. (2019). Heavy Oils And Oil Sands: Global Distribution And Resource Assessment. Acta Geologica Sinica - English Edition. 93. 199-212. 10.1111/1755-6724.13778.

Maugeri, Leonardo, 2006. The age of oil, the mythology, history, and future of the world's most controversial resources. Westport, CT: Praeger Publishers.

McGee, B.C.W. & Donaldson, R.D. (2009). Heat Transfer Fundamentals for Electrothermal Heating of Oil Reservoirs. 10.2118/2009-204.

McGee, B.C.W. & McDonald, Craig W. & Les Little. (2008) Electro-Thermal Dynamic Stripping Process-Integrating Environmentalism with Bitumen Production. Paper presented at the International Thermal Operations and Heavy Oil Symposium, Calgary, Alberta, Canada. doi: https://doi.org/10.2118/117470-MS.

McGee, B.C.W. & Vermeulen, F. (1996). Electrical Heating With Horizontal Wells, The Heat Transfer Problem. 10.2523/37117-MS.

Millikan, Robert A. & Bishop, E.S. (1917). Elements of Electricity. American Technical Society. p. 54. Ohm's law current directly proportional

Oilfield Glossary. Schlumberger Limited. Retrieved from: https://glossary.oilfield.slb.com/

Palo Alto, CA (1999). "Enhanced Oil Recovery Scoping Study", Electric Power Research Institute, Final Report, No. TR-113836.

Raicar, Procter, 1984. Economic considerations and potential of heavy oil supply from Lloydminster–Alberta, Canada. In: Meyer RF, Wynn JC, Olson JC (eds) The future of heavy oil and tar sands, The Second UNITAR International Conference on Heavy Crude and Tar Sands, Caracas, 1982: New York, McGraw-Hill, p. 212-219.

Riebeek, Simmon, 2010. Global Warming. NASA Earth Observatory.

Rudnev, V. & Loveless, Don & Cook, Raymond & Black, Micah. (2002). Handbook of Induction Heating. 10.1201/9781420028904.

Sarathi,. (1998). In-Situ Combustion Handbook -- Principles and Practices. 10.2172/3175.

Smalley, Philip. (2000). Heavy oil and viscous oil. In Modern Petroleum Technology, Vol. 1 Upstream, Ch. 11, 409-435, sixth edition, ed. R.A. Dawe.

Souraki, Yaser & Ashrafi, Mohammad & Karimaie, Hassan & Torsæter, Ole. (2012). Experimental Analyses of Athabasca Bitumen Properties and Field Scale Numerical Simulation Study of Effective Parameters on SAGD Performance. Energy and Environment Research. 2. 10.5539/eer.v2n1p140.

Supplementary materials of Hangingstone oil sands Project, JAPEX, 2012

Temizel, Cenk & Canbaz, Celal Hakan & Tran, Minh & Abdelfatah, Elsayed & Jia, Bao & Putra, Dike & Irani, Mazda & Alkouh, Ahmad. (2018). A Comprehensive Review Heavy Oil Reservoirs, Latest

Techniques, Discoveries, Technologies and Applications in the Oil and Gas Industry. 10.2118/193646-MS.

Temizel, Cenk & Rodriguez, D. & Saldierna, N. & Narinesingh, J.. (2016). Stochastic Optimization of Steamflooding Heavy Oil Reservoirs. 10.2118/180811-MS.

US EPA, 2020. Overview of Greenhouse Gases. Retrieved from: https://www.epa.gov/ghgemissions/

Whitaker, Stephen. (1986). Flow in Porous Media I: A Theoretical Derivation of Darcy's Law. Transport in Porous Media. 1. 3-25. 10.1007/BF01036523.

Zhang, Jiaming & Chen, Zhangxin. (2018). Formation Damage by Thermal Methods Applied to Heavy Oil Reservoirs. 10.1016/B978-0-12-813782-6.00009-9.

Zhang, Yiming & Evans, Julian & Yang, Shoufeng. (2011). Corrected Values for Boiling Points and Enthalpies of Vaporization of Elements in Handbooks. Journal of Chemical & Engineering Data. 56. 328-337. 10.1021/je1011086.

Appendix

Previously simulated model results are presented here. The main difference from the present model is geometry by omitting injection wells and cooling electrodes. Injection and production were 10 m instead of 28 m (Fig. A.1 (a)). Initial conditions are the same as present model (subchapter 5.1.4); however, boundary conditions are changed. Water is injected to the sand formation as well as electric current from the wells interval. Ground condition is set along production well interval (Fig. A.1. (b)). Electric insulation and symmetry boundary conditions are set on the vertical walls of the model. Only bitumen viscosity is considered to be temperature dependent. Figure A.2 showed the representative cross sections. i.e., section 1-1 was a horizontal section along the sand formation, and section 2-2 was vertical section along the whole model.

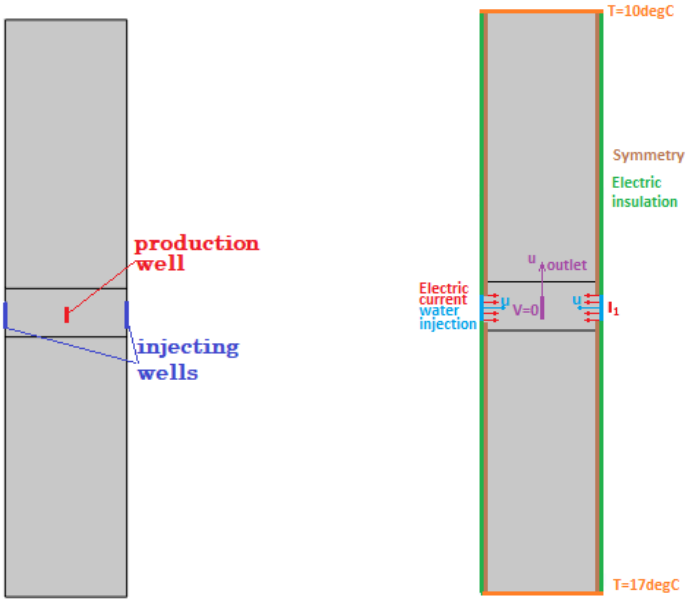

(a) (b)

Figure A.1 Schematic geometry (a) and boundary conditions (b)

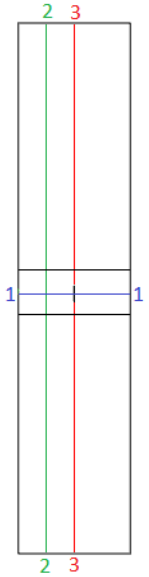

Figure A.2. Sections map

Calculated saturation profiles are shown on Fig. A.3. We can see water intrusion in sands formation on Fig.A.3. (a). Water flows mainly into sands formation, however there is some water occurring nearby production well when waterfront has not yet reached the production well. Horizontal profile 1-1 (Fig. A.3. (b)) shows water saturation distribution along sands formation. At left and right borders we can see that saturation profile starts from 1, which means that injecting wells are fully saturated with water.

At the production well we can see increase of water saturation which also occurs on Fig. A.3 (a). This pattern can be explained by the fact that even viscosity of bitumen is decreased, still it is bigger than water. This means that water has bigger mobility and oil is too viscous to be fully expelled from the sands formation. Due to this water breaks its pass through the formation and reached production well faster than oil. On the section 2-2 (Fig. A.3. (b)) we can see that no flow occurs in mudstone and limestone formations as filtration characteristics are much lower comparing to the sand's formation.

Water saturation profiles show non-Buckley-Leverett displacement process (Fig. 3.6). Even after heating and decrease of bitumen viscosity (from 90 Pa·s to 0.11 Pa·s), it is still huge bitumen-water viscosities difference (100 times). This problem can be partly solved by increasing time of heating process before water injection and raising the temperature of heating (temperature 200˚C bitumen viscosity 0.004 Pa·s).

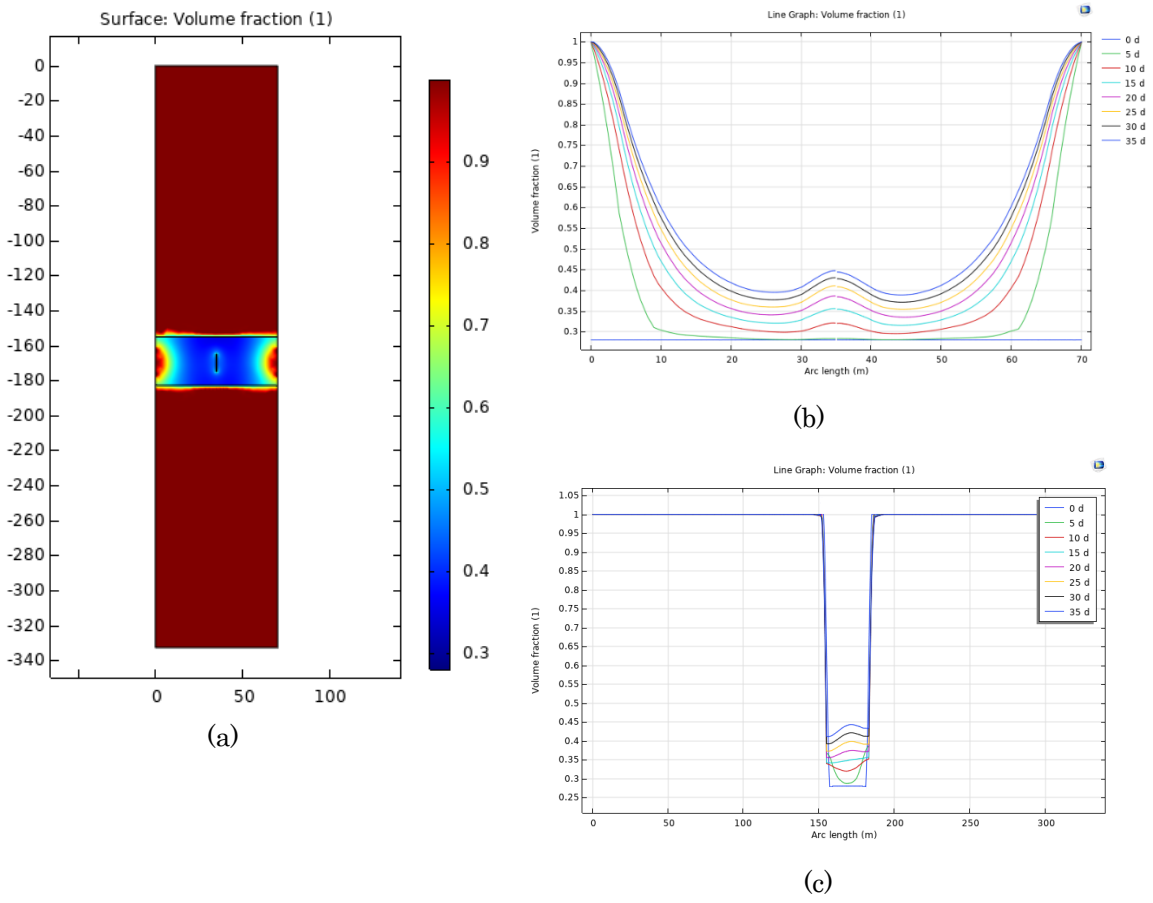

Figure A.3. Water saturation profile (a) surface map, (b) horizontal section 1-1, (c) vertical section 2-2

On Fig. A.4 (a) and (b), temperature increase was observed nearby production well. As water is injected into the sands, the system's resistivity drops, and the Joule Heating becomes less effective. That is why temperature is higher nearby the production well than on the injection wells. On the section 1-1 (Fig. A.4 (b)) we can see that cold water injection decreases temperature nearby injection wells. Temperature increase occurs mainly in the sand's formation. On the section 2-2 (Fig. A.4 (c)) there is still a heat dissipation into upper and down rocks as we can see temperature increase nearby the sands.

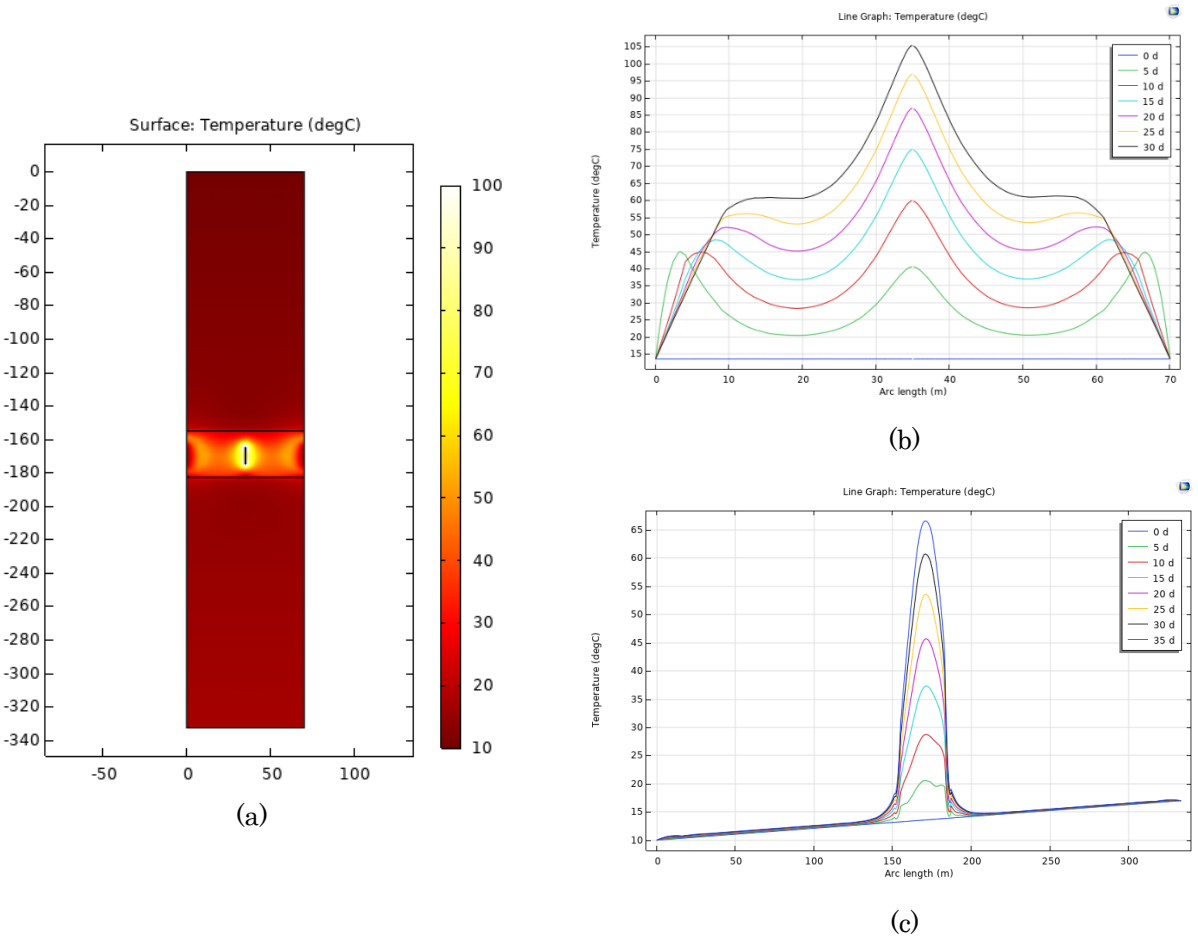

Figure A.4. Temperature profile (a) surface map, (b) horizontal section 1-1, (c) vertical section 2-2

On section 1-1 we can see big pressure gradient (Fig. A.5) at the beginning of water injection process which is caused by huge viscosity difference of fluids. As convection process started and viscosity of bitumen started decreasing pressure gradient also decreases.

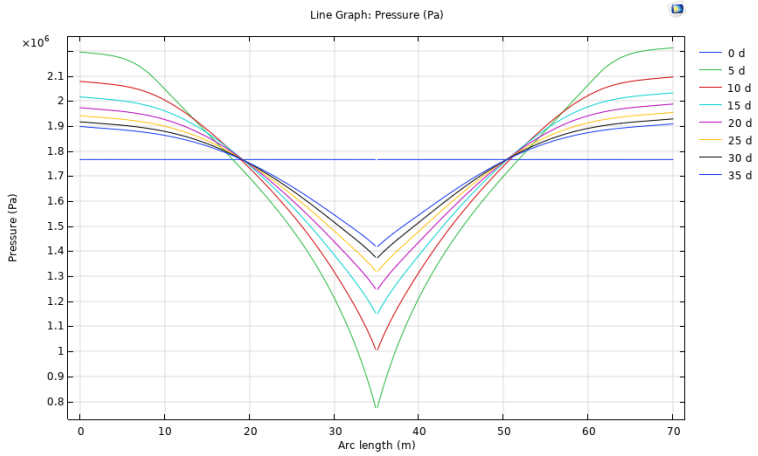

Figure A.5. Pressure profile on section 1-1

On Fig. A.6 (a) Darcy's velocity streamlines shows the flow direction from injection wells to production well. Velocity increases with time on section 1-1 (Fig. A.6 (b)). As viscosity of bitumen decreases and mobility increases, velocity also increases.

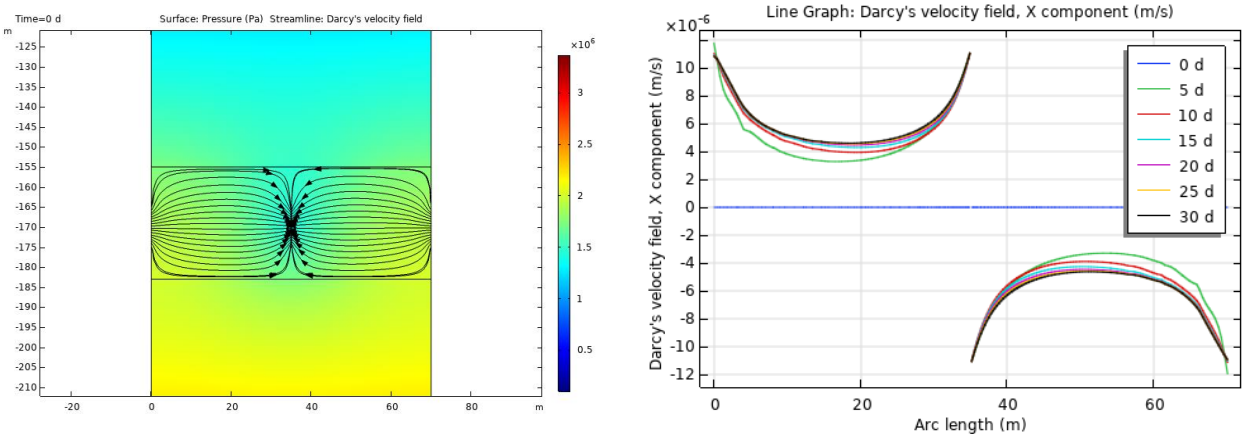

(a) (b)

Figure A.6. Velocity profile (a) surface map (b) horizontal section 1-1